COPPE
Instituto Alberto Luiz Coimbra de Pós-Graduação e Pesquisa de Engenharia
UFRJ

EXPERIMENTALLY BASED MECHANICAL MODEL OF SANDWICH PIPES WITH A STRAIN-HARDENING CEMENTITIOUS COMPOSITE CORE

Huarong Cheng

Tese de Doutorado apresentada ao Programa de Pós-graduação em Engenharia Oceânica, COPPE, da Universidade Federal do Rio de Janeiro, como parte dos requisitos necessários à obtenção do título de Doutor em Engenharia Oceânica.

Orientadores: Segen Farid Estefen
Bianca de Carvalho Pinheiro

Rio de Janeiro
Dezembro de 2020

EXPERIMENTALLY BASED MECHANICAL MODEL OF SANDWICH PIPES WITH A STRAIN-HARDENING CEMENTITIOUS COMPOSITE CORE

Huarong Cheng

TESE SUBMETIDA AO CORPO DOCENTE DO INSTITUTO ALBERTO LUIZ COIMBRA DE PÓS-GRADUAÇÃO E PESQUISA DE ENGENHARIA DA UNIVERSIDADE FEDERAL DO RIO DE JANEIRO COMO PARTE DOS REQUISITOS NECESSÁRIOS PARA A OBTENÇÃO DO GRAU DE DOUTOR EM CIÊNCIAS EM ENGENHARIA OCEÂNICA.

Orientadores: Segen Farid Estefen
Bianca de Carvalho Pinheiro

Aprovada por: Prof. Segen Farid Estefen
Prof. Bianca de Carvalho Pinheiro
Prof. Murilo Augusto Vaz
Prof. Ney Roitman
Prof. Celio Albano da Costa Neto
Prof. Celso Kazuyuki Morooka

RIO DE JANEIRO, RJ – BRASIL
DEZEMBRO DE 2020

Cheng, Huarong

Experimentally based mechanical model of sandwich pipes with a strain-hardening cementitious composite core/Huarong Cheng. – Rio de Janeiro: UFRJ/COPPE, 2020.

XIV, 101 p.: il.; 29, 7cm.

Orientadores: Segen Farid Estefen

Bianca de Carvalho Pinheiro

Tese (doutorado) – UFRJ/COPPE/Programa de Engenharia Oceânica, 2020.

Referências Bibliográficas: p. 92 – 101.

1. Mechanical model. 2. Sandwich pipes. 3. Strain-hardening cementitious composite. I. Estefen, Segen Farid *et al.* II. Universidade Federal do Rio de Janeiro, COPPE, Programa de Engenharia Oceânica. III. Título.

To my dear family for their endless love, support and encouragement

Acknowledgement

It would not be possible to accomplish the present thesis without supports from many people. First, I would like to express my sincere gratitude to my supervisor, Prof. Segen Farid Estefen, who leads me to the area of ocean engineering and guides me with the methodology for conducting research.

I would like to thank my co-supervisor, Prof. Bianca C. Pinheiro, for her valuable suggestions and insightful comments, besides the knowledge related to my topic. I have learned a lot from the enthusiastic discussion with her. And her rigorous scientific attitude on research will have a profound influence on me.

Special thanks to Dr. Claudio M. Paz. Thank you for the sincere discussion and help in the test during the research on the concrete damage plasticity model. Reinaldo Merendaz helps me a lot in the push-out test. I would express my gratitude to him as well. Many thanks also go to the staff of Subsea Technology Laboratory (LTS) for all the help during my doctoral study.

Special thanks to all my friends. I feel very warm in such a foreign country because of their help. The talks on imagining the future, celebrations of various special days, and awesome travelings, made my life here much more colorful. The time living and studying together with them is my most precious memories in Rio de Janeiro.

I am also grateful for the support from the China Ship Scientific Research Center (CSSRC), not only for the financial support but also for providing such a valuable opportunity.

Last, but certainly not least, to my family: my parents, thanks for their encouragement and support; my fiance, Zhao Yue, thanks for her warm companionship and endless encouragement. I would not have reached this stage without their support.

Resumo da Tese apresentada à COPPE/UFRJ como parte dos requisitos necessários para a obtenção do grau de Doutor em Ciências (D.Sc.)

MODELO MECÂNICO BASEADO EM EXPERIMENTOS DE DUTOS SANDUÍCHE COM ANULAR DE COMPÓSITO CIMENTÍCIO REFORÇADO

Huarong Cheng

Dezembro/2020

Orientadores: Segen Farid Estefen
Bianca de Carvalho Pinheiro

Programa: Engenharia Oceânica

A tese visa construir um modelo mecânico completo para os Dutos Sanduíche (SPs), o qual consiste, principalmente, do modelo plástico de danos no concreto (CDP) para o anular do SHCC e o modelo real de comportamento intercamada.

A tese propõe um modelo particular CDP para o anular SHCC em três partes. Para a evolução do dano, dois modelos de variáveis do dano, sob tração e compressão, são propostos baseados nos dados experimentais uniaxiais disponíveis e na teoria da energia da fratura. Para o critério de escoamento, os parâmetros para o modelo de Lubliner são fornecidos de acordo com os dados experimentais dos testes compressivos uniaxiais e biaxiais. Para a regra de escoamento plástico, o ângulo de dilatação do concreto é deduzido de testes compressivos triaxiais combinados com a regra de escoamento plástico de Drucker-Prager.

Posteriormente, a tese analisa o real comportamento entre camadas, utilizando os testes de deslizamento entre camadas (push-out) e de tensão residual (self-stress), e um modelo numérico do deslizamento (camada bond-slip) é proposto. O modelo de elementos finitos do comportamento entre camadas é modelado em três partes: modelo coesivo de base superficial para o comportamento camadas interligadas e livres, modelo de fricção de Coulomb para o comportamento de fricção na direção tangencial, e o modelo de contato da pressão de fechamento na direção normal.

Finalmente, para verificar o modelo completo dos SPs, os resultados das simulações numéricas de colapso e flexão são correlacionados a testes experimentais em escala real, apresentando boa concordância. Um estudo paramétrico foi então realizado para investigar a influência de parâmetros geométricos e ovalização inicial na resistência última à flexão.

Abstract of Thesis presented to COPPE/UFRJ as a partial fulfillment of the requirements for the degree of Doctor of Science (D.Sc.)

EXPERIMENTALLY BASED MECHANICAL MODEL OF SANDWICH PIPES WITH A STRAIN-HARDENING CEMENTITIOUS COMPOSITE CORE

Huarong Cheng

December/2020

Advisors: Segen Farid Estefen
Bianca de Carvalho Pinheiro

Department: Ocean Engineering

The thesis aims to build a comprehensive mechanical model for Sandwich pipes (SPs), which mainly consists of the concrete damage plasticity (CDP) model for the SHCC core and the actual interlayer behavior model.

The thesis proposes a particular CDP model for the SHCC core based both on experimental data and on the continuum damage mechanics (CDM) theory. The fundamentals of the CDP model can be divided into three major issues, namely, damage evolution, yield criterion, and plastic flow rule. For the damage evolution, two models of damage variables, under tension and compression, respectively are built based on uniaxial experimental data available and the fracture energy theory. For the yield criterion, the parameters for the Lubliner model are fitted according to available experimental data from uniaxial and biaxial compressive tests. For the plastic flow rule, the dilation angle is deduced from the results of triaxial compressive tests combined with the Drucker-Prager type plastic flow rule.

Then, the thesis investigates the actual interlayers behavior through push-out and self-stress tests, and a bond-slip layer numerical model is proposed. The finite element model of the actual interlayer behavior is modeled in three parts as the surface-based cohesive model for the bond-debonded behavior, the Coulomb friction model for the frictional behavior in the tangential direction, and the pressure-overclosure contact model in the normal direction.

Finally, to verify the whole mechanical model of SPs, the results from collapse and bending numerical simulations are correlated to full-scale tests, presenting good agreement. A parametric study is then performed to investigate the influence of geometric parameters and initial ovality on the ultimate bending strength.

Contents

List of Figures

List of Tables

Chapter 1

Introduction

1.1 Overview

With the development of the offshore oil and gas industry in deep and ultra-deep waters, new concepts of structural pipelines have been proposed to face the challenge of lower temperatures and higher hydrostatic pressures in these scenarios [1, 2]. Sandwich pipes (SPs), composed of two concentrically steel tubes with a filling core (annular), between inner and outer pipes, are designed to assure that the three layers withstand, simultaneously, the high external hydrostatic pressure and the high internal pressure from the fluid being transported. The strain hardening cementitious composite (SHCC) can be applied in the core (annular) layer to contribute to the thermal insulation, avoiding both hydrate and paraffin formation.

SPs were introduced by Estefen et al. [3] with the advantage of reducing the installation weight. It was shown that the optimized high strength-to-weight ratio can greatly benefit their installation process, and, consequently, reduce costs [3]. In the SP, the core layer is the most critical part of the design phase [1]. The design of the core layer should consider the influence of its mechanical strength, thermal insulation capacity, fracture behavior, and weight. To assure the thermal insulation, Castello and Estefen [4] used polypropylene as the core material. However, this material showed manufacturing problems associated with the adhesion to the steel pipes. Further, Velasco et al. [5] designed the steel fiber reinforced concrete (SFRC) as a possible core material. However, the SFRC has shown to be sensitive to crack propagation when submitted to large bending moments. Based on experimental evidence, An et al. [1] finally identified the strain-hardening cementitious composites (SHCC) as the optimum core material. Unlike the tensile softening behavior, after the elastic domain, shown by the SFRC material, the SHCC material has revealed suitable strain hardening behavior properties for subsea pipes, with the potential for

reducing manufacturing costs in engineering applications [6]. The strain at tensile failure of SHCC was reported ranging from 2% to 8%, with the fiber volume fractions below 2% [7]. This high strain behavior at tensile failure can greatly improve the resistance to crack propagation [8, 9].

For further research on the property of SPs during installation and service, the mechanical model should be built first. The whole model should consist of a mechanical model for the SHCC core, a mechanical model for the tubes, and the mechanical model of the actual interlayer behavior. The mechanical model for the tubes can be easily gotten by the standard uniaxial tensile and compressive tests. However, the mechanical model for the SHCC core and the actual interlayer behavior are more complex.

Currently, the SHCC concept has been studied based on experimental procedures and numerical simulations based on test data input. The research issues focused on the tensile and compressive properties and crack propagation behavior. Yu et al. [7] experimentally observed strains up of 8% at the tensile failure of an SHCC material. Lu [10] built a new numerical model for the cracking process of SHCC based on tension test data. Swanepoel [11] carried out systematic tests to study the behavior of SHCC under biaxial compressive loading. Nevertheless, there are still few reports on the building of a CDP model for SHCC material. An et al. [1] used the CDP model to simulate the mechanical behavior of the SHCC core in sandwich pipes under external pressure. However, no detailed information on the model building process was provided and damage variables were not considered in this model. Khalil et al. [12] used the CDP model to study the nonlinear behavior of beams strengthened with SHCC subjected to monotonic and cyclic loads. The model just considers the uniaxial tensile behavior and ignored the damage variables and other parameters of the CDP model.

Also, no research was reported on the actual interlayer behavior of SPs. Some researchers, as An et al. [1], Arjomandi and Taheri [13], and Castello et al. [4] simulated the SPs interlayer behavior under two extreme conditions, fully bonded and unbounded. Others used friction models to simulate the interlayer interaction behavior, as Yang et al. [14] and Xu et al. [15]. The results from all these researches showed that the interlayer behavior has a significant influence on the mechanical analysis of the SPs.

Set against this background, this thesis did a comprehensive research on the mechanical model of the SHCC core and actual interlayer behavior of SPs. The corresponding experiments and verifying tests were performed. Also, finite element simulations were carried out to simulate these results and, after being calibrated and validated, the proposed numerical model can provide a precise estimate of the SP mechanical properties.

1.2 Motivation and objectives

The motivation of this thesis is to build a comprehensive mechanical model for the SPs. Based on this motivation, the following objectives were defined step by step:

- A comprehensive literature review on the CDP model and the interlayer behavior.
- Build of a modified CDP model for the SHCC core.
- Verification of a modified CDP model with specific tests and correlation between numerical and experimental results.
- Study of the actual interlayer behavior of SPs through specific tests, and build the corresponding numerical model.
- Verification of the whole mechanical model of SPs with full-scale tests and correlation between numerical and experimental results.

1.3 Outline of the thesis

To comply with the objectives listed in Section 1.2, the thesis is planned to be divided into seven chapters.

- **Chapter 2 Literature review**

A comprehensive literature review on the CDP and the actual interlayer behavior research is presented.

For the CDP model of the SHCC core, the fundamentals of the CDP model are introduced. The fundamentals of the concrete damage plasticity (CDP) model contain three major parts: damage evolution, yield criterion, and plastic flow rule. The damage evolution is the critical part of the CDP model, the methods to calculate the damage variables are summarized.

For the actual interlayer behavior, firstly, the experimental methods on the SPs interlayer behavior study are identified, the push-out and self-stress tests are chosen for the study. Then, the methods used to simulate the actual interlayer behavior are introduced, and the surface-based cohesive contact in ABAQUS is selected. Finally, the surface-based cohesive contact theory is introduced in details.

- **Chapter 3 Modified CDP model for the SHCC material**

A modified concrete damage plasticity (CDP) model is proposed for the SHCC core based both on experimental data and the continuum damage mechanics (CDM) theory. The whole CDP model can be divided into three major issues, namely, damage evolution, yield criterion, and plastic flow rule.

For the damage evolution, two models of damage variables, under tension and compression, respectively, are built based on uniaxial experimental data and the fracture energy theory.

For the yield criterion, the parameters for the Lubliner model are fitted according to available experimental data from uniaxial and biaxial tests.

For the plastic flow rule, the dilation angle is deduced from the results of triaxial compressive tests combined with the Drucker-Prager model.

- **Chapter 4 Verification test for the CDP model**

To verify the modified CDP model for the SHCC material, four-point bending tests are carried out on SHCC specimens and collapse tests are conducted on SP models.

Then, the results from numerical simulations, based on the finite element method, are correlated with experimental data. The correlation between numerical and experimental results are analized.

- **Chapter 5 Experimental research on the interlayer behavior of SPs**

Push-out tests are designed to study the actual interlayer behavior of the SPs. Specific tests are designed to measure the self-stress in the SPs.

Based on the test data, the numerical models of the interlayer behavior are proposed, and the friction coefficients between the tubes and SHCC core are deduced. Then, the finite element models are built to simulate the interlayer behavior model considering the surface-based cohesive contact and friction behavior.

- **Chapter 6 Verify tests for the mechanical model of SPs**

To verify the whole mechanical model of SPs, full-scale collapse and bending experiments are performed on full-scale SP models. Finite element models of the SPs are built, and the correlation between numerical and experimental results are analyzed.

Furthermore, the SP ultimate bending moment and post-failure behavior under pure bending are also investigated using the FE model. The ultimate bending capacities of the sandwich pipes is estimated from the numerical simulations. The influence of geometric parameters and initial ovality on the ultimate bending moments is also analyzed.

- **Chapter 7 Conclusions and future works**

The final chapter resumes the main conclusions drawn during the thesis development and points out some meaningful work that exceeds its scope, them as possible future investigations.

Chapter 2

Literature Review

A comprehensive review of the concrete damage plasticity (CDP) model and research on the actual interlayer behavior of sandwich pipes (SPs) is introduced.

First, current research outcomes on CDP models for the SHCC core are summarized, the fundamentals of the CDP model are briefly described, and since the damage variables are the critical parameters for whole CDP model, the methods to calculate damage variables are presented.

Then, the experimental procedures applied in the present work to study the actual interlayer behavior of the SPs, the methods used to simulate the actual interlayer behavior are discussed. Finally, the surface-based cohesive theory is introduced in details.

2.1 Current research of the CDP model on SHCC core

The CDP model is a plasticity-based continuum damage model [16–18], assuming a plastic regime under tensile and compressive loads [16, 17, 19–21]. It generally identifies the failure of the concrete into tensile cracking or compressive crushing [16, 19, 21, 22]. Lubliner et al. [20] first proposed a model using one fracture-energy-based damage variable to represent the total damage. Then, Lee and Fenves [21] separated it into two damage variables, which are related to tensile and compressive stresses, respectively.

A concrete damage plasticity (CDP) model can be used to simulate concrete, reinforced concrete structures, and other quasi-brittle materials used in different applications and structures [16, 20, 21, 23, 24]. By combing isotropic damage elasticity and isotropic tensile and compressive plasticity, it can model nonlinear deformation

and irreversible damage in plain concrete materials applied to different types of structures, under different load conditions [18, 25–27].

Inspired by this approach, many researchers investigated the failures of concrete structures. Yan et al. [28] used the CDP model to analyze the damage of steel-concrete-steel (SCS) walls used in offshore structures. Alfarah et al. [29] used the CDP model to investigate the behavior of a reinforced concrete (RC) structure with a steel joint. The CDP model has been widely used for the SFRC concept. Hany et al. [30] modified the CDP model for an SFRC material and simulated the compressive behavior. Ribeiro et al. [31] numerically simulated confined SFRC columns with a modified CDP model. Tysmans et al. [32] built a model for high-performance SFRC using the CDP model to study its biaxial behavior.

More recently, the SHCC concept has been studied on experimental procedures and numerical simulations based on test data input. The research issues focused on the tensile and compressive properties and crack propagation behavior. Yu et al. [7] experimentally observed strains up to 8% at the tensile failure of an SHCC material. Lu [10] built a new numerical model for the cracking process of SHCC based on tension test data. Swanepoel [11] carried out systematic tests to study the behavior of SHCC under biaxial compressive loading. Nevertheless, there are still few reports on the building of a CDP model for SHCC material. An et al. [1] used the CDP model to simulate the mechanical behavior of the SHCC core in sandwich pipes under external pressure. However, no detailed information on the model building process was provided and damage variables were not considered in this model. Khalil et al. [12] used the CDP model to study the nonlinear behavior of RC beams strengthened with SHCC subjected to monotonic and cyclic loads. The model just considers the uniaxial tensile behavior and ignored the damage variables and other parameters of the CDP model.

2.2 Fundamentals of the concrete damage plasticity model

The fundamentals of the concrete damage plasticity (CDP) model contain three major parts: damage evolution, yield criterion, and plastic flow rule [16, 18, 33, 34].

2.2.1 Damage evolution

Traditionally, the classic elastic-plastic regime is used to represent the nonlinear deformation of the quasi-brittle materials, which is composed of the elastic and plastic strain, ε^{el} and ε^{pl}, respectively

$$\varepsilon = \varepsilon^{el} + \varepsilon^{pl} \tag{2.1}$$

However, in the CDP model, the nonlinearity is due to a combination of damage and plasticity. Two damage parameters characterize the degradation of the elastic stiffness, referred as d_t and d_c, under tension and compression, respectively. The constitutive relations under uniaxial tensile and compressive loads are given, respectively as

$$\sigma_t = E(\varepsilon_t - \varepsilon_t^{pl}) = (1 - d_t)E_0(\varepsilon_t - \varepsilon_t^{pl}) \tag{2.2}$$

and

$$\sigma_c = E(\varepsilon_c - \varepsilon_c^{pl}) = (1 - d_c)E_0(\varepsilon_c - \varepsilon_c^{pl}) \tag{2.3}$$

where E_0 is the initial elastic stiffness of the material (undamaged condition); σ_t and σ_c are the tensile and compressive stresses, respectively.

The model defines the effective tensile stress $\overline{\sigma_t}$ and compressive stress $\overline{\sigma_c}$ as:

$$\overline{\sigma_t} = \frac{\sigma_t}{(1 - d_t)} = E_0(\varepsilon_t - \varepsilon_t^{pl}) = E_0\varepsilon_t^{el} \tag{2.4}$$

and

$$\overline{\sigma_c} = \frac{\sigma_c}{(1 - d_c)} = E_0(\varepsilon_c - \varepsilon_c^{pl}) = E_0\varepsilon_c^{el} \tag{2.5}$$

As shown in Fig. 2.1b, the total compressive strain of the CDP model can be divided into the undamaged elastic strain ε_{0c}^{el} and the damage inelastic strain ε_c^{in} as

$$\varepsilon_c = \varepsilon_c^{in} + \varepsilon_{0c}^{el} \tag{2.6}$$

with

$$\varepsilon_{0c}^{el} = \frac{\sigma_c}{E_0} \tag{2.7}$$

Applying Eq.2.6 and 2.7 into Eq.2.3, the compressive plastic strain ε_c^{pl} is obtained as

$$\varepsilon_c^{pl} = \varepsilon_c - \varepsilon_{0c}^{el} = \varepsilon_c^{in} - \frac{d_c}{1 - d_c} \times \frac{\sigma_c}{E_0} \tag{2.8}$$

Similarly, as shown in Fig. 2.1a, the total tensile strain ε_t is divided into the

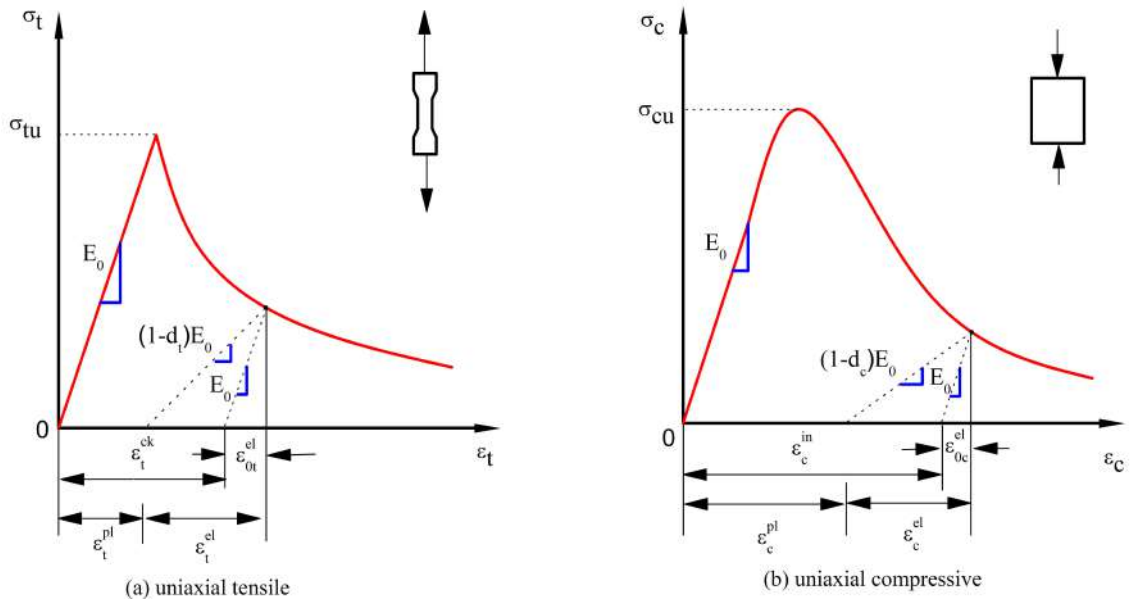

Figure 2.1: Stress-strain relationships [1, 18, 35]

undamaged tensile elastic strain ε_{0t}^{el} and the damage tensile cracking strain ε_t^{ck} , as

$$\varepsilon_t = \varepsilon_t^{ck} + \varepsilon_{0t}^{el} \tag{2.9}$$

with

$$\varepsilon_{0t}^{el} = \frac{\sigma_t}{E_0} \tag{2.10}$$

Eq. 2.9 and 2.10 into Eq. 2.2, the tensile plastic strain ε_t^{pl} is obtained as

$$\varepsilon_t^{pl} = \varepsilon_t - \varepsilon_t^{el} = \varepsilon_t^{ck} - \frac{d_t}{1 - d_t} \times \frac{\sigma_t}{E_0} \tag{2.11}$$

For the numerical simulations in ABAQUS [35] , the compressive behavior data is inputted with the damage compressive inelastic strain ε_c^{in}, compressive stress σ_c and the compression damage variable d_c, while the tensile behavior data is inputted with the damage tensile cracking strain ε_t^{ck}, the tensile stress σ_t and the tension damage variable d_t. During the simulation process, compressive plastic strains ε_c^{pl} and tensile plastic strains ε_t^{pl} are automatically computed based on the input data. When the compressive or tensile plastic strains show negative values $\varepsilon_c^{pl} < 0$ or $\varepsilon_t^{pl} < 0$, an error is detected and the simulation ends.

2.2.2 Yield criterion

In the concrete damage plasticity model (CDPM), the yield criterion was assumed according to Lubliner [20] and further modified by Lee and Fenves [21]. In terms of

effective stresses, it takes the following form

$$\frac{1}{1-\alpha}(\sqrt{3J_2}+\alpha I_1+\beta\langle\overline{\sigma}_{max}\rangle-\gamma\langle-\overline{\sigma}_{max}\rangle)=c \tag{2.12}$$

with

$$I_1=\sigma_1+\sigma_2+\sigma_3 \tag{2.13}$$

$$J_2=-(1/6)[(\sigma_1-\sigma_2)^2+(\sigma_2-\sigma_3)^2+(\sigma_3-\sigma_1)^2] \tag{2.14}$$

where α, β and γ are material parameters;$\overline{\sigma}_{max}$ is the maximum principal effective stress; $\langle.\rangle$ denotes the Macauley bracket; c is the compressive cohesion.

2.2.3 Flow rule

For the plastic flow, the CDP model used the non-associated potential plastic flow hypothesis. The potential function G has a Drucker-Prager type hyperbolic form [36]:

$$G=\sqrt{(e\sigma_{to}\tan\psi)^2+\overline{q}^2}-\overline{p}\tan\psi=0 \tag{2.15}$$

where $\overline{p}$ is the von Mises equivalent effective stress; $\overline{q}$ is the hydrostatic stress; ψ is the dilation angle measured in the $p-q$ plane at high confining pressure; σ_{to} is the uniaxial tensile stress; e is the eccentricity that defines the rate at which the function approaches the asymptote, and by default $e=0.1$ is adopted [37–39].

2.3 Methods to calculate the damage variable

In the framework of continuum damage mechanics, a scalar damage variable d is introduced, with theoretical values ranging between 0 and 1. Kachanov [40] first proposed the concept of continuum damage mechanics followed by Rabotnov [41] provides a practical tool to the damage processes inside the materials at a macroscopic continuum level [42]. The research on the damage variables based on the continuum damage mechanics theory [45, 49, 50].

However, up to now, there is still no standard method to calculate the damage variables. So herein, a summary will be performed.

2.3.1 Elasticity damage theory

Based on the elasticity damage theory, it assumes the damage case of the degradation of the elastic stiffness [43, 44, 46–48]. As shown in the Fig.2.2, the current elastic stiffness (E) at the point of (ε_1, σ_1) can be expressed as:

$$E = (1 - \mathrm{d})E_0 = \sigma_1/\varepsilon_1 \tag{2.16}$$

where E_0 is the initial elastic modulus, the damage variable (d) is deduced as

$$d = 1 - \frac{\sigma_1/\varepsilon_1}{E_0} \tag{2.17}$$

This is an approximate method to calculate the damage variable, it can be used for the brittle material. However, for the quasi-brittle materials, such as concrete and SHCC, it can not get sufficient accuracy.

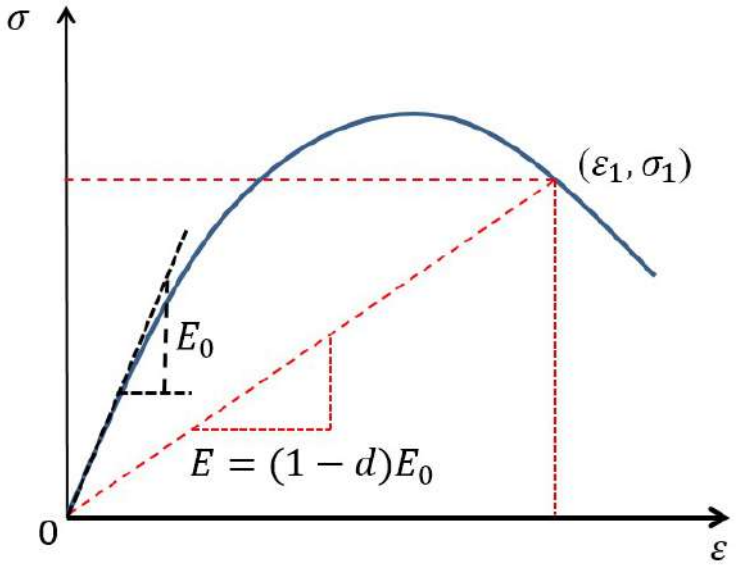

Figure 2.2: The elasticity damage theory [44]

2.3.2 Classic plasticity damage theory

Based on the classic damage theory d can be expressed as follows [56–61]:

$$d = \frac{W_0 - W_\varepsilon}{W_0} \tag{2.18}$$

where W_0 is the strain energy under an undamaged condition; W_ε is the strain energy under a damaged condition, as shown in Fig. 2.3, and given respectively as

$$W_0 = \frac{E_0\varepsilon^2}{2} \tag{2.19}$$

and

$$W_\varepsilon = \int \sigma d\varepsilon = \int f(\varepsilon)d\varepsilon \tag{2.20}$$

where W_ε can be calculated based on a segmentation method, the Simpson integral,

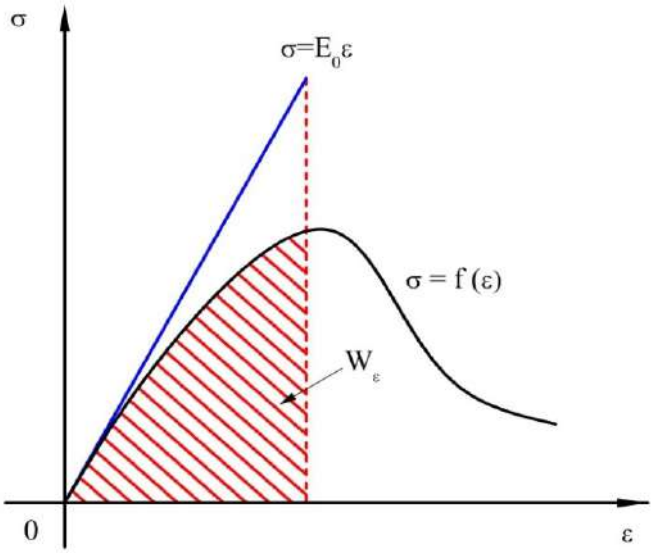

Figure 2.3: The classic damage-based theory [45, 49, 50]

the Gauss integral or other numerical integration methods [62–64].

So the damage variable d is deduced as:

$$\mathrm{d} = \frac{E_0\varepsilon^2/2 - \int f(\varepsilon)d\varepsilon}{E_0\varepsilon^2/2} \tag{2.21}$$

This method can be used in concrete and other quasi-brittle materials. The key points are to calculate the E_0 and $f(\varepsilon)d\varepsilon$ based on stress-strain curves of experiments.

2.4 Review of the experimental methods the interlayer behavior of SPs

Currently, researches on interlayer behavior were all reported based on polypropylene core. Castello and Estefen [65] did adhesion tests using two shear specimen types. Xu et al. [15] designed a simple shear specimen as shown in Fig.2.4(a) to identify the circumferential adhesion characteristics of SPs with a polypropylene core. The specimen was uniaxially stretched until the failure of the bonding surface, as displayed in Fig. 2.4(b). Then, the pure shear stress is calculated by the total force applied to the specimen divided by the overlapping area on one side.

There is still no experimental study for the actual interlayer behavior of SPs with an SHCC core. However, there are a series of studies on the concrete-filled steel tube (CFST) columns in civil engineering. The CFST columns have gradually become a central element in structural systems owing to their high bearing capacity,

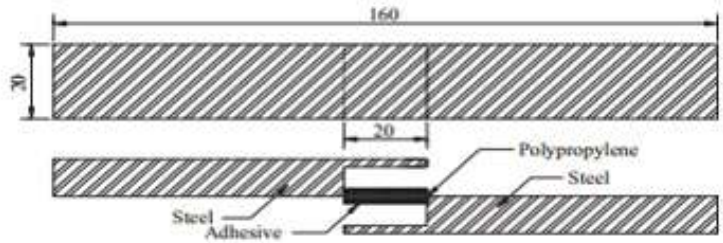

(a) Dimensions of the test specimen (mm)

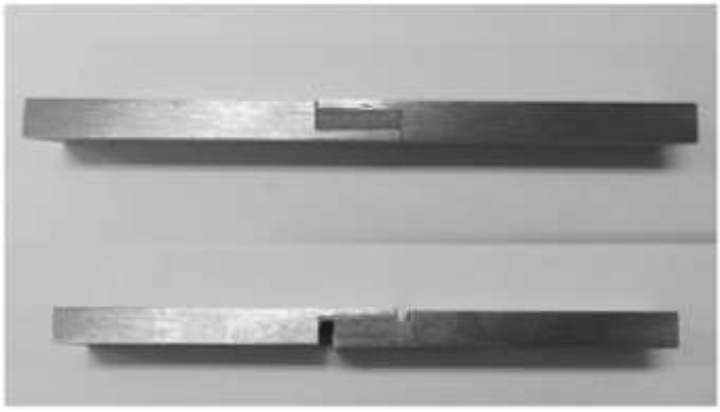

(b) Shear test specimen before and after the test

Figure 2.4: Shear test for the SP interlayer behavior study by Xu [15]

rigidity, ductility, and sutiable performance under seismic loading or fire conditions [66, 67]. The steel tube serves as longitudinal and transverse confinement to the concrete infill, and the concrete core can stabilize and stiffen the steel tube to delay the local buckling [58, 68, 69]. The project of these composite structures requires excellent bond behavior between the steel tubes and the concrete core.

As shown in Fig.2.5, both the CFST columns and SPs consist of steel tubes and a cement-based material core. Both of them have similar interlayer behavior. So, the researches on the interlayer behavior of CFST columns can be a good reference for SPs.

To study the actual interlayer behavior of CFST columns, the push-out test is commonly used. This type of test was first recommended by RILEM-7-II-128 [70] and was used to investigate the bond behavior between concrete and steel bars, as reported by Gooranorimi et al. [71]. In recent decades, this test was adapted to study the bond behavior of concrete-filled steel tubes in civil engineering. This type of test was conducted by Tao et al. [72], Chen et al. [73], and Qu and Liu [53], leading to very encouraging results of the bond-slip curves, which motivated its widly use [74–81]. Inspired by the above-mentioned researches, the push-out test was chosen in the present work, and specimens were designed for this purpose.

After investigating, the push-out tests almost have the same experimental devices

(a) CFST columns with concrete core (b)SP with SHCC core

Figure 2.5: Examples of CFST with concrete infill and a SP with an SHCC core [51]

form [82]. During the push-out test by Lu [51], as shown in Fig.2.6, the specimen was installed in a vertical position with a prefabricated air gap at the bottom. A circular steel block with a cross-section that was slightly lesser than that of the concrete core is placed at the top of the specimen. During testing, the vertical load was applied only on the concrete core, and subsequently, the concrete core was pushed downward. To measure the slip value between the steel tube and concrete core, two linear variable displacement transducers (LVDTs) are located vertically. The strain gauges were posted to analyze the load transfer between the steel tube and concrete. The similar push-out test was chosen to study the actual interlayer behavior of the SPs, the special specimens would be designed. The details will be introduced in the corresponding chapters.

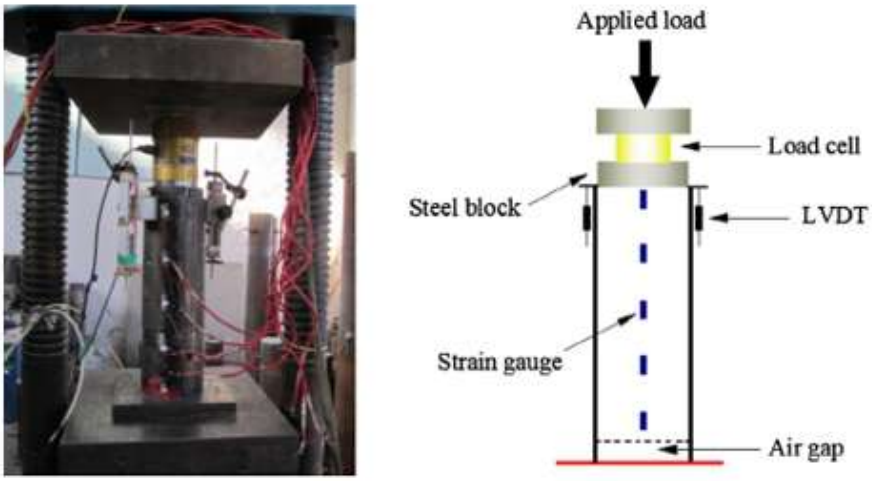

Figure 2.6: Push-out test arrangement by Lu [51]

2.5 Models to simulate the interlayer behavior

The bond-slip numerical models proposed from the push-out tests are mainly divided into four categories. Xue [52] proposed a simplified elastic-plastic model by load-reversed push-out tests on 32 circle CFST columns, as shown in Fig.2.7(a). Qu and Liu [53] proposed a three-segment linear bond strength-slip model based on the analyses of push-out tests on square CFST columns, as shown in Fig.2.7(b). Djamai et al. [54] proposed a four-segment linear bond strength-slip model, as shown in Fig.2.7(c) and Wang et al. [55] proposed a four-segment nonlinear bond strength-slip model, as shown in Fig.2.7(d), respectively.

The Coulomb friction model, nonlinear spring elements, and the surface-based cohesive contact can be used to simulate the bond-slip relationship between steel sections (tubes, bars, etc.) and concrete layers.

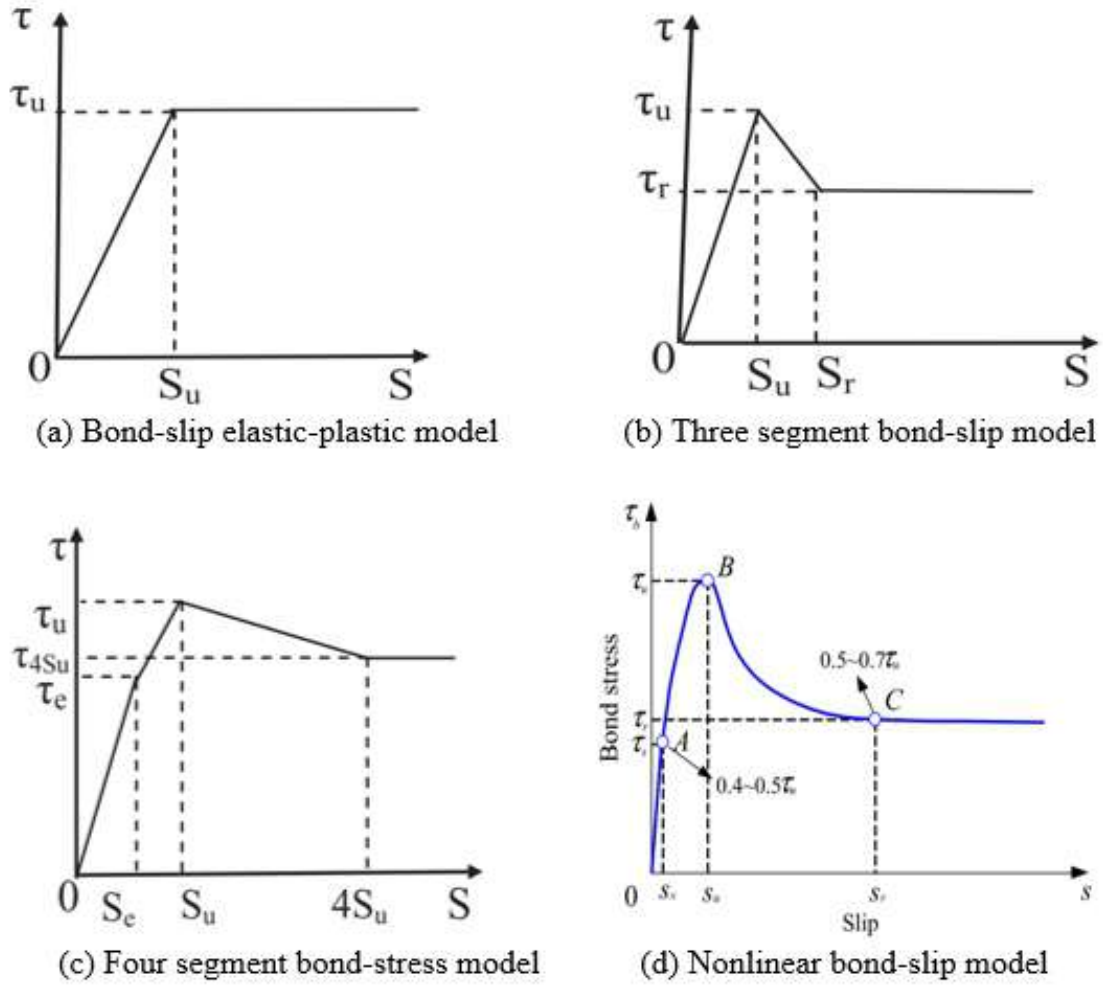

Figure 2.7: Interlayer bond-slip model review [52–55]

The Coulomb friction model can be used to simulate the elastic-plastic bond-slip model as shown in Fig.2.7(a). The self-stress and the fraction coefficient between the steel tubes and the concrete core can be measured by experiments.

There are three types of spring elements in ABAQUS [35], namely Spring1, Spring2, and SpringA. Spring1 element is an elastic spring element with only one node; Spring2 element has two nodes, each node has only one degree of freedom; SpringA element is connected along with two points, each point has three degrees of freedom.

Spring2 element in ABAQUS is a nonlinear spring element, which can reflect the whole bond-slip model as shown in the Fig.2.7(a) and Fig.2.7(b). X. Castello [4] and Xu [15] all used the Spring2 element to simulate the interlayer behavior during the analysis of the SPs collapse with the polypropylene core, as shown in the Fig.2.8.

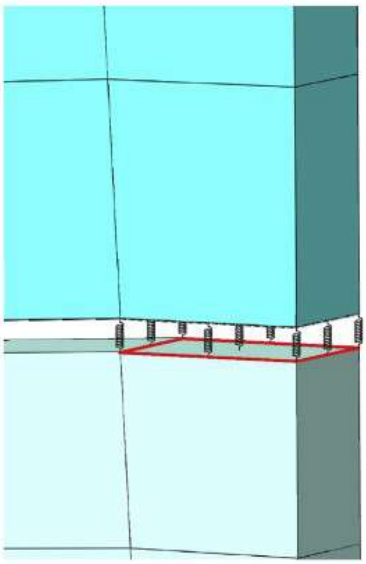

Figure 2.8: Schematic diagram of spring connection between tube and polypropylene [15]

The difficulty for the simulation with the Spring2 element is that it is necessary to find a large number of pairs of nodes on the steel tube and the core materials to define two nodes of the spring elements. As shown in the Fig.2.8, each corresponding pair nodes must be added one Spring2 element manually. It makes the simulation model very complicate and the calculation ineffective, especially for the models with thousands of nodes. Also, the simulation may meet the convergence issues with such large numbers of the nonlinear spring elements.

Surface-based cohesive behavior is primarily intended for situations in which the interface thickness is negligibly small. It can be used to model sticky contact, which means that surfaces or parts of surfaces that are not initially in contact may bond on coming into contact; subsequently, the bond may damage and fail[35]. The sticky contact just meat the interlayer situation of the SPs.

A linear elastic traction-separation law is assumed before the damage and the failure of the cohesive bond is characterized by degradation of the cohesive stiffness,

which is an assumption based on the fracture energy or the separation. For each situation, the post damage softening response main has the linear softening and the exponential softening. Therefore, it can be used to simulate all the bond-slip models in the Fig.2.7. Also, that damage in surface-based cohesive behavior is an interaction property, not a material property, so it can be defined as part of the surface interaction properties that are assigned to the applicable surfaces which can make the model and simulation simplify. Detail of the surface-based cohesive behavior theory is introduced in the following section.

2.6 Surface-based cohesive contact behavior theory

Surface-based cohesive behavior provides a simplified way to model cohesive connections using the traction-separation constitutive model [35, 83, 84]. As shown in Fig.2.9, the available traction-separation model contains three parts as initially linear elastic behavior, damage initiation, and damage evolution[82, 85, 86]. Contact separations are the relative displacements between the nodes on the slave surface and their corresponding projection points on the master surface along with the contact directions. Stresses are defined for surface-based cohesive behavior as the cohesive forces acting along with the contact normal and shear directions divided by the current area at each contact point. The specifics of the corresponding parts are discussed in the following.

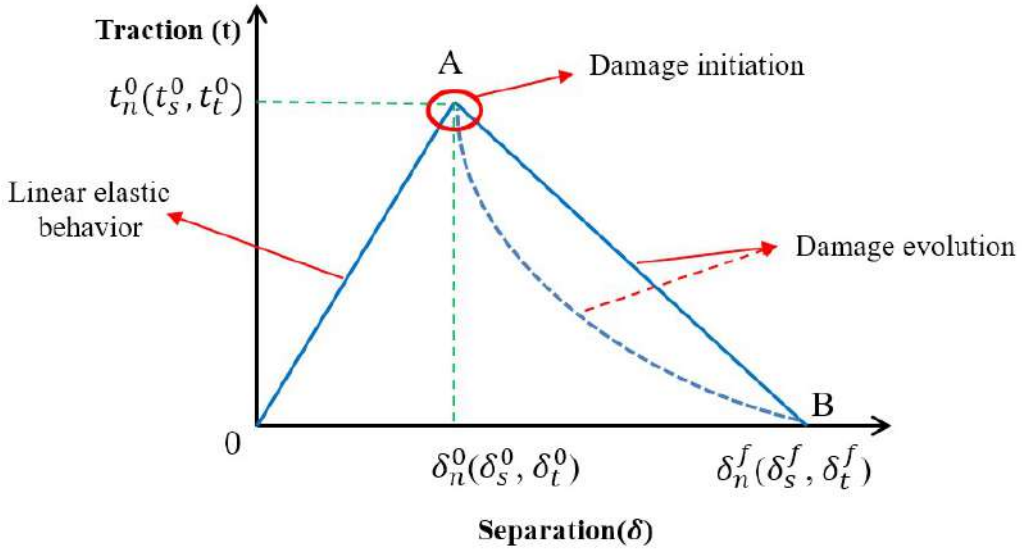

Figure 2.9: Typical traction-separation response

2.6.1 Linear elastic behavior

The elastic behavior is written in terms of an elastic constitutive matrix that relates the normal and shear stresses to the normal and shear separations across the interface. The nominal traction stress vector, $\vec{t}$, consists of three components: t_n, t_s, and t_t, which represents the normal and the two shear tractions, respectively. The corresponding separations are denoted by δ_n, δ_s, and δ_t. The elastic behavior can then be written as

$$\vec{t} = \begin{Bmatrix} t_n \\ t_s \\ t_t \end{Bmatrix} = \begin{bmatrix} K_{nn} K_{ns} K_{nt} \\ K_{ns} K_{ss} K_{st} \\ K_{nt} K_{st} K_{tt} \end{bmatrix} \begin{Bmatrix} \delta_n \\ \delta_s \\ \delta_t \end{Bmatrix} = \vec{K}\vec{\delta} \tag{2.22}$$

In ABAQUS [35], for uncoupled traction-separation behavior, the terms K_{nn}, K_{ss}, and K_{tt} must be defined. For coupled traction-separation behavior, all the terms in the matrix must be defined. The terms can be defined by the corresponding experiments.

For coupled traction-separation behavior, the mix-mode is shown as Fig.2.10. where $\tau = \sqrt{{\tau_s}^2 + {\tau_t}^2}$ is a measure of the effective shear traction.

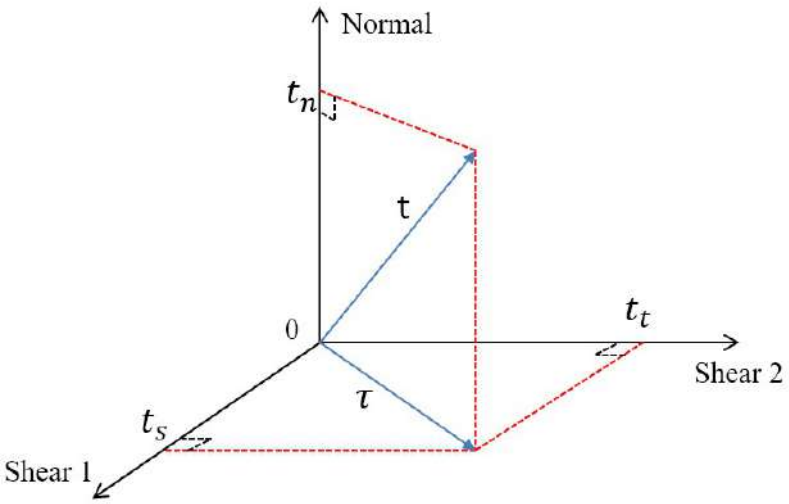

Figure 2.10: Mix-mode based on traction

2.6.2 Damage initiation

The failure mechanism of the traction-separation constitutive model consists of two ingredients: a damage initiation criterion and a damage evolution law. The initial response is assumed to be linear as discussed above. Once a damage initiation criterion is met, damage can occur according to a defined damage evolution law.

Damage initiation means the beginning of degradation, which starts with the specified damage initiation criteria satisfied. The process of degradation begins when the contact stresses and/or contact separations satisfy certain damage initiation criteria as specified. Several damage initiation criteria are available and are discussed below.

The main damage initiation criteria are maximum stress criterion (Eq.2.23), maximum separation criterion (Eq.2.24), quadratic stress criterion (Eq.2.25), and quadratic separation criterion (Eq.2.26) as shown

$$\max\left\{\frac{\langle t_n\rangle}{t_n^0}, \frac{t_s}{t_s^0}, \frac{t_t}{t_t^0}\right\} = 1 \tag{2.23}$$

$$\max\left\{\frac{\langle \delta_n\rangle}{\delta_n^0}, \frac{\delta_s}{\delta_s^0}, \frac{\delta_t}{\delta_t^0}\right\} = 1 \tag{2.24}$$

$$\left\{\frac{\langle t_n\rangle}{t_n^0}\right\}^2 + \left\{\frac{t_s}{t_s^0}\right\}^2 + \left\{\frac{t_t}{t_t^0}\right\}^2 = 1 \tag{2.25}$$

$$\left\{\frac{\langle \delta_n\rangle}{\delta_n^0}\right\}^2 + \left\{\frac{\delta_s}{\delta_s^0}\right\}^2 + \left\{\frac{\delta_t}{\delta_t^0}\right\}^2 = 1 \tag{2.26}$$

where, t_n^0, t_s^0 and t_n^0 represent the peak values of the contact stress in a pure model or along with the shear directions; δ_n^0, δ_s^0 and δ_t^0 represent the peak values of the contact separation in a pure model or along with the shear directions, as shown in Fig.2.9. The symbol $\langle\rangle$ represents the Macaulay bracket, which is used to signify that a purely compressive displacement or a purely compressive stress state does not initiate the damage.

To describe the evolution of damage under a combination of normal and shear separations across the interface, it is useful to introduce an effective separation (δ_m) defined by Camanho and Davila [35] as

$$\delta_m = \sqrt{{\delta_n}^2 + \delta_s^2 + \delta_t^2} \tag{2.27}$$

2.6.3 Damage evolution

The damage evolution law describes the rate at which the cohesive stiffness is degraded once the corresponding initiation criterion is reached. It describes the degradation rate of the cohesive stiffness.

A scalar damage variable, D, represents the overall damage at the contact point. It initially has a value of 0. After the damage evolution is modeled, D monotonically evolves from 0 to 1 upon further loading after the initiation of damage. The contact

stress components are affected by the damage according to

$$\overrightarrow{t_n} = \begin{cases} (1-D)\,\overrightarrow{t_n^0}, & \overrightarrow{t_n^0} \geq 0 \\ \overrightarrow{t_n}, & \overrightarrow{t_n^0} < 0 \end{cases} \tag{2.28}$$

$$\overrightarrow{t_s} = (1-D)\,\overrightarrow{t_s^0} \tag{2.29}$$

$$\overrightarrow{t_t} = (1-D)\,\overrightarrow{t_t^0} \tag{2.30}$$

where $\overrightarrow{t_n^0}, \overrightarrow{t_s^0}, \overrightarrow{t_t^0}$ are the contact stress components predicted by the elastic traction-separation behavior for the current separations without damage, respectively.

The damage evolution can be defined on by the specified total fracture energy (G^C) or the effective separation at failure (δ_m^f), as shown in Fig.2.11. For each situation, the post damage evolution main has the linear softening (as shown in Fig.2.11(a)) and the exponential softening (as shown in Fig.2.11(b)).

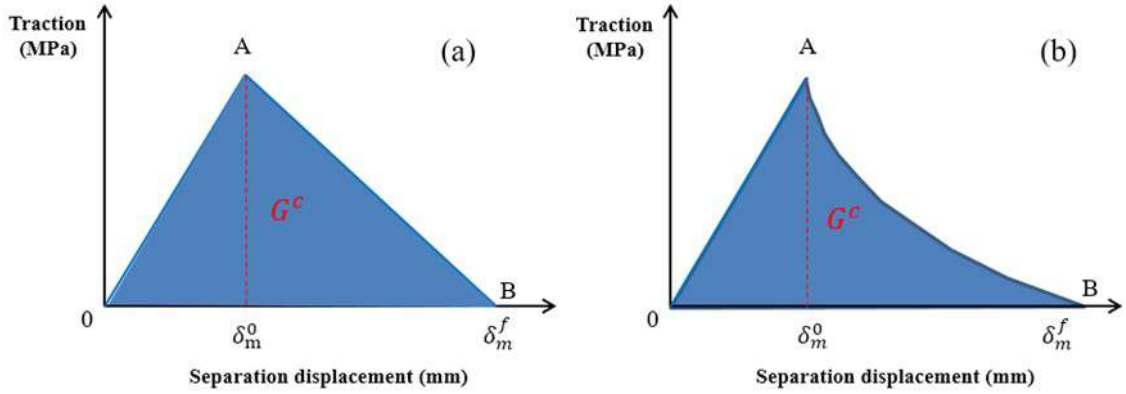

Figure 2.11: Traction-separation constitutive model

Evolution based on effective separation

After specifying the effective separation at failure (δ_m^f), the damage variable (D) model should be specified to decide using linear or exponential softening.

For the linear softening, ABAQUS [35] uses the damage model proposed by Camanho and Davila [35] as

$$D = \frac{\delta_m^f\,(\delta_m^{max} - \delta_m^0)}{\delta_m^{max}\left(\delta_m^f - \delta_m^0\right)} \tag{2.31}$$

where, δ_m^{max}, refers to the maximum value of the effective separation during the loading history; δ_m^f, relatives to the effective separation at complete failure; δ_m^0 relatives to the effective separation at damage initiation.

For the exponential softening, the damage variable model is shown as

$$\mathrm{D} = 1 - \left\{ \frac{\delta_m^0}{\delta_m^{max}} \right\} \left\{ 1 - \frac{1 - \exp\left(-\alpha \left(\frac{\delta_m^{max} - \delta_m^0}{\delta_m^f - \delta_m^0} \right) \right)}{1 - \exp\left(-\alpha\right)} \right\} \tag{2.32}$$

In the equation, $\exp(\alpha)$ is the exponential function, the non-dimensional parameter defines the rate of the damage, is a characteristic parameter.

Evolution based on fracture energy

Damage evolution can be defined based on the energy that is dissipated as a result of the damage process, also called the fracture energy. ABAQUS [35] specifies the fracture energy as a property of the cohesive interaction and either a linear or an exponential softening behavior can be chosen. The area under the linear or the exponential model is equal to the fracture energy, as shown in Fig.2.11.

Two kinds of the energy-based criterion are introduced in ABAQUS [35] as the Power law criterion and Benzeggagh-Kenane fracture criterion [87, 88].

The Power law criterion states that failure under mixed-mode conditions is governed by the energies required to cause failure in the individual (normal and two shears) modes. It is given by

$$\left\{ \frac{G_n}{G_n^C} \right\}^{\alpha} + \left\{ \frac{G_s}{G_s^C} \right\}^{\alpha} + \left\{ \frac{G_t}{G_t^C} \right\}^{\alpha} = 1 \tag{2.33}$$

where G_n, G_s and G_t stand for the energy released on the normal, first shear direction, and second shear direction, respectively. The quantities G_n^C, G_s^C, and G_t^C, are specified by the user, which refers to the critical fracture energies required to cause failure in the normal, the first, and the second shear directions, respectively.

The Benzeggagh-Kenane fracture criterion was proposed by Benzeggagh and Kenane [89] is particularly useful when the critical fracture energies on the first and the second shear directions are the same ($G_s^C = G_t^C$). It is given by

$$G_n^C + \left(G_s^C - G_n^C\right) \left\{ \frac{G_S}{G_T} \right\}^{\eta} = G^C \tag{2.34}$$

where $G_S = G_s + G_t$, $G_T = G_n + G_S$ and η is a cohesive property parameter.

For the linear softening based on the energy-based criterion, the damage variable (D) is reduced as

$$\mathrm{D} = \frac{\delta_m^f \left(\delta_m^{max} - \delta_m^0\right)}{\delta_m^{max} \left(\delta_m^f - \delta_m^0\right)} \tag{2.35}$$

where $\delta_m^f = 2G^C/T_{eff}^0$ with T_{eff}^0 as the effective traction at damage initiation. δ_m^{max}

refers to the maximum value of the effective separation attained during the loading history.

For the exponential softening based on the energy-based criterion, the damage variable (D) is reduced as

$$\mathrm{D} = \int_{\delta_m^0}^{\delta_m^f} \frac{T_{\text{eff}}}{G^C - G_0} d\delta \tag{2.36}$$

where T_{eff} and δ are effective traction and separation, respectively. G_0 is the elastic energy at damage initiation.

2.7 Summary

A comprehensive literature review on the CDP model for SHCC cores and current research outcomes on the actual interlayer behavior were presented.

First, the current research developments and issues on the CDP model for an SHCC material is presented.

Then, the fundamentals of the CDP model were introduced. It was described that the CDP model can be divided into three major parts, namely, damage evolution, yield criterion, and plastic flow rule. To build a modified CDP model for an SHCC core, part should be considered. Also, the methods to calculate the damage variables were summarized.

The classic plasticity damage theory based on the fracture energy theory was recommended using in the future study.

For the actual interlayer behavior, the experimental methods to evaluate the SPs interlayer behavior of SPs are summarized and the push-out test was chosen for the present study.

Then, suitable methods used to simulate the actual interlayer behavior model are introduced and the surface-based cohesive contact available in ABAQUS [35] was selected.

Finally, the surface-based cohesive contact theory was described considering three parts, indentified as initially linear elastic behavior, damage initiation, and damage evolution.

Chapter 3

Modified CDP model for the SHCC material

3.1 Introduction

A particular concrete damage plasticity (CDP) model is proposed for the SHCC core based both on experimental data and the continuum damage mechanics (CDM) theory. The modified CDP model can be divided into three major issues, namely, damage evolution, yield criterion, and plastic flow rule.

For the damage evolution, two models of damage variables, under tension and compression, respectively, are built based on uniaxial experimental data and the fracture energy theory.

For the yield criterion, the parameters for the Lubliner model are fitted according to available experimental data from uniaxial and biaxial compressive tests.

For the plastic flow rule, the dilation angle is deduced from the results of triaxial compressive tests combined with the Drucker-Prager type plastic flow rule.

The details are shown in the following.

3.2 Damage evolution

As described in Chapter 2, uniaxial tensile and compressive data and damage variables should be considered to model the damage evolution. Data from uniaxial tests were used to build the damage variables model.

3.2.1 Uniaxial behavior of SHCC

The composition of the SHCC material is shown in kg per cubic meter in Table 3.1, comprising cement (C), refined sand (S), water (W), fly ash (FA), superplasticizer (SP), and viscosity agent (VA). The maximum grain size of the refined sand should not exceed 0.2 mm. Two classes of fly ash are defined by ASTM C618 [90], namely class F and class C. In this work, class F was adopted for the fly ash and the BS 17 3P water reducing superplasticizer was used. The PVA fiber REC 15 produced by Kuraray was employed with a volume of 2%.

The material properties of the PVA fiber are shown in Table 3.2. The density of the SHCC material is 1830 kg/m^3.

Table 3.1: Mixture proportions of the SHCC material (unit content: kg/m^3)

C	S	W	FA	SP	VA	PVA
488.1	516.1	360.0	593.5	30.0	3.2	29.0

Four block specimens were made for the conduction of uniaxial tensile tests. The mixture of the SHCC materials should follow a strict sequence advised by An [1]. All the test specimens were kept at a room temperature of 21 °C for curing for 28 days.

Fig.3.1(a) shows the dimensions of the 30 mm thickness specimens. The specimens were carefully assembled in the clamps so they could withstand the tensile load. The bolt holes on each side were aligned along with the same direction to avoid torque or bending loads during the experiments.

The final test was set up as shown in Fig.3.1(b). The displacements of the specimens were measured by the two LVDTs.

For the uniaxial compressive tests, four cylindrical specimens, 50 mm in diameter and 100 mm in height, were used. The adopted axial displacement rate was 0.02mm/min. During the experiment, the specimen was positioned on a platform and the axial force was applied through a load cell. The acquisition of displacement during the uniaxial compressive test was performed using strain gages and two LVDTs positioned laterally to the specimen, as shown in Fig. 3.2.

The final test results of the uniaxial tensile and compressive tests are shown inFig.3.3(a) and Fig.3.3(b), respectively. Based on the research of An et al. [1], three successive stages of the material behavior can be identified in these fitted curves: (a) elastic regime, (b) stress hardening, and (c) stress softening.

To allow accurate numerical simulations, suitable constitutive models are adopted to reproduce these successive stages of the material behavior, under both tension and compression. A constitutive model with four successive linear equations

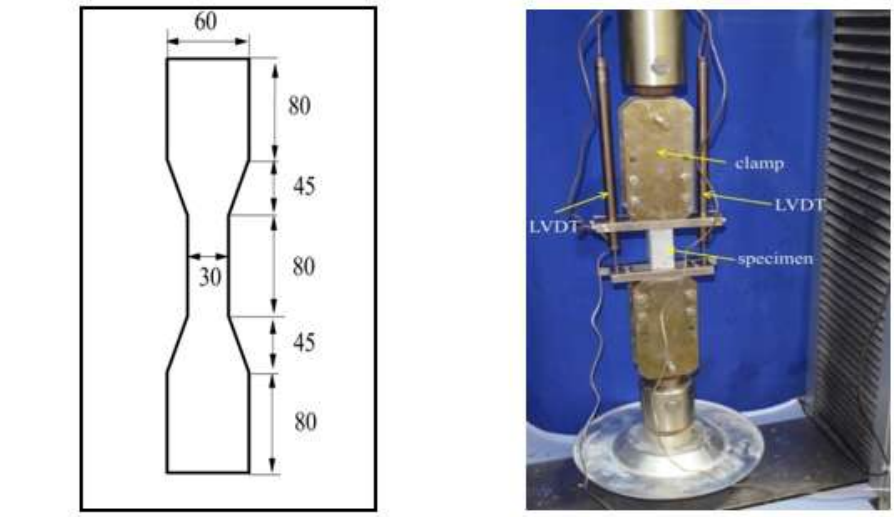

(a) The geometry of the specimen (b) Test set up

Figure 3.1: SHCC geometry and tensile test set up

Figure 3.2: Uniaxial compressive test set up

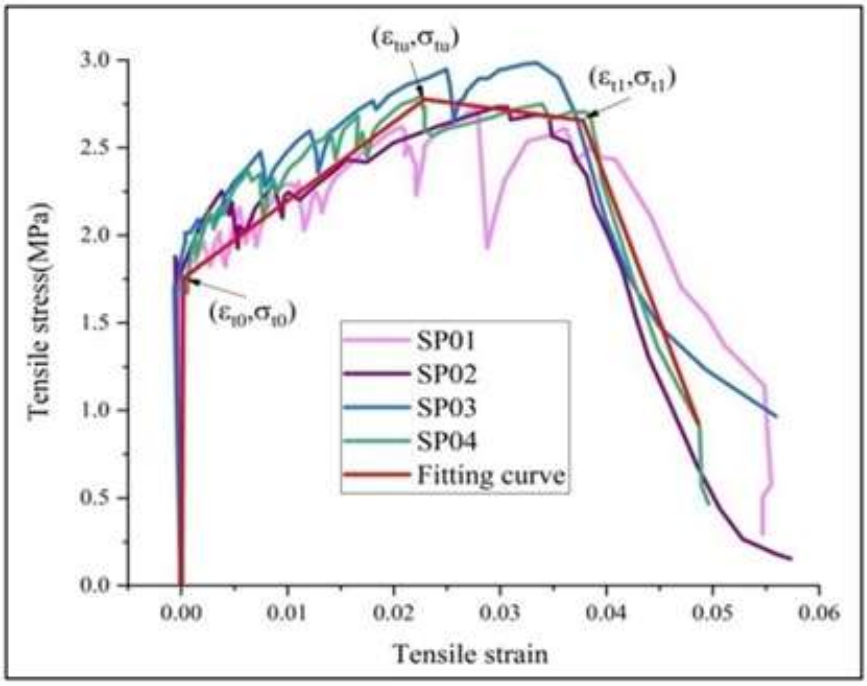

(a) SHCC uniaxial tensile results and fitting curve

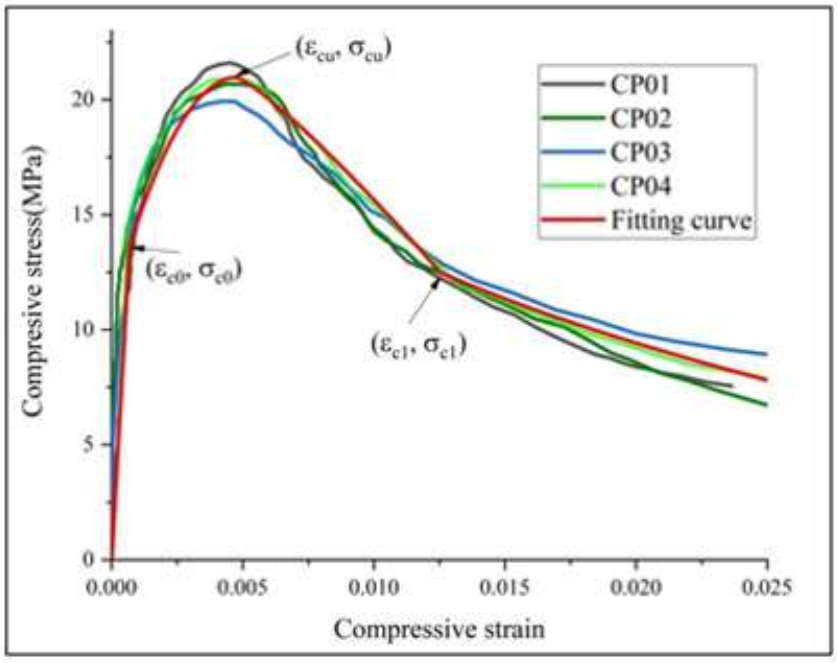

(b) SHCC uniaxial compressive results and fitting curve

Figure 3.3: Uniaxial tests results and fitting curves

Table 3.2: Geometric and material parameters of the PVA fiber

Parameter	Value	Unit
Length (l)	12	mm
Diameter(d)	0.04	mm
Density	1.3	MPa
Tensile strength	1600	MPa
Young Modulus	40.0	GPa
Stretching	7.0 %	

is employed in the simulations, given by

$$\sigma_t = \begin{cases} E_0\varepsilon_t & \text{for } \varepsilon_t \leq \varepsilon_{t0} \\ k_1\varepsilon_t + a_1 & \text{for } \varepsilon_{t0} < \varepsilon_t \leq \varepsilon_{tu} \\ k_2\varepsilon_t + a_2 & \text{for } \varepsilon_{tu} < \varepsilon_t \leq \varepsilon_{t1} \\ k_3\varepsilon_t + a_3 & \text{for } \varepsilon_t > \varepsilon_{t1} \end{cases} \tag{3.1}$$

where $E_0 = 20GPa$,is the initial elasticity modulus; k_1, k_1 and k_3 are the slopes of the different linear segments; a_1, a_2 and a_3 are, respectively, the intercept of these linear equations; ε_{t0} (tensile ultimate elastic strain),ε_{tu}(tensile ultimate strain), andε_{t1} (strain at the turning point) stage) can be identified in Fig.3.3(a).

Velasco proposed that the concrete strain-stress curve under compression can be divided into three parts as [5]

$$\sigma_c = \begin{cases} E_0\varepsilon_c & \text{for } \varepsilon_c \leq \varepsilon_{c0} \\ \sigma_{cu}\left[1 - (1 - \dfrac{\varepsilon_c}{\varepsilon_{cu}})^{\eta_1}\right] & \text{for } \varepsilon_{c0} < \varepsilon_c \leq \varepsilon_{cu} \\ \sigma_{cu}\left[1 - (\dfrac{\varepsilon_c - \varepsilon_{cu}}{\beta_1\varepsilon_{cu}})^{\eta_2}\right] & \text{for } \varepsilon_c > \varepsilon_{cu} \end{cases} \tag{3.2}$$

However, to better simulate the compressive stress-strain behavior in the softening stage, it is divided into two parts and the model given in Eq.3.2 is modified to

Table 3.3: Parameters for the fitted tensile stress-strain curve Eq.3.1

Tensile stress(MPa)		Tensile strain		Fitted parameters	
σ_{to}	1.76	ε_{to}	0.000088	k_1	44.95
				k_2	-8
σ_{tu}	2.79	ε_{tu}	0.023	k_3	158.18
				a_1	1.76
σ_{t1}	2.67	ε_{t1}	0.038	a_2	2.97
				a_3	8.68

$$\sigma_c = \begin{cases} E_0\varepsilon_c & \text{for } \varepsilon_c \le \varepsilon_{c0} \\ (\sigma_{cu} - \sigma_{c0})\left[1 - (\dfrac{\varepsilon_c - \varepsilon_{c0}}{\varepsilon_{cu} - \varepsilon_{c0}})^{\eta_1}\right] + \varepsilon_{c0} & \text{for } \varepsilon_{c0} < \varepsilon_c \le \varepsilon_{cu} \\ \sigma_{cu}\left[1 - (\dfrac{\varepsilon_c - \varepsilon_{cu}}{\beta_1\varepsilon_{cu}})^{\eta_2}\right] & \text{for } \varepsilon_{cu} < \varepsilon_c \le \varepsilon_{c1} \\ \sigma_{cu}\left[1 - (\dfrac{\varepsilon_c - \varepsilon_{cu}}{\beta_2\varepsilon_{cu}})^{\eta_3}\right] & \text{for } \varepsilon_c > \varepsilon_{c1} \end{cases} \tag{3.3}$$

where ε_{c0} is the compressive ultimate elastic strain σ_{cu} and ε_{cu} are the ultimate compressive stress and strain, respectively; $(\varepsilon_{c1}, \sigma_{c1})$ is the turning point in the stress softening stage, as shown in Fig. 3.3(b); η_1, η_2 and η_3 are the exponents describing the rising or declining of the curve and β_1 and β_2 are material parameters.

Table 3.4: Parameters for the fitted compressive stress-strain curve Eq.3.3

Copressive stress(MPa)		Compressive strain		Fitted parameters	
σ_{co}	13.60	ε_{co}	0.00068	η_1	2.02
				η_2	1.17
σ_{cu}	20.97	ε_{cu}	0.0048	η_3	0.46
				β_1	3.49
σ_{c1}	11.91	ε_{c1}	0.0136	β_2	11.62
				-	-

The coefficients of the tensile stress-strain curve model were calculated based on linear fittings and are shown in Table 3.3.

Based on the least square method, with the aid of the software Matlab 14.0, the

coefficients of the compressive stress-strain curve model were determined and shown in Table 3.4.

The final fitted stress-strain curves under tension and compression are shown in Fig. 3.3(a) and (b), respectively. These fitted curves are the basis for the subsequent calculation of damage variables.

3.2.2 New damage variables model for the SHCC material

Based on the summary of the methods to calculate the damage variable in Section 2.3, the classic plasticity damage theory was used to calculate the damage variable in this section.

In the thesis, the integral method is used for the calculation of the tensile damaged strain energy W_{ε}^{t} , and the Simpson integral method is used for the compressive damaged strain energy W_{ε}^{c}.

The tension damage variable (d_t) and the compression damage variable (d_c) were deduced as shown as Eqs.3.4 and 3.5.

$$d_t = \begin{cases} 0 & \text{for } \varepsilon_t \leq \varepsilon_{t0} \\ \dfrac{19419\varepsilon_t^2 - 3.52\varepsilon_t + 0.000155}{20000\varepsilon_t^2} & \text{for } \varepsilon_{t0} < \varepsilon_t \leq \varepsilon_{tu} \\ \dfrac{19472\varepsilon_t^2 - 5.94\varepsilon_t + 0.0236}{20000\varepsilon_t^2} & \text{for } \varepsilon_{tu} < \varepsilon_t \leq \varepsilon_{t1} \\ \dfrac{20158\varepsilon_t^2 - 17.36\varepsilon_t + 0.2408}{20000\varepsilon_t^2} & \text{for } \varepsilon_t > \varepsilon_{t1} \end{cases} \tag{3.4}$$

$$d_c = \begin{cases} 0 & \text{for } \varepsilon_c \leq \varepsilon_{c0} \\ 1 - \dfrac{20.97\varepsilon_c + 159592(0.0048 - \varepsilon_c)^{3.02} - 0.0054}{10000\varepsilon_c^2} & \text{for } \varepsilon_{c0} < \varepsilon_c \leq \varepsilon_{cu} \\ 1 - \dfrac{20.97\varepsilon_c + 1152(\varepsilon_c - 0.0048)^{2.17} - 0.0047}{10000\varepsilon_c^2} & \text{for } \varepsilon_{cu} < \varepsilon_c \leq \varepsilon_{c1} \\ 1 - \dfrac{20.97\varepsilon_c + 54(\varepsilon_c - 0.0048)^{1.46} - 0.0093}{10000\varepsilon_c^2} & \text{for } \varepsilon_c > \varepsilon_{c1} \end{cases} \tag{3.5}$$

Fig. 3.4(a) shows the curve of the tension damage variable (d_c) and tensile strain (ε_t).Based on evidence from the uniaxial tensile tests, when the tensile strain (ε_t) reaches 3%, visible cracks appear. Submitted tensile strain value into in Eq.3.4 gives a tension damage variable of 0.965. In other words, it can be considered that the crack propagates when the tension damage variable exceeded 0.965.

Combining Eq.3.4 and Eq.3.5, it is noticed that there is no damage within the elastic area, with the damage appearing only in the inelastic area.

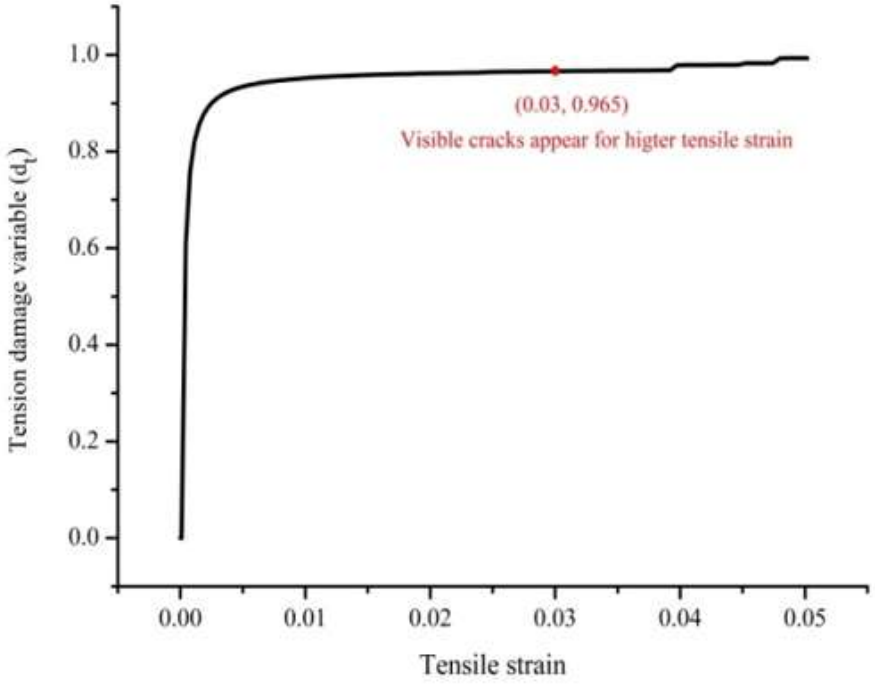

(a) Tension damage variable model

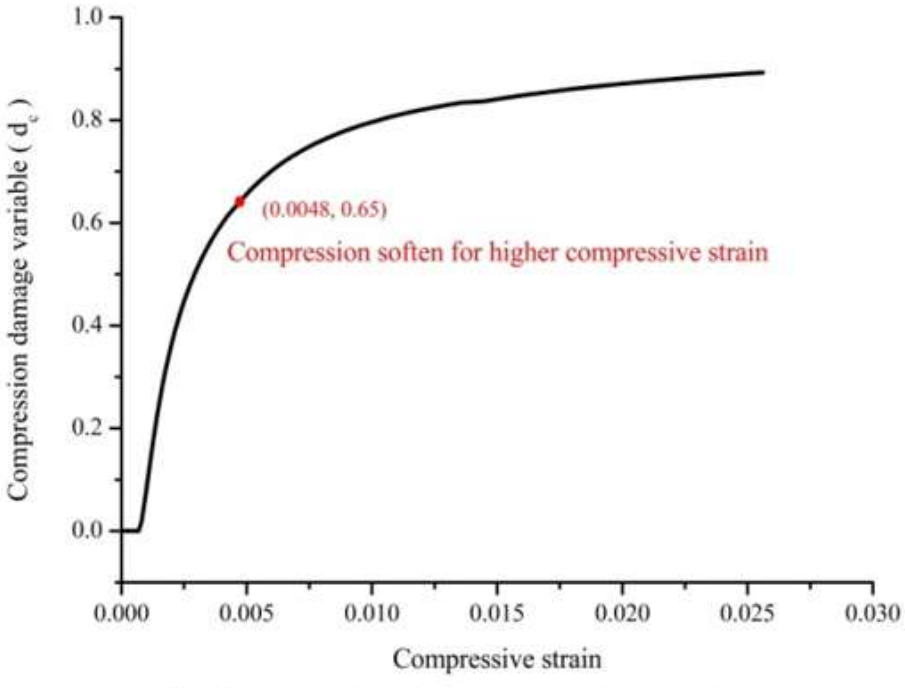

(b) Compression damage variable model

Figure 3.4: Tension and compression damage variables versus strain

Fig. 3.4(b) shows the curve of the compression damage variable (d_c) and compressive strain (ε_c).The compression damage variable corresponding to the ultimate compressive stress (σ_{cu}) is 0.65. It means that when compressive material damage exceeds 0.65, the compressive stress begins to decline.

With these two damage variable models, the CDP model can simulate the tension and compression damage distribution in the SHCC material under different complex load situations.

3.3 Yield criterion

As described in section 2.1.2, to modify the yield criterion for the SHCC core, the value of the parameter α, β, and γ should be deduced.

The formulation of the yield criterion (Eq.2.12) in Chapter 2 leads to two different formulations, depending on the sign of $\overline{\sigma}_{max}$,i.e. if the stress state is under tension ($\overline{\sigma}_{max} > 0$) or compression ($\overline{\sigma}_{max} < 0$)[91].

In the case of a tensile stress state ($\overline{\sigma}_{max} > 0$), Eq.2.12 reduces to

$$\frac{1}{1-\alpha}(\sqrt{3J_2} + \alpha I_1 + \beta\overline{\sigma}_{max}) = c \tag{3.6}$$

In the case of a biaxial compressive stress state ($\overline{\sigma}_{max} = 0$), Eq.2.12 results in

$$\frac{1}{1-\alpha}(\sqrt{3J_2} + \alpha I_1) = c \tag{3.7}$$

while in a triaxial compressive stress state ($\overline{\sigma}_{max} < 0$) it gives

$$\frac{1}{1-\alpha}(\sqrt{3J_2} + \alpha I_1 + \gamma\overline{\sigma}_{max}) = c \tag{3.8}$$

The parameter α is calibrated by the equibiaxial compressive yield stress σ_{bu} and the uniaxial compressive yield stress σ_{cu} as

$$\alpha = \frac{(\frac{\sigma_{bu}}{\sigma_{cu}}) - 1}{2(\frac{\sigma_{bu}}{\sigma_{cu}}) - 1} \tag{3.9}$$

and the parameter β is calibrated by the uniaxial tensile yield stress σ_{tu} and σ_{cu} as

$$\beta = \frac{\sigma_{cu}}{\sigma_{tu}}(1-\alpha) - (1+\alpha) \tag{3.10}$$

Furthermore, the parameter γ is calibrated under a triaxial compressive stress state by the parameter K_c, given as the ratio of the second stress invariant on tensile meridian (TM) and on compressive meridian (CM) as a given hydrostatic pressure as

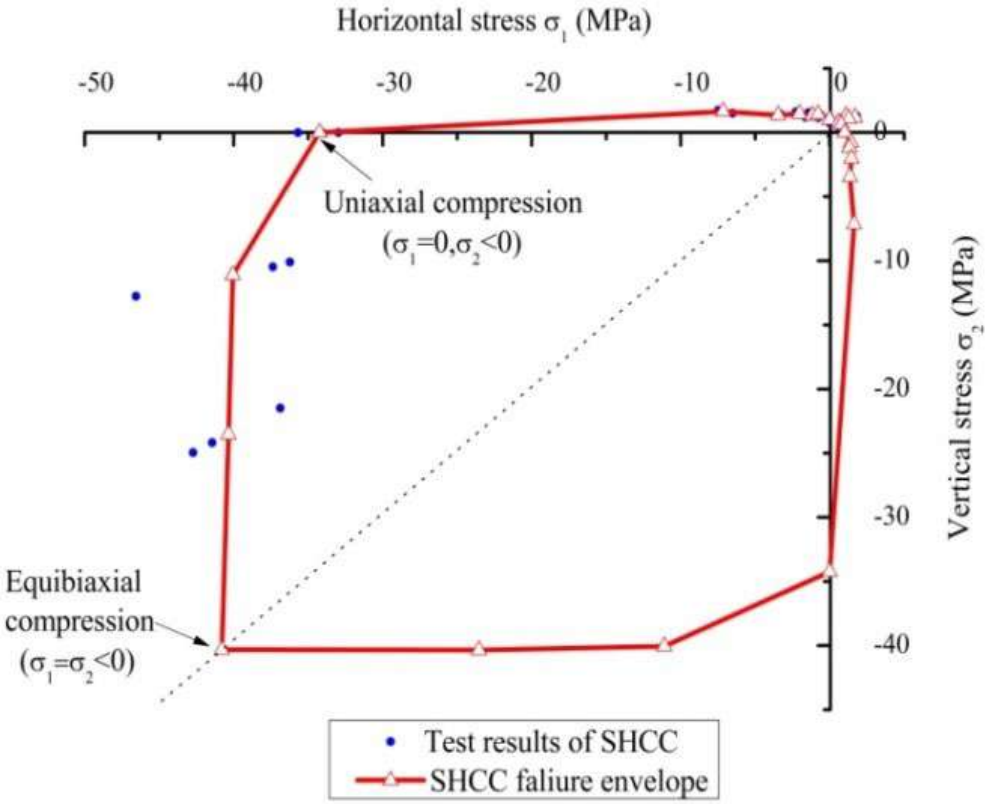

Figure 3.5: Biaxial failure envelope of an SHCC material based on test data [11]

$$\gamma = \frac{3(1 - K_c)}{2K_c - 1} \tag{3.11}$$

To sum up, the value of β is corresponding to the value of α. And α and β are according to σ_{b0}, σ_{c0} and σ_{t0}. The value of α and β are calibrated in plane stress conditions, which are the key parameters of the yield criterion in plane stress state. The parameter γ is the key parameter of the yield criterion in a three-dimensional stress state condition, and its value is a function of K_c in a triaxial compressive stress state.

Finally, to define the values of α, β and γ , the results from uniaxial tensile, uniaxial compressive, biaxial compressive and triaxial compressive tests should be used. Particularly, for the value of α, the equibiaxial compressive yield strength should be obtained from experiments. Until now, there is little research about equibiaxial compressive behavior on SHCC materials.

Swanepoel [11] studied the behavior of SHCC materials under biaxial loads. A comprehensive research concerning biaxial loads on different directions was presented. The research considered symmetry conditions, and the half plane was divided into 13 directions and three square specimens were used for each direction. However, further study is needed to extend the experimental results obtained in this

research. Based on the test data, the biaxial failure envelope can be obtained as shown in Fig. 3.5, where σ_1 is the horizontal stress (with $\sigma_1 > 0$ representing tensile stress and $\sigma_1 < 0$ a compressive stress), σ_2 is the vertical stress (being tensile with $\sigma_2 > 0$ and compressive with $\sigma_2 < 0$).

The compressive yield stress (σ_{bu}) in an equibiaxial stress state (when $\sigma_1 = \sigma_2 < 0$) and uniaxial compressive σ_{cu} (when $\sigma_1 = 0, \sigma_2 < 0$ can be obtained from the failure envelope in Fig. 3.5. The value of the ratio $\frac{\sigma_{bu}}{\sigma_{cu}}$ was then calculated as 1.18. Submitting this ratio in Eq. 3.9, the parameter α is calculated as 0.13. Submit the value of α and the values of uniaxial tensile yield stress σ_{tu} and σ_{cu} in Eq.3.10. The value of the parameter β was calculated as -1.01. Finally, the value of γ, is related to the parameter K_c (Eq.3.11).

The calculation of the parameter was first recommended by Lubliner for the classic CDP model. For plain concretes, the typical value of K_c ranges from 0.5 to 0.8. Based on the Lubliners classic CDP model, several results of K_c were deduced based on experiments. The value of K_c was calculated as 0.5 by Ottosen [92], 0.64 by Schickert and Winkler [93], 0.66 by Richart [94], and 0.8 by Mills and Zimmerman [95]. All these results were obtained from tests under biaxial loads, cyclic loads, and bending loads, respectively. The value of K_c influences the shape of the yield surface in the deviatoric stress plane under a triaxial stress state as shown in Fig. 3.6.

For the fiber reinforced concrete, many researches were carried out on the value of K_c. Typically, in the paper of Chi et al. [39], they concluded that, in the situation of low hydrostatic stress, $K_c = 2/3$ is appropriate, while, in high hydrostatic stress situation, $K_c = 0.7$.

3.4 Plastic flow rule

As described in section 2.1.3, to modify the flow rule for the SHCC core, the value of the dilation angle (ψ) should be deduced.

The potential function G, expressed in Eq.2.15 in section 2.1.3, has a Drucker-Prager type hyperbolic form, as shown in Fig. 3.7. It can be observed that the plastic potential tends to a straight line as the eccentricity tends to zero. The non-associative plastic potential dilation angle (ψ) is a significant parameter influencing the flow rule.

The determination of the dilation angle (ψ) is based on a series of confined triaxial compressive experiments.

According to the description in ABAQUS [35], as shown in Fig. 3.8, the points in the stress-strain curves corresponding to the ultimate elastic strength were chosen

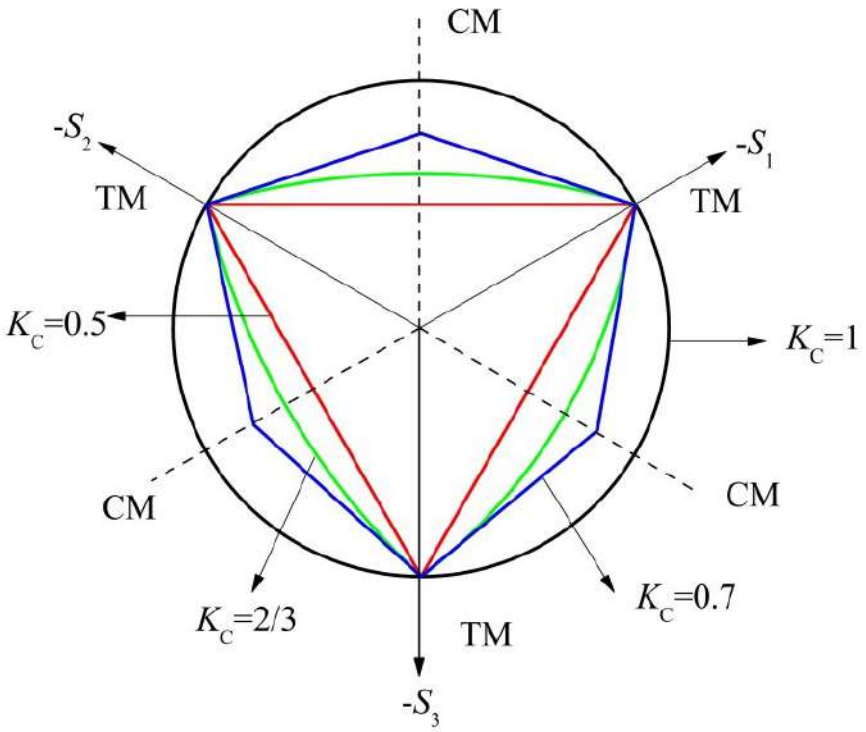

Figure 3.6: Yield surface in the deviatory plane for different K_c

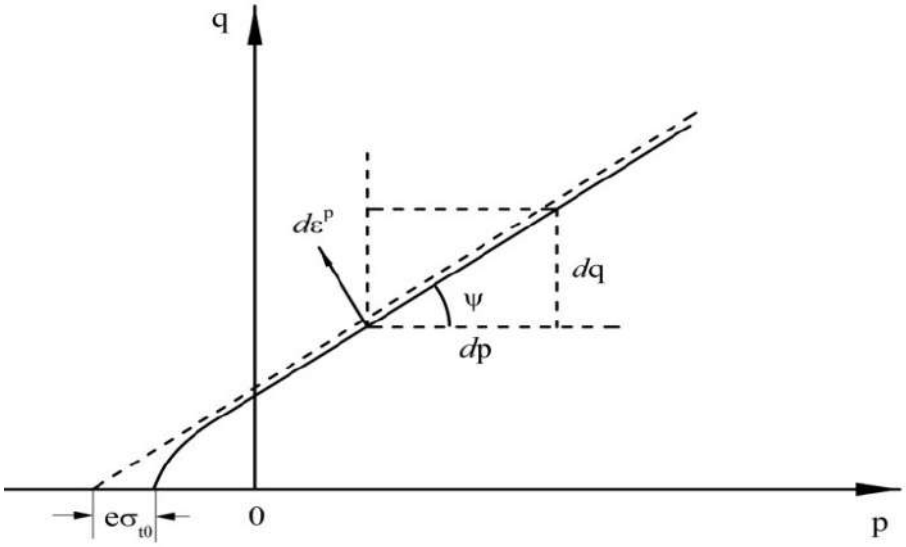

Figure 3.7: Surface of the plastic potential in meridional plane

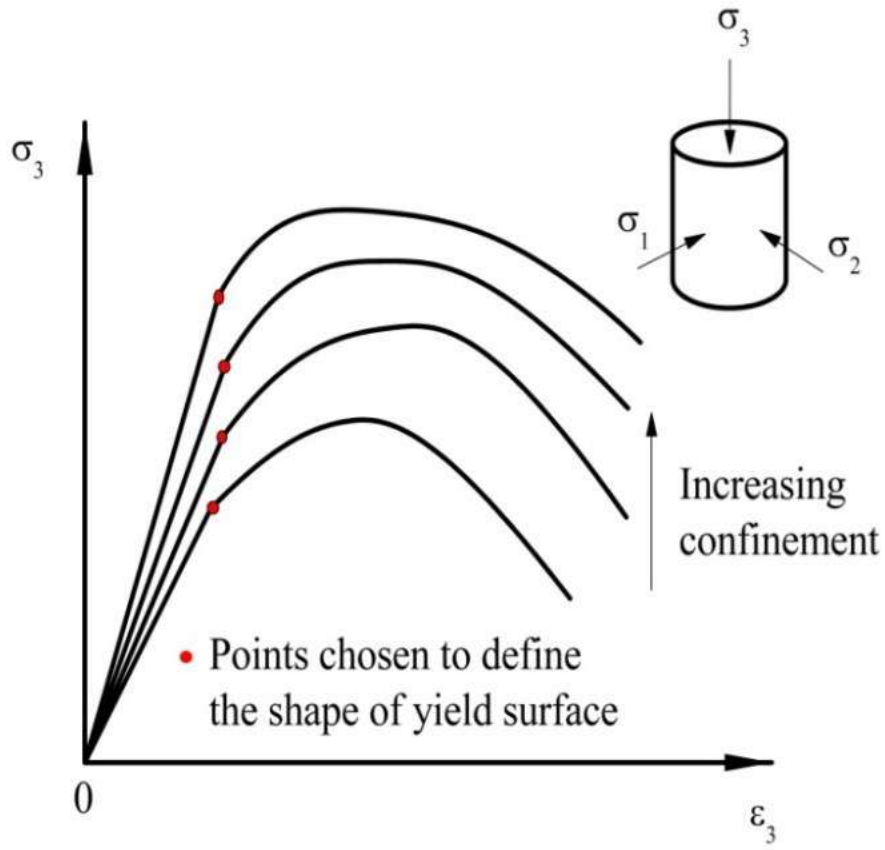

Figure 3.8: Typical points in stress-strain curves used to calculate the dilation angle ψ [49,50]

to define the shape of the yield surface based on the reference of [96, 97].

3.4.1 Triaxial test setup

To calibrate the dilation angle ψ, the triaxial compressive experiments were conducted in the present study.

Fig. 3.9 shows the experimental setup for the triaxial compressive tests. Compared to the uniaxial compressive test, the specimen was installed in a metal warehouse to withstand the confined stress, and a hydraulic pump was used to change the oil confining pressure in the warehouse. The confining stress is $\sigma_1 = \sigma_2$ and σ_3 is the applied compressive stress.

Finally, the confining stress of 3.45 MPa (500 psi) and 6.89 MPa (1,000 psi) were conducted. Under each confined condition, three cylindrical specimens, 50 mm in diameter and 100 mm in height, were used. The axial deformation speed was 0.02 mm/min and the displacements were measured by an LVDT during the tests.

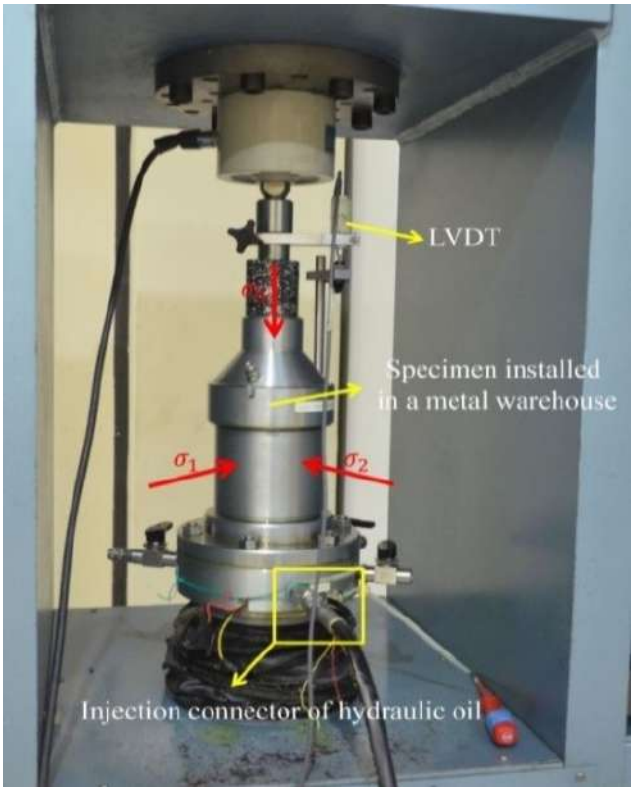

Figure 3.9: Triaxial compressive tests setup

3.4.2 Results and calculation

The final results are shown in the Fig. 3.10. From the results, it is concluded that with the increase of the confining stress the compressive stress is synchronous increase. All the curves can be divided into the elastic phase and the plastic phase.

The uniaxial compressive stress-strain curve measured in section 3.2.1, which equates to under zero confine pressure is also used for the calculation.

The turning points corresponding to the ultimate elastic stress were obtained as shown in Fig. 3.10, in which the exact value is shown in Table 3.5.

Table 3.5: The representation of the turning points

Confining stress	σ_1	σ_2	σ_3	p	q
0MPa	0	0	13.60	4.53	13.60
3.45MPa	3.45	3.45	18.33	8.41	14.88
6.89MPa	6.89	6.89	25.21	12.99	18.32

The representation of the stress components in three directions in the meridional plane p-q can be expressed as

$$p = \frac{1}{3}(\sigma_1 + \sigma_2 + \sigma_3) \tag{3.12}$$

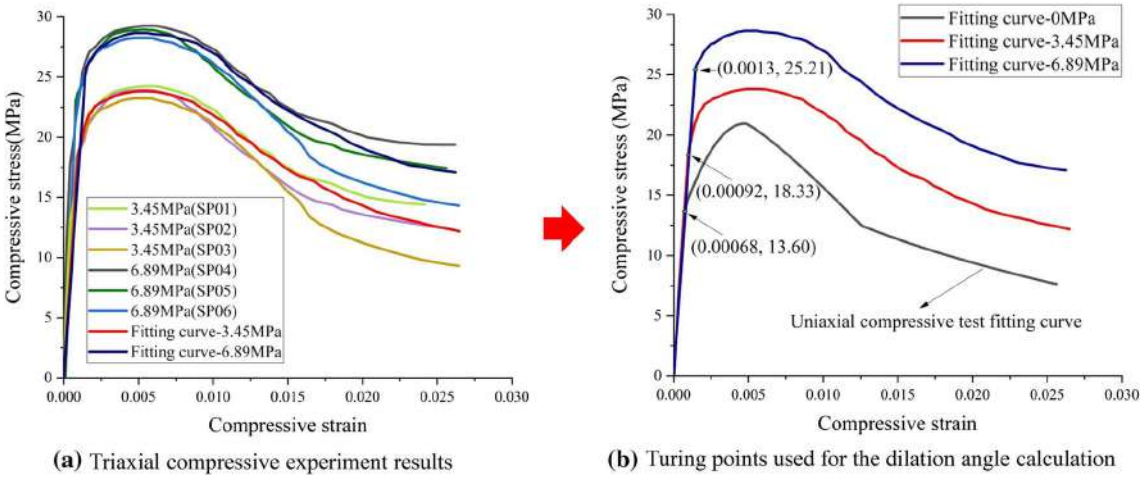

(a) Triaxial compressive experiment results

(b) Turing points used for the dilation angle calculation

Figure 3.10: Triaxial compressive tests results

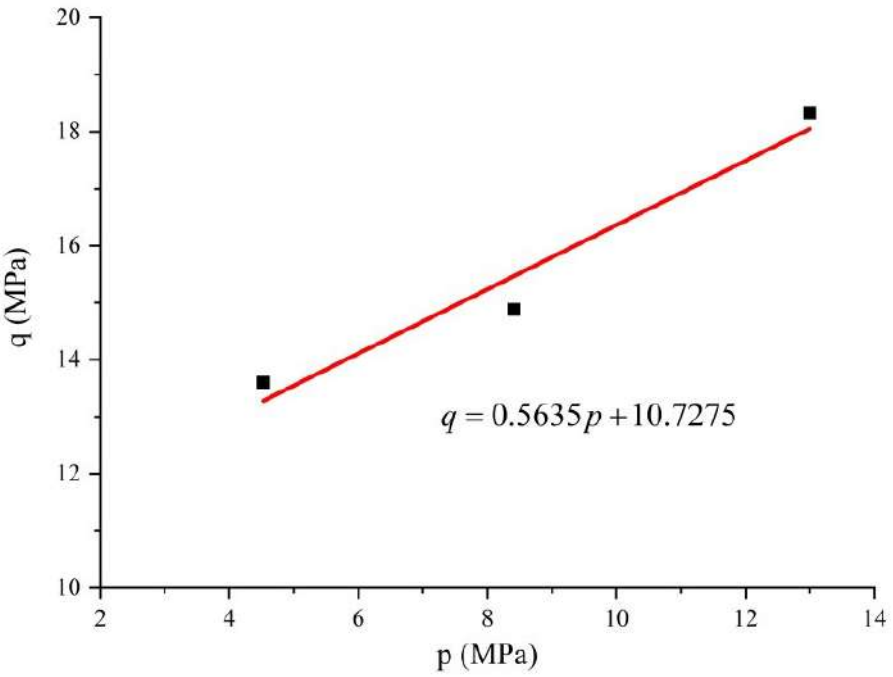

Figure 3.11: Fitting curve

$$q = \sigma_3 - \sigma_1 \tag{3.13}$$

After identifying the turning points in the p-q plane, shown in Fig. 3.11, the fitting equation is deduced as

$$q = 0.5638p + 10.7275 \tag{3.14}$$

where $tan\psi$=0.5638 and, finally, that ψ assumes an angle of 29.4°.

3.5 Summary

A modified concrete damage plasticity (CDP) model of an SHCC material employed as the annular layer of sandwich pipes (SPs) has been developed based on experiments and the classic continuous damage theory.

The model was built in three parts, associated to the damage evolution, yield criterion, and plastic flow rule.

Based on the obtained results the following conclusions are presented.

- The SHCC material presents a tensile hardening region during the uniaxial tensile experiments, which can greatly improve the resistance to crack propagation for SPs under bending.

- Based on the uniaxial tensile stress-strain curves and classic continuous damage theory, the tension damage variables for the theoretical model can be deduced as shown in Eq. 3.4 . With the tension damage variables model, the tensile damage distribution in the SHCC material can be simulated.

- Based on the uniaxial compressive stress-strain curves and classic continuous damage theory, the compression damage variables for the theoretical model can be deduced as shown in Eq. 3.5. With the compression damage variables model, the compressive damage distribution in the SHCC material can be simulated.

- Through the theoretical analysis and biaxial compressive experiments, the value of the parameter $\frac{\sigma_{bo}}{\sigma_{co}}$ was calculated as 1.18. According to the yield criterion for the SHCC material, value of K_c was calculated as 0.667.

- Based on reported triaxial compressive experimental data with the Drucker-Prager type hyperbolic form, the dilation angle of the SHCC plastic flow rule was calculted as 29.4°.

Chapter 4

Verification tests for the CDP model

4.1 Introduction

The modified CDP model for the SHCC material will be applied in the numerical simulations of sandwich pipes (SPs), using a finite element (FE) model. To verify the accuracy of the model, the specific experiments are reported in this chapter.

Four-point bending tests are performed, and the results from the numerical simulations and the experimental data are correlated.

Also, the results from the collapse tests are correlated with the numerical simulation results under two different bonding conditions for the interlayer behavior: fully bonded and unbonded conditions.

4.2 Parameters of the modified CDP model

Based on the formulation of the CDP model described in Chapter 3, the parameters of the modified model were calculated. These parameters are shown in Table 4.1.

4.3 Four-point bending numerical-experimental correlation

To verify the accuracy of the CDP model for the SHCC material, the specific specimens were designed, and the four-point bending experiments were performed.

Table 4.1: The parameters of the CDP model for the SHCC material

$E_0(GPa)$	20	Dilation angle $\psi(\circ)$	29.4	α	0.13
Poisson ration μ	0.2	$\frac{\sigma_{b0}}{\sigma_{c0}}$	1.18	β	-1.01
Eccentricity e	0.1	K_c	0.667	γ	2.99

Stress σ_c/MPa	Strain ε_c	Inelastic strain ε_c^{in}	Damage variable d_c	Stress σ_t/MPa	Strain ε_t	Cracking strain ε_t^{ck}	Damage variable d_t
13.64	0.00068	0	0	1.76	0.000088	0	0
15.17	0.0012	0.00041	0.14	1.79	0.00044	0.00035	0.609
16.98	0.0018	0.00092	0.32	1.82	0.00079	0.00070	0.759
18.85	0.0025	0.0015	0.45	1.91	0.0017	0.0018	0.876
20.97	0.0048	0.0038	0.65	2.16	0.0045	0.0046	0.931
20.34	0.0059	0.0049	0.69	2.74	0.030	0.030	0.965
19.32	0.0068	0.0058	0.72	2.58	0.039	0.039	0.967
16.74	0.0088	0.0080	0.78	2.23	0.041	0.041	0.993
14.83	0.011	0.010	0.81	2.06	0.042	0.042	0.994
12.80	0.013	0.012	0.82	1.71	0.044	0.044	0.994
9.23	0.020	0.019	0.87	1.01	0.048	0.049	0.995

Then, the finite element model was built for the simulation. The mechanical behavior and the damage distribution in the SHCC material obtained from the experiments and numerical simulations were compared in detail.

4.3.1 Experimental setup for the four-point bending tests

Fig. 4.1 shows shows the experimental setup for the four-point bending tests, with specimens with length 400 mm, width 60 mm, and thickness 12.5 mm. The spans between the two lower support points and two upper loading points are 300 mm and 100 mm, respectively.

The tests were performed with two SHCC specimens to obtain values of bending force and flexibility. 4-axis bending test machine was used to apply a vertical displacement speed of 0.03 mm/min. The specimens were simply supported on the two lower support points.

The applied force (F) and related displacement (D) were measured by a load cell and an LVDT positioned in the bending apparatus.

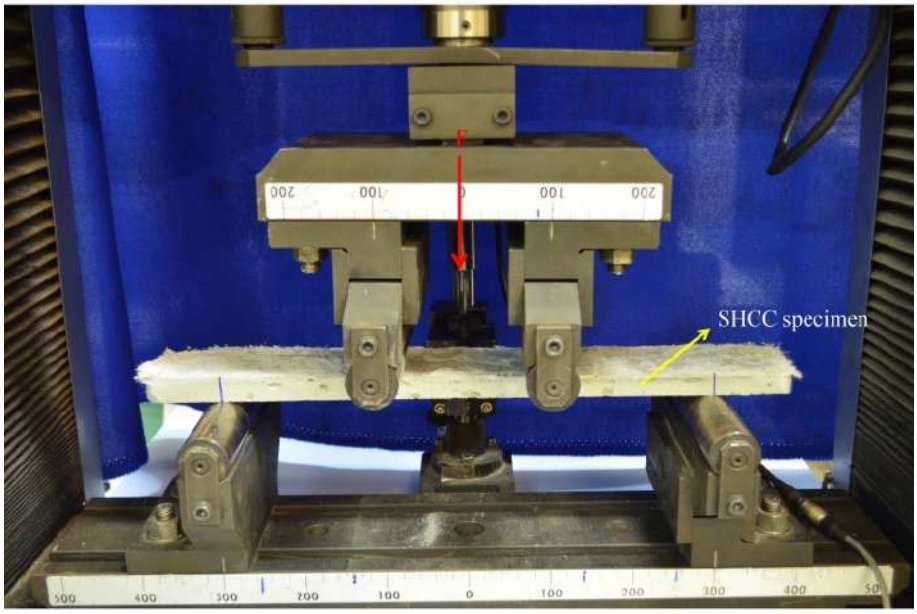

Figure 4.1: Four-point bending setup

4.3.2 Numerical simulation

Fig. 4.2 shows the finite element (FE) model of the four-point bending, with the aspect ratio of the elements set as 1. The FE mesh was generated with the CPS4R element type. A mesh-sensitivity analysis was carried out considering the effect of the element size on the results. Finally, the FE mesh comprises 400 elements in length (x-axis) and 10 elements in height (y-axis).

The two upper loading blocks and two lower support blocks were set as rigid bodies with four corresponding reference points (RP). The rigid body surfaces were set as master surfaces, and the SHCC specimen surfaces were set as slave surfaces within a contact interaction model.

For boundary conditions, the SHCC specimen was simply supported on the two lower support blocks (RP-3 and RP-4), which were assumed as fully fixed. During the simulation, the displacement was prescribed vertically at the two upper loading blocks (RP-1 and RP-2).

4.3.3 Results and discussion

Fig. 4.3 correlates the curves of applied force versus displacement of the tested specimens with those obtained from the numerical simulation. In both the elastic regime and plastic hardening region, the numerical results present good agreement with the experiments. In the softening region (unloading), the simulation results are in between the experimental values.

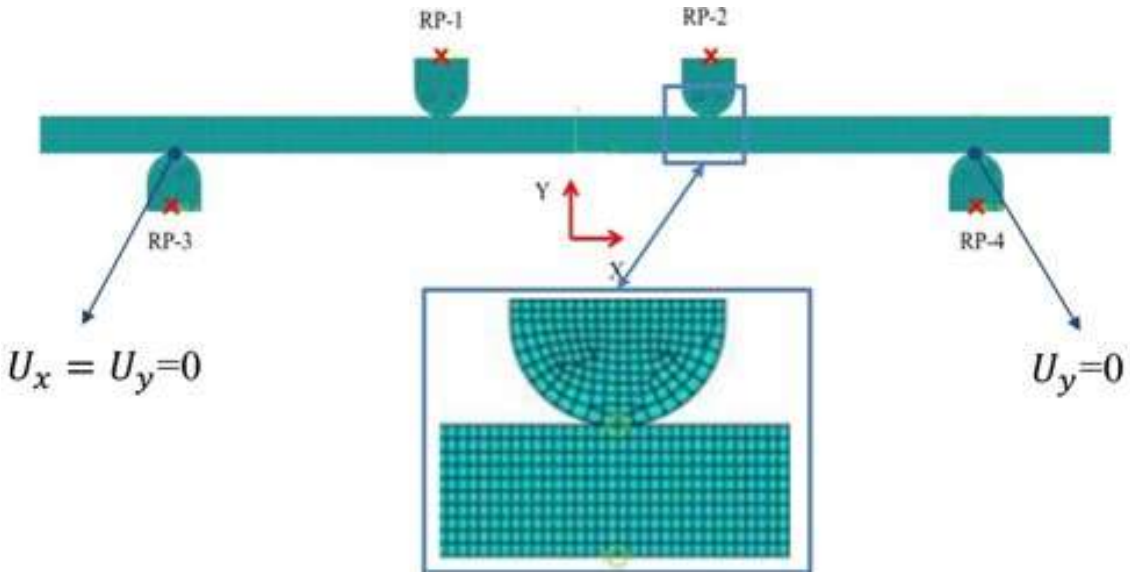

Figure 4.2: FE model for the four-point bending

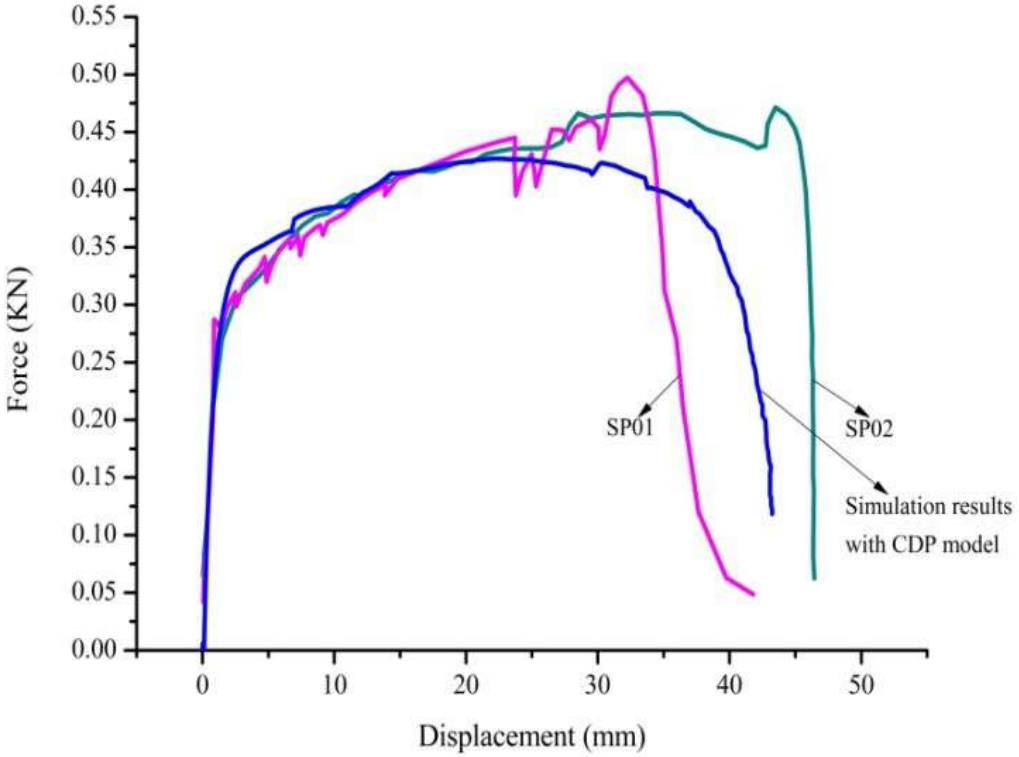

Figure 4.3: Applied force versus displacement of the tested specimens and numerical model

Concerning the experimental results, the two specimens show almost the same tendency in the elastic region and plastic hardening region, but they behave differently in the softening region. These phenomena can be explained based on the uniaxial tensile experiments, with visible multiple cracks appearing in the softening region after the first crack propagation, the specimens become very unstable. The cracks appear randomly located in the tests and are associated with the fibers distribution during the manufacturing process. Also, the damage has already existed in the specimen during the manufacturing process. So the bearing capacity of the specimens will be unstable after the main crack propagation in the plastic hardening region.

Fig. 4.4(a) shows the two tested specimens, SP01 and SP02, that showed failures combining tensile and compressive damages. The tensile damage behaves clearly with one main crack and many small cracks around. For the SHCC material, the mechanism of tensile damage is mainly due to the development of microcracks which already existed due to the manufacturing process.

As mentioned in section 3.2.2, the visible cracks appear and propagate for tensile damage values higher than 0.965. Fig. 4.4(b) shows the results of the numerical simulation with the crack region under tensile bending. The numerical results reflect all the possible crack areas, which can match the crack area shown in the Fig. 4.4(a) from the tests.

For the compressive damage, there are no obvious characteristics of the specimens about the compressive damage during the experiments. However, based on the simulation as shown in Fig. 4.4(c), it can be observed that the top part of the specimens was damaged under compression due to bending.

Based on the correlation of the simulation results and test results, it can be concluded that the CDP model can be used to reproduce the mechanical behavior and predict the damage distribution in an SHCC material.

4.4 Correlation study for the collapse of sandwich pipes

To verify the applicability of the CDP model for the SHCC in sandwich pipes, the collapse experiments were performed. The collapse pressure (P_{co}) was gotten from the experiments was correlated with the simulation results from the numerical simulation.

To eliminate the influence of the actual interlayer behavior of the SPs, the simulation was done under two extreme cases as a fully bonded condition and unbonded condition.

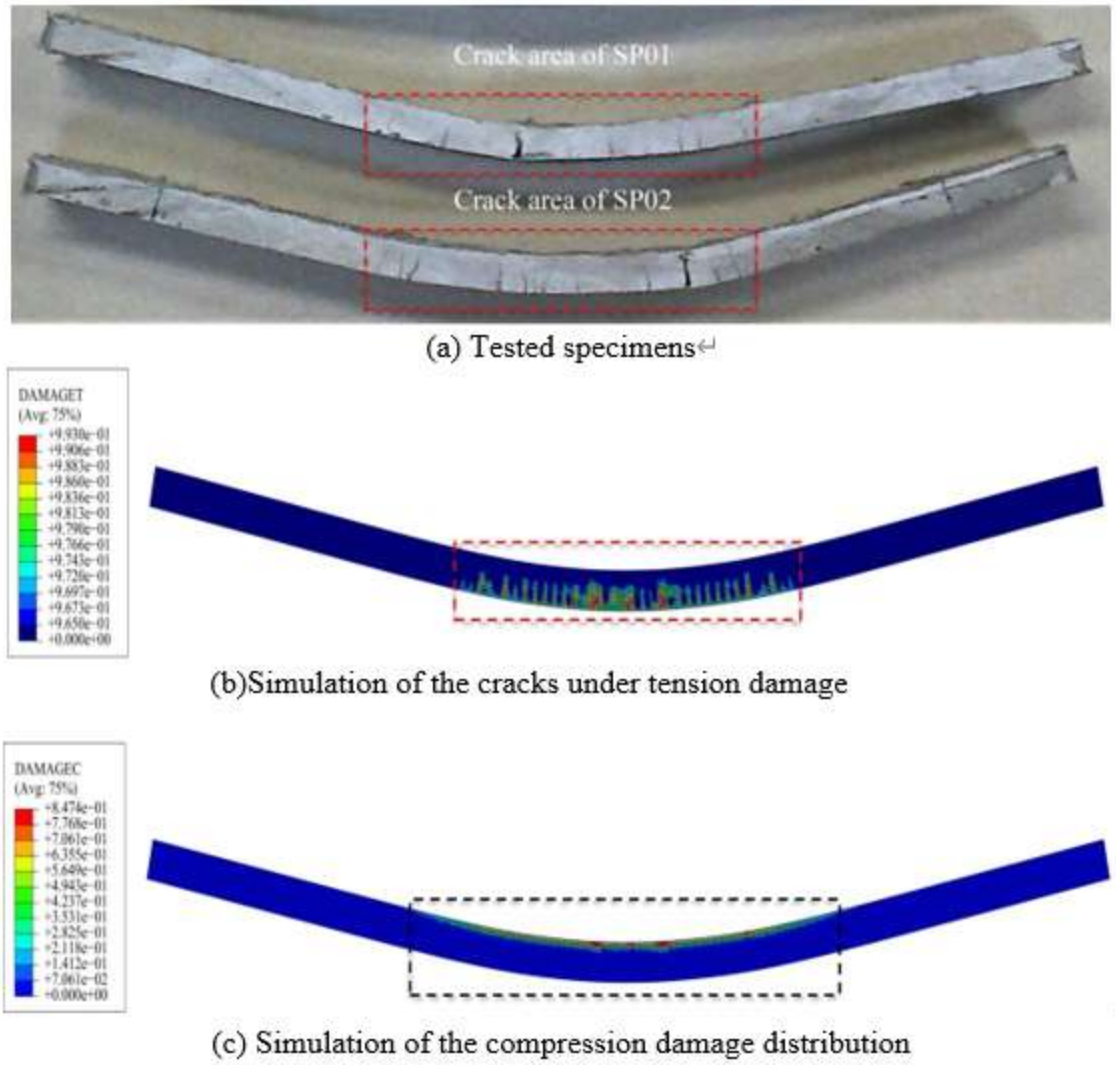

Figure 4.4: Tested specimens and the damage areas distribution of simulation

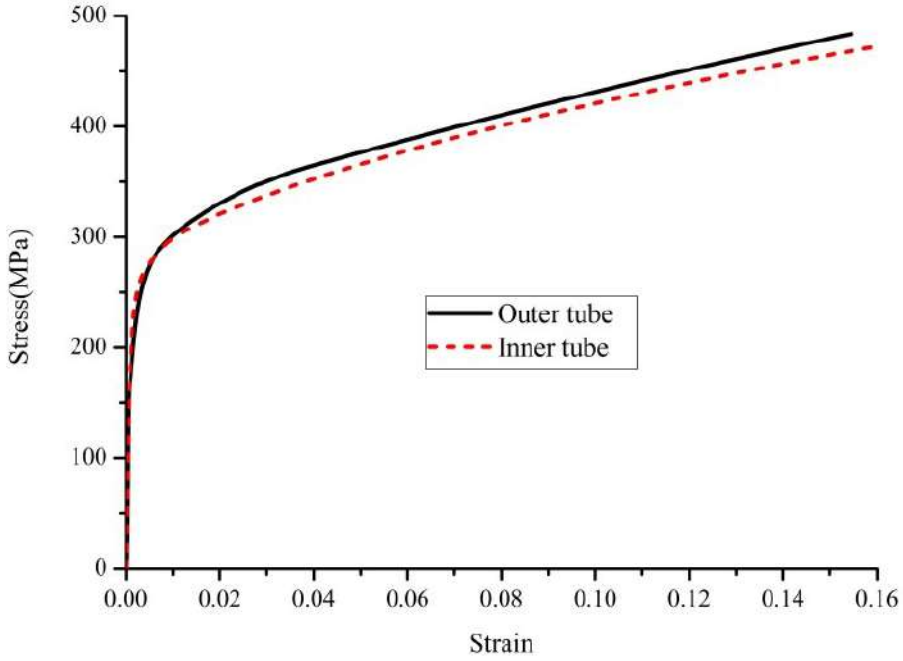

Figure 4.5: Stress-strain curves for SS304 outer and inner tubes

4.4.1 Collapse experiments

Four sandwich pipes have been built using stainless steel 304 for inner and outer tubes, with Young's modulus 200 GPa and Poisson coefficient 0.3. The standard uniaxial tensile of the two tubes are made to define the material property. Stress-strain curves from specimens of the two tubes are shown inFig. 4.5.

The nominal external diameters are 8 in and 6 in for the outer and inner pipes, respectively, and the thicknesses 2.0 mm. The thickness of the SHCC core is 23.4 mm. The initial ovality ($\triangle_0$) of the sandwich pipe which influences its collapse pressure, is defined as

$$\triangle_0 = \frac{D_{max} - D_{min}}{D_{max} + D_{min}} \tag{4.1}$$

where, D_{max} and D_{min} represent the maximum and the minimum diameters in the cross-section. The measured data of the four sandwich pipe samples are shown in Table 4.2.

A hyperbaric chamber with a working pressure capacity of 50 MPa has been employed for the external pressure tests. The pressure inside the chamber was controlled and monitored by an outside water pump and an inside pressure transducer. The rate of the applied pressure was 0.4 MPa/min. The collapsed configuration of the SP1 sample is shown in Fig. 4.6.

Figure 4.6: Tested SP1 sandwich pipe

4.4.2 Numerical simulation

The finite element model was built to simulate the collapse behavior of sandwich pipes under external pressure as shown in Fig.4.7.

The stainless steel 304 adopted for the inner and outer pipes was modeled according to the Hooke's law in the elastic domain and plasticity flow theory based on the von Mises yield criteria with anisotropic hardening model. The SHCC core was modeled by the former described CDP model.

The adhesion between the core and the steel tubes of the sandwich pipes has a considerable influence on the collapse pressure [3, 4, 14]. The fully bounded adhesion represents the upper bound collapse pressure.In this study, to consider the influence of the extreme adhesion condition fully bounded and unbounded adhesion conditions were simulated.

Therefore, it is expected that the experimental results are in-between these two extreme boundary conditions. The fully bounded condition between the SHCC layer and the steel pipe layers was simulated with tied surfaces. For the unbounded case, the surfaces of the pipes were defined as the master surfaces and the SHCC surface was defined as the slave one, and the small sliding option was used.

As proposed by Estefen et al. [4] and An et al.[1], the contact interaction considers the Coulomb friction model in the tangential direction and a contact pressure model in the normal direction. The tangential behavior was defined as frictionless for the unbounded layers, and the normal contact was defined as hard contact, allowing separation after the contact.

The CPE8 element type was used for the whole SP model, and a mesh-sensitivity analysis was performed to analyze the effect of the mesh size on the collapse pressure (P_{co}). Finally, the FE mesh was generated with 240 elements in the circumferential direction, one element in the radial direction for each pipe and 5 elements for the SHCC layer, as shown in Fig.4.7(a).

The initial ovality was considered in the numerical model. The external pressure was applied on the outer pipe through surface load, as shown in Fig.4.7(b).

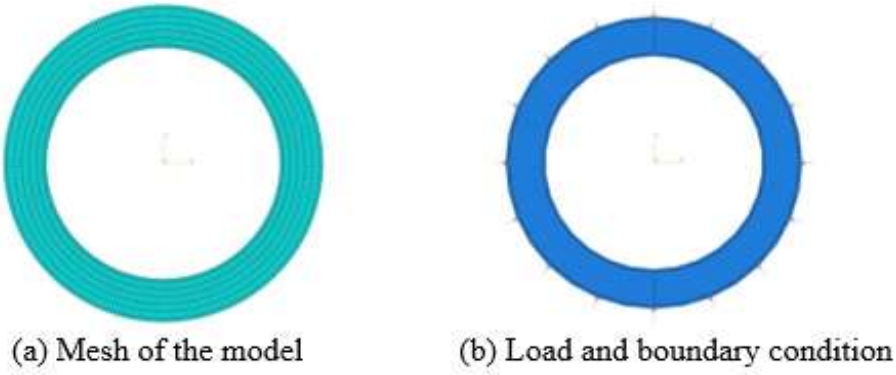

Figure 4.7: Finite element model of the SP

4.4.3 Results and discussion

By simulating the behavior of SPs under hydrostatic pressure using the ABAQUS software [35], the collapse pressure (P_{co}) obtained for SP1 for fully bounded and unbounded layers are 39.99 MPa and 34.10 MPa, respectively. The corresponding experimental collapse pressure for this sample was 37.68 MPa.

Similar results indicating the experimental collapse pressure between the simulation values for fully bounded and unbounded layers were obtained for the other three SP samples.

Numerical and experimental results are shown in Table 4.2. The values of collapse pressure (P_{co}), simulated under fully bounded condition were 39.99, 39.40, 38.09 and 36.82 MPa, which are 6.1, 5.9, 3.2 and 4.5% higher than the experimental results, respectively.

The values of (P_{co}) simulated under unbounded conditions were 34.10, 33.71, 32.88, and 32.14 MPa, which are 9.5, 9.3, 10.9, and 8.8% lower than the experimental results, respectively.

Table 4.2: Comparison between numerically predicted and experimentally observed SP collapse pressures of SPs

Pipe No.	Inital ovality (%)	P_{co} (experiments)	P_{co} (fully bounded)	P_{co} (unbounded)
SP1	0.29	37.68	39.99	34.10
SP2	0.34	37.18	39.40	33.71
SP3	0.46	36.92	38.09	32.88
SP4	0.57	35.23	36.82	32.14

Fig. 4.8 also shows the compression damage simulation results of SHCC material

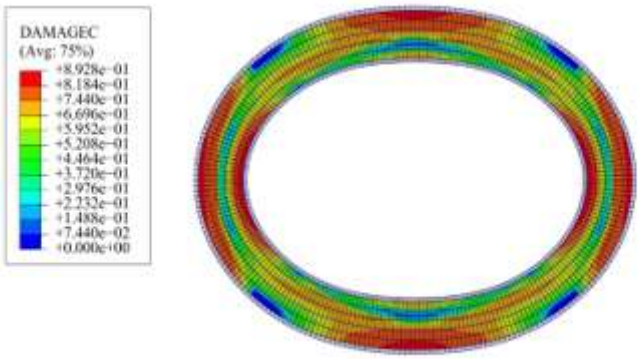

(a) SHCC damage distribution under unbounded situation for SP4

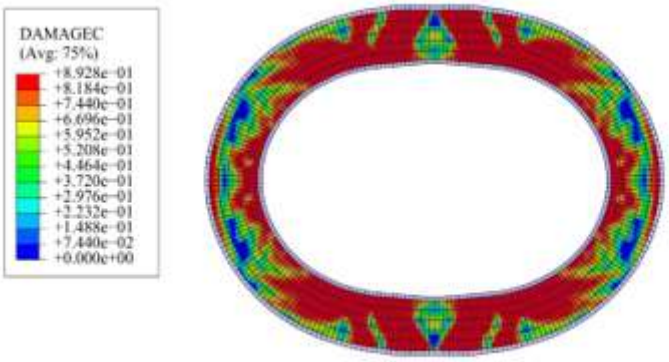

(b) SHCC damage distribution under a fully bounded situation in SP4

Figure 4.8: Compression damage simulation of SHCC in SP

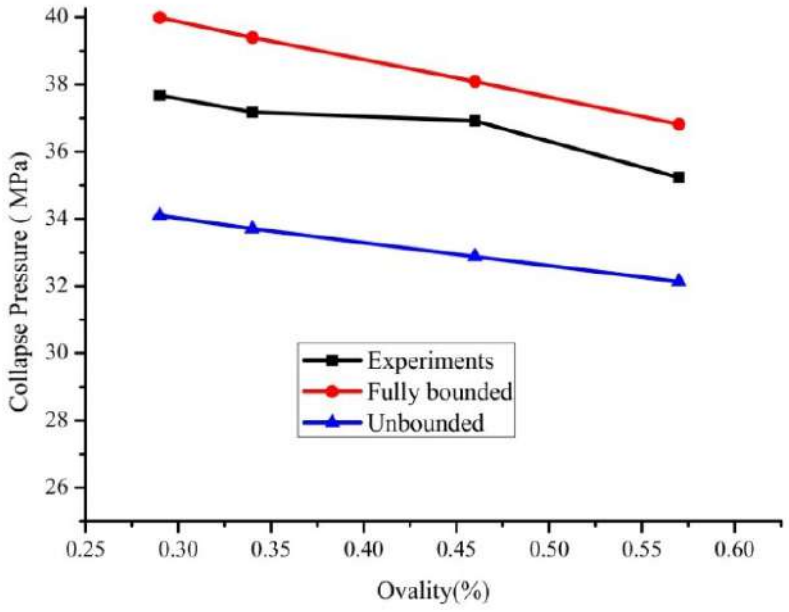

Figure 4.9: Experimental and numerical collapse pressure of SP in relation to initial ovality

in the SP for different boundary conditions. By comparison, the damaged area of the fully bounded condition is larger than the unbounded condition. The damage both starts from inner face and outer surfaces and then propagates to the middle along the radial direction.

Fig. 4.9 shows that with the increase of the initial ovality, the value of the collapse pressure decreases. The experimental results are distributed between the fully bounded and unbounded conditions. The fully bounded results are much closer to the experimental results.

The simulation results also show that the CDP model can adequately represent the mechanical behavior of an SHCC material in the annular layer of SPs.

4.5 Summary

To verify the behavior of the modified CDP model for the SHCC material and SPs, four-point bending tests are carried out on SHCC specimens and collapse tests are conducted on SP models, respectively.

Then, the results from numerical simulations, based on the finite element method, are correlated with experimental data. The correlation between numerical and experimental results are studied.

Based on the obtained results the following conclusions are presented.

- Considering results from the experiments and numerical simulations from four-point bending experiments, it can be concluded that the CDP model can be used to reproduce the mechanical behavior and predict the damage distribution in an SHCC material.

- Considering the experiments and numerical simulations of the SP collapse, as expected, the increase of the initial ovality leads to a decrease of the collapse pressure, and the CDP model can be used to simulate the mechanical behavior of an SHCC material employed in the annular of SPs, as demonstrated for SPs with fully bonded and unbonded layers.

- The experimental results remain between the numerical results with fully bonded and unbonded conditions between layers. The numerical results with the fully bounded condition are much closer to the experimental results.

Chapter 5

Experimental research on the interlayer behavior of SPs

5.1 Introduction

This chapter proposes to investigate the interlayer behavior of SPs through the specific experiments and the finite element method.

Based on the summary in Section 2.4, the push-out test is chosen to study the actual interlayer behavior of the SPs.

Also, the expansion of the SHCC core during manufacture hydration is confined by the steel tubes, thus producing self-stress associated with the expansive strain. Therefore, the self-stress measure test is designed to measure the self-stress in SHCC core.

According to the test results, the corresponding numerical model of the interlayer behavior is built. Based on the summary in Section 2.5, surface-based cohesive contact behavior in ABAQUS is chosen to simulate the experimental relationship combined with the Coulomb friction model.

5.2 Preparation for test programs

The specimens are designed and manufactured for the tests, and the material properties were measured before the tests.

5.2.1 Sandwich pipe specimen manufacture process

The manufactured SPs were used for the tests in this Chapter and the correlation study in Chapter 6. The SP manufacturing process comprises the mixture of SHCC

components and the assembly of a full-scale SP. The components of the SHCC core material were summarized by An et al. [1].

To assembly the SP, as shown in Fig. 5.1(a), the plugs consist of a metallic base and circular polypropylene body that was designed and installed at both ends of the SP with the function of sealing the annular space to hold the SHCC mixture during filling and curing. The O-rings in the plugs can prevent leakage. The thickness of the circular body is equal to the annular space of the SP specimen to be filled. Also, the plugs are responsible for keeping internal and external pipe ends concentrically. After cleaning the external and internal surfaces of the pipes with solvent, the plug was positioned at one side of the SP (defined as a bottom plug) as Fig. 5.1(b) shown.

Then, the pipes were lifted and fixed on a scaffold waiting for the filling of the SHCC mixture, as presented in Fig. 5.1(c). The vibrators were installed on the SPs to help achieve greater compactness and homogeneity of the SHCC mixture during the filling process.

A guide ring was installed at the top of the SP to guide the entry of the mixture. The SHCC mixture would be pulled in different batches, at the ending of each batch, a centralizer was introduced into the SPs annular regions, as shown in Fig. 5.1(d). The centralizer was made of SHCC mixture by the mold as Fig. 5.1(e) shown. Compressing the centralizers, the flow of SHCC mixture passes through the centralizer, which can help to remove the possibly trapped air in the annular space. A total of four centralizers were introduced in each SP sample.

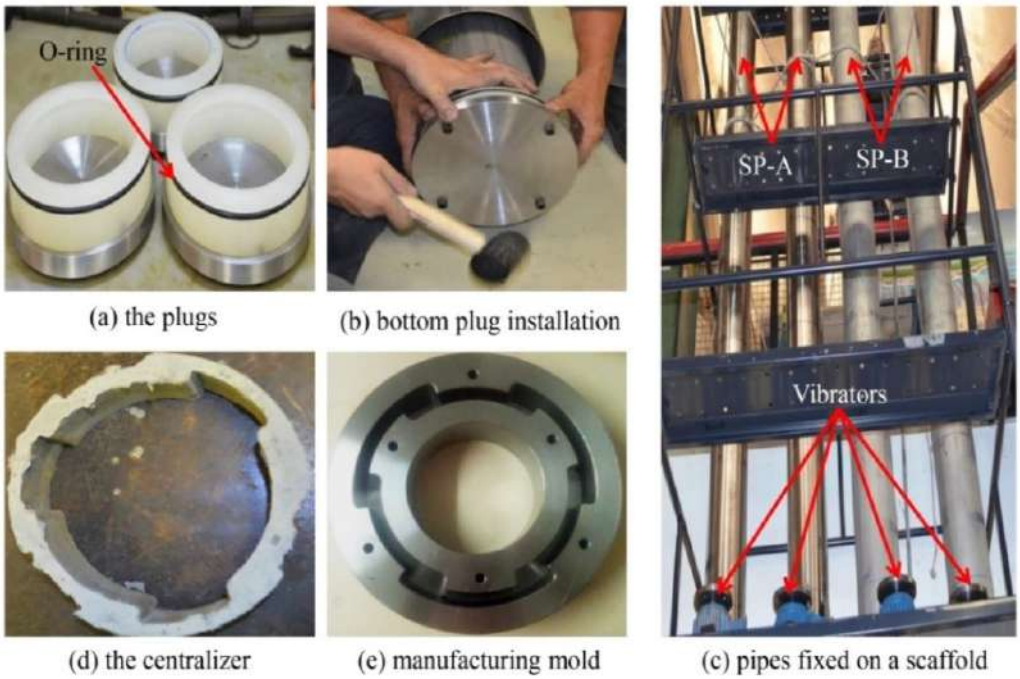

Figure 5.1: Manufacture of the SPs

When the SHCC mixture reached the upper end of the SP, the guide ring was

removed, and the upper plug was installed to maintain the humidity of the SHCC mixture during the curing. The SPs were kept at room temperature of 21 °C . After two days, the upper plugs were removed and the SPs were still positioned on the scaffold for curing with 28 days.

Two SP models were designed considering two different stainless steels for the inner and outer layers. AISI304 stainless steel tubes with smooth inner and outer surfaces were employed for the sandwich pipe specimen identified as SPA and AISI316 stainless steel tubes with rough surfaces were used in the sandwich pipe specimen referred to SPB. Table 5.1 summarizes the geometric properties of the two tested SP models. For each model, inner and outer steel tubes have the same thickness.

Table 5.1: Geometric properties of the SP models

Sandwich pipe	SP-A	SP-B
Outer diameter (mm)	203.2	219.1
Inner diameter (mm)	148.4	162.7
SHCC layer thickness (mm)	23.4	22.8
Steel tube material	AISI304	AISI316
Steel tube thickness (mm)	2.0	2.7
Tube finishing surface	Smooth	Rough
SP length (m)	7	7

5.2.2 Material properties

Standard uniaxial tension tests of the stainless steels AISI 304 and AISI 316 were performed, as shown in Fig. 5.2a. One tension test coupon was machined from each steel tube, inner and outer, respectively, for the two SP models, resulting in a total of four test coupons. A Young's modulus of 200 GPa and a Poisson ratio of 0.3 were obtained as average elastic constants. Fig. 5.2b shows the mechanical behavior of both the SS304 and SS316 specimens.

For the SHCC core, the uniaxial tensile and compressive tests were performed as described in Section 3.2.1. The built CDP model in Chapter 3 will be used in the following numerical simulation.

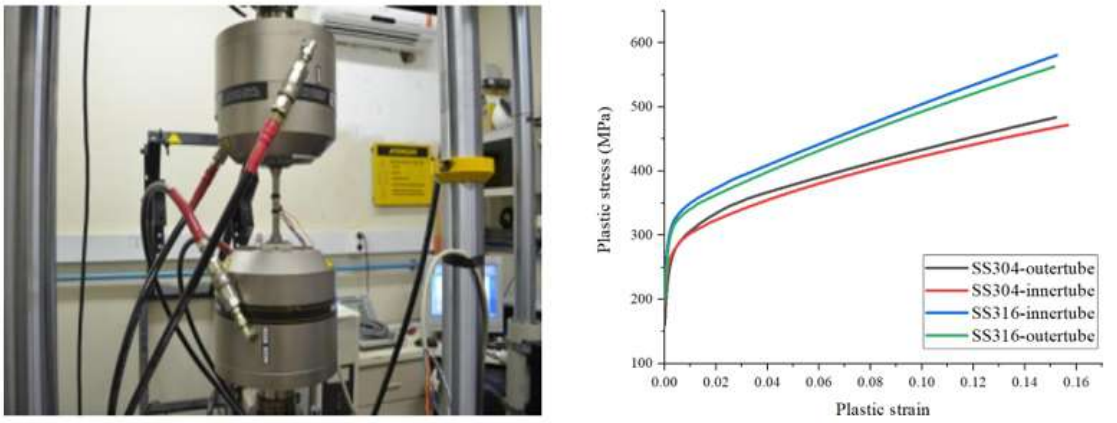

(a) Uniaxial tension test setup

(b) Mechanical properties of stainless steel.

Figure 5.2: Uniaxial tension tests and results for the steel pipe materials

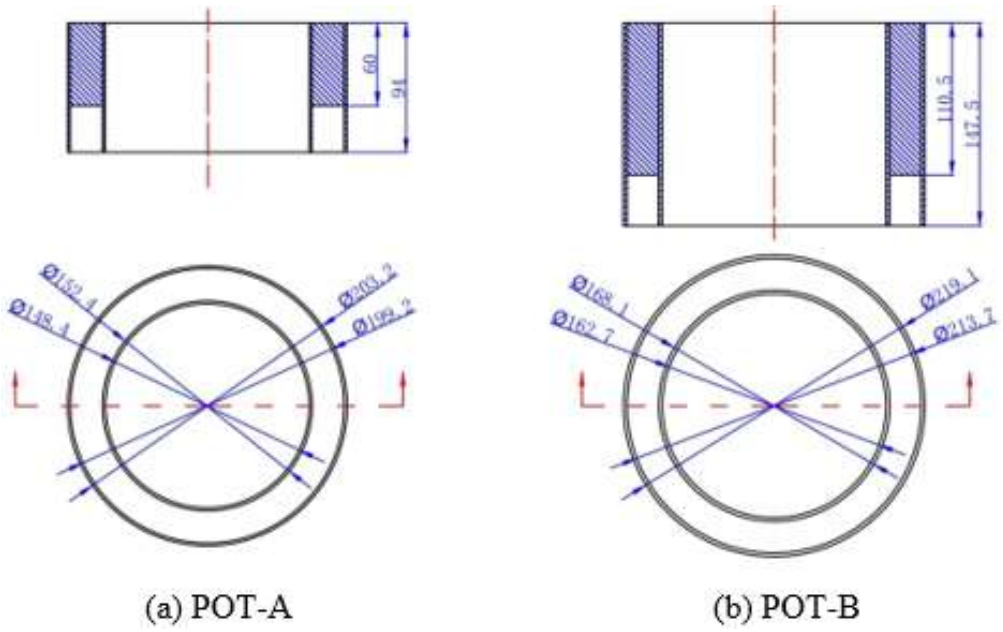

(a) POT-A

(b) POT-B

Figure 5.3: Geometries of the push-out test specimens (unit: mm)

5.3 Push-out test

For the push-out tests, two specimens were cut from the ends of the SPA and SPB models, named as POT-A and POT-B, respectively. The geometries of the specimens are schematically shown in Fig. 5.3. The length of the SHCC core was left smaller at least 30 mm than the steel tube length so that the SHCC core layer can slip in the pipe annulus (between inner and outer steel pipes) along the axial direction during the test procedure.

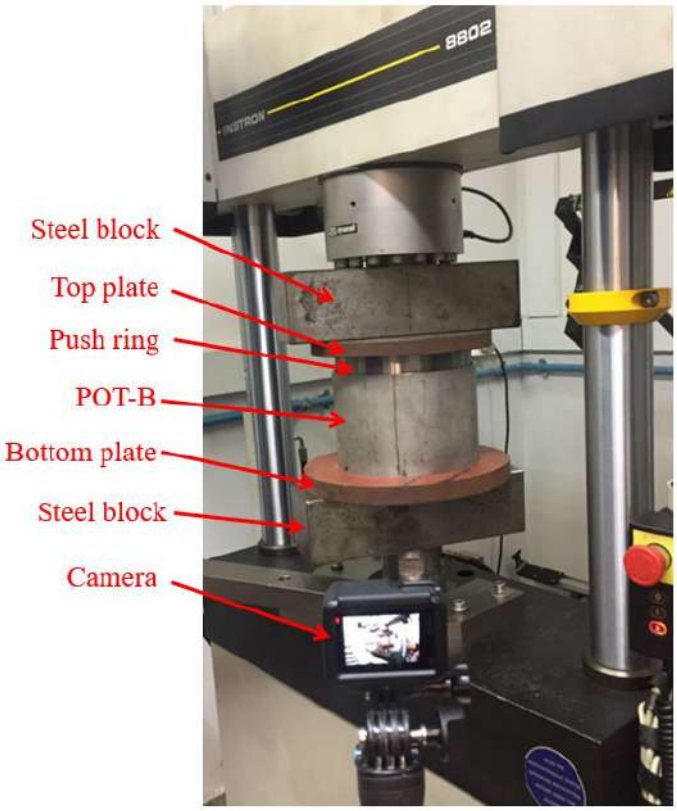

Figure 5.4: Push-out test setup for the POT-B specimen

5.3.1 Test setup

The setup for the push-out tests is shown in Fig.5.4. The tests were carried out by using a conventional servo-hydraulic machine INSTRON 8802 with a maximum load capacity of 250 kN. Top and bottom plates were used to assure that the specimens could withstand uniformly distributed loads. Two actuator rings were specially designed to push forward the SHCC core. Both rings have a height of 40mm, and outer and inner diameters, respectively, 3mm smaller and 3 mm larger than the associated SHCC cores. The actuator rings were concentrically installed on the top of the corresponding cores.

All the tests were carried out under a displacement-controlled load regime at a rate of 0.3 mm/min. The applied axial load and the displacements were recorded from the machine load cell. Each specimen was loaded until the complete slip-failure mode was attained, which was characterized when the applied load remained constant for increasing core displacements.

5.3.2 General observations

Both specimens (POT-A and POT-B) present similar behavior during loading. In the initial stage, no obvious slipping is observed between the SHCC core and the

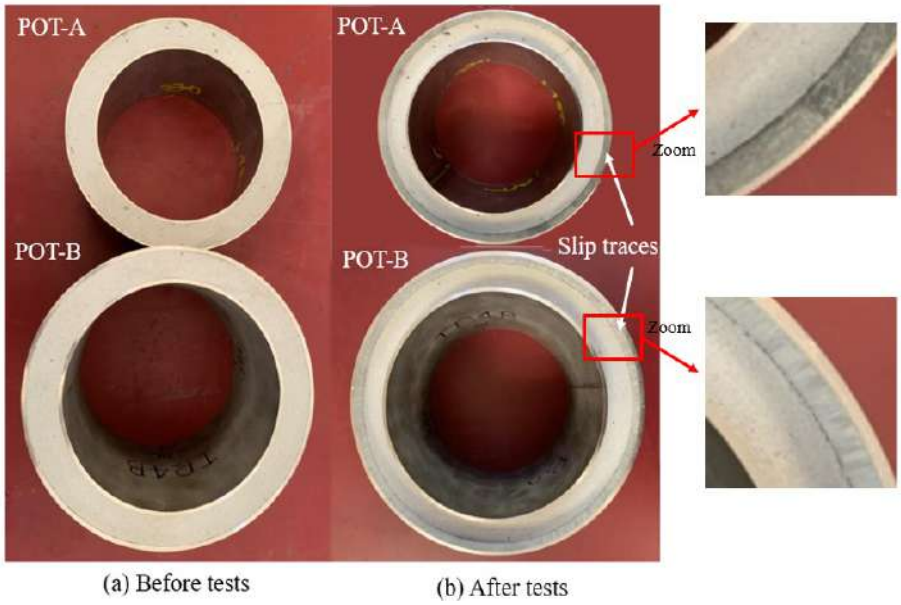

Figure 5.5: Specimens configurations before and after the tests

steel tubes. With the load increase, small slipping takes place and progresses slowly. Approaching 90% of the ultimate load, the slip dramatically increases, and when the ultimate load is reached a loud sound comes from the specimen, followed by a noticeable relative slipping. After the peak load is attained, with the relative slipping aggravating, the load drops slightly, developing a plateau until the end of the test. No buckling is observed in the steel tubes. The SHCC core keeps its integrity, and no compressive damage nor macroscopic crack is observed. Visible slip traces appear on the surface of the tubes as the slipping progresses, Fig.5.5.

5.3.3 Load-slip curves

The curves of applied load (F) versus slip displacement (S) acquired during the tests are shown in Fig. 5.6. Similar to the researches on the CFST [51], four significant points can be labeled for the identification of three stages of a typical F-S curve: A (load start), B (90% of the ultimate load), C (ultimate load), and D (test end).

The three stages can be described as:

(1) Stage AB: Initially, the curve presents a linear behavior. The applied load is primarily resisted by the adhesion between the SHCC core and the steel tubes.

(2) Stage BC: As the load increases, the slope of the curve decreases, the interlayer bond is gradually damaged and the frictional interaction force appears due to the rough surface. The applied load is resisted by both adhesive and frictional forces.

(3) Stage CD: At the ultimate load, the adhesive bond is destroyed and the frictional force acts alone. As the slipping increases, the rough surface gradually

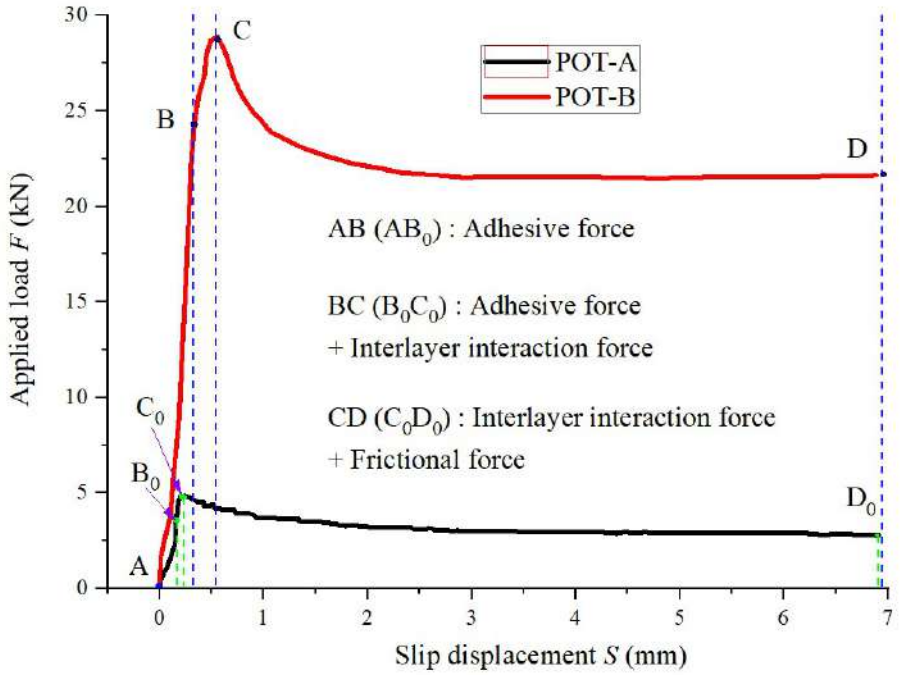

Figure 5.6: Applied load-slip displacement curve during push-out tests

becomes smoother, and, therefore, the interlayer interaction force decreases, and the curve exhibits a descending trend. When the mechanical interaction force disappears, the load is only resisted by the frictional force, and the curve presents a stable behavior as slipping progresses.

5.3.4 Relation between average bond stress and slip

According to Lu et al.[10] and Song et al.[72], the average bond stress (τ) equals to the applied load (F) divided by the contact area, as follows

$$\tau = \frac{F}{A} \tag{5.1}$$

where A is the contact area between the SHCC core layer and the inner and outer surfaces.

The average bond stress (τ) and the slip displacement of the specimens POT-A and POT-B are shown in Fig. 5.7. The maximum bond stress (τ_u) of the specimens POT-A and POT-B are 0.073 MPa and 0.218 MPa, respectively.

5.3.5 Numerical model for average bond stress and slip

Based on available test results and a literature review on these bond-slip models, a linear and nonlinear combined bond-slip model is proposed in thesis. The whole

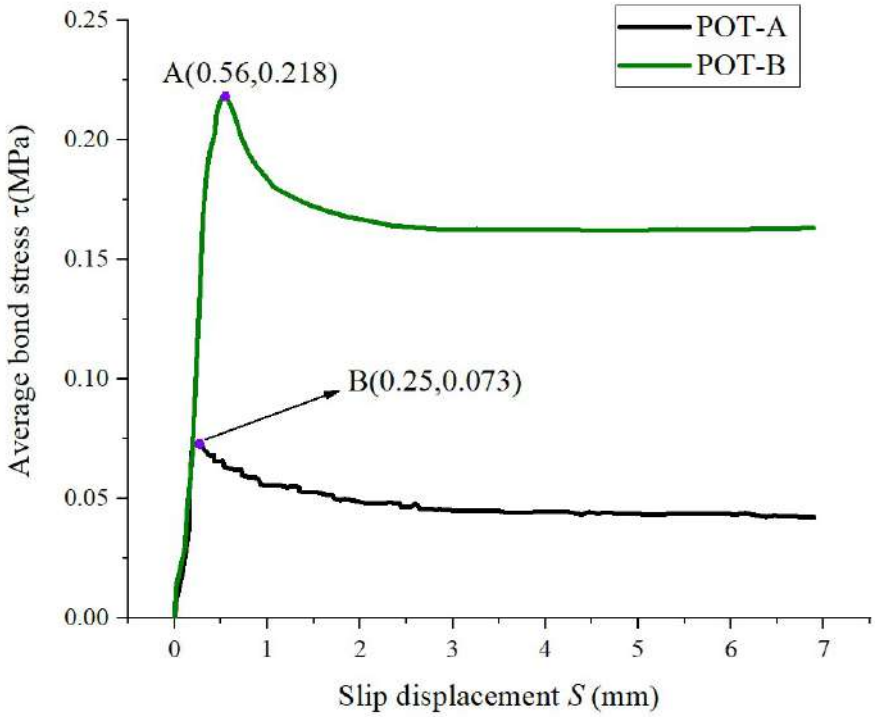

Figure 5.7: Average bond stress versus slip displacement curves

model was divided into three segments: linear increase phase, nonlinear debond phase, and linear friction phase.

For the specimen POT-A, the coordinate values of the turning points B and D are (0.25, 0.073) and (3.20, 0.045), respectively, as shown in Fig. 5.6. Fitting of the numerical model results for the specimen POT-A, with the aid of the software Matlab14.0 , leads to the following equations for the three stages, respectively.

$$\tau = \begin{cases} 0.2989S & for\ S \leq 0.25 \\ 0.0354\exp\left(-S/1.0121\right) + 0.0438 & for\ \ 0.25 < S < 3.20 \\ 0.045 & for\quad S \geq 3.20 \end{cases} \tag{5.2}$$

Similarly, for the POT-B specimen, the coordinate values of the turning points A and C are (0.56, 0.218) and (2.66, 0.165), respectively. The fitting of the numerical results for this specimen leads to the following equations representing the three successive stages, respectively.

$$\tau = \begin{cases} 0.3927s & for\ s \leq 0.56 \\ 0.1926\exp\left(-s/0.021\right) + 0.164 & for 0.56 < s_B < 2.66 \\ 0.1647 & for\quad s_B \geq 2.66 \end{cases} \tag{5.3}$$

The final fitting curves and the experimental results for specimens POT-A and POT-B are shown in Fig. 5.8. Both fitting curves present good agreement with the

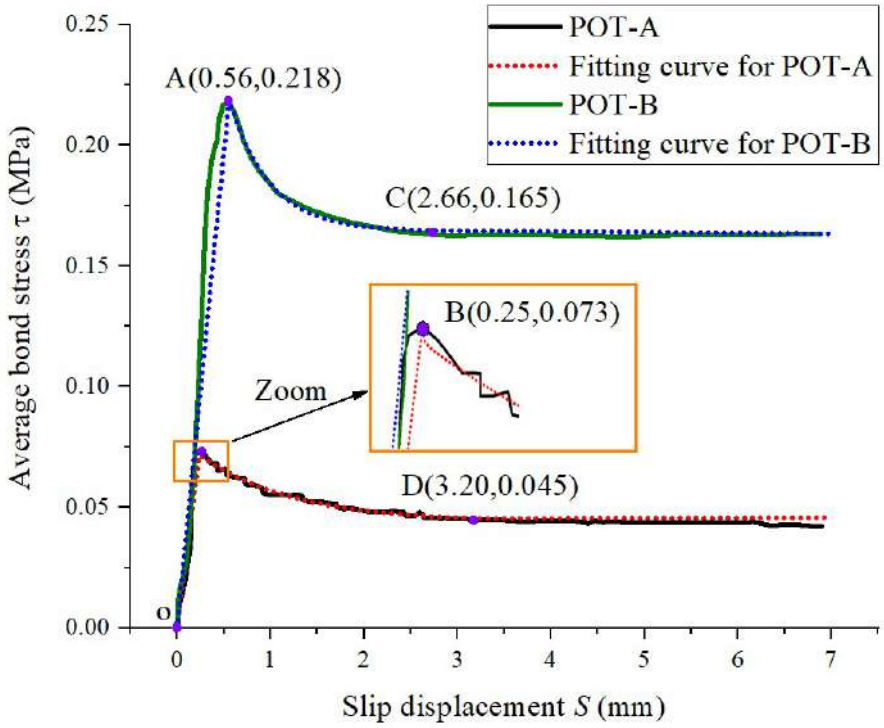

Figure 5.8: Average bond stress versus slip displacement curves

experiments.

5.4 Self-stress measurement test

The expansion of the SHCC core during manufacture hydration is confined by the steel tubes, thus producing self-stress associated with the expansive strain. Therefore, self-stresses in the SHCC core can be calculated by measuring the SHCC core radial expansion after the longitudinal cutting of the outer steel tube.

5.4.1 Specimens for the test

The tested specimens after the push-out test are used for the self-stress measuring tests. As shown in Fig. 5.9, the specimen with the AISI304 tubes is named CFS-A, and the AISI316 tubes named CFS-B.

As shown in Fig. 5.10(a), biaxial strain gages KFG-5-120-D16-11 were used during the tests. The general technical parameters are shown in the Fig. 5.10(b),

The biaxial strain gages were installed on the SHCC core cross-section at four locations spaced by 90 °, as shown in Fig. 5.11. At each location, strain gauges are used to measure the strains in the tangential and radial directions, respectively.

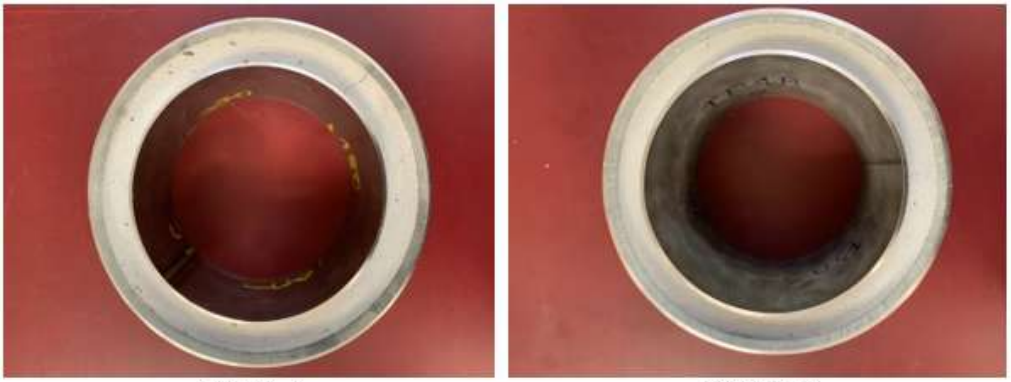

(a) CFS-A (b) CFS-B

Figure 5.9: Specimens for the self-stress measurement tests

(a) Strain gages (b) Technical parameters statement

Figure 5.10: The strain gages and technical parameters statement

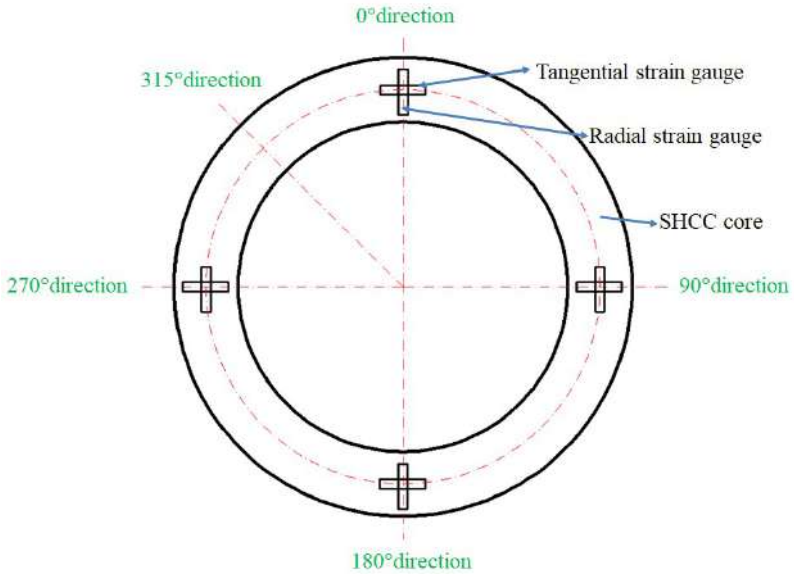

Figure 5.11: Biaxial strain gauge locations on the cross-section of the SHCC core

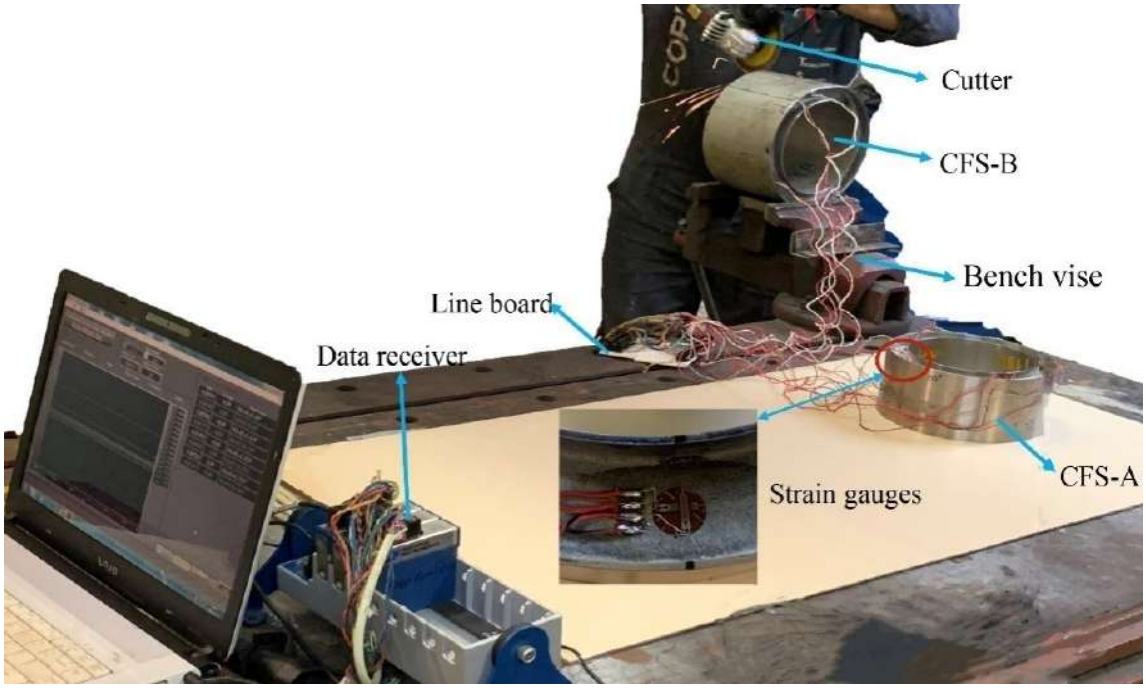

Figure 5.12: Self-stress test setup

5.4.2 Test set-up

As shown in Fig. 5.12, the specimen CFS-B is fixed by a bench vise and the outer pipe cut longitudinally along the 315° generator indicated in Fig. 5.11.

During the cutting, the self-stress in the SHCC core is released, leading to strain relief. The strain gages data acquisition is obtained during the cutting process. The measured data is transferred to the data receiver through lines and shown in the computer screen. The test finishes when the outer pipe is completely cut.

The biaxial strain gages can measure the value of the strain before and after the tests. The strain before the test measured by the stages may not be zero because the operation of stages installation and specimen movement can cause the variety of strain. The difference between the measurement results before and after the test is the accurate strain released by self-stress.

5.4.3 Test results and discussion

After cutting the specimens, the self-stress in the SHCC core layer is released, leading to strain relief. The strain response during the cutting process was acquired from the strain gauges. After cutting, the outer pipes of the specimens are separated from their SHCC core layers, as can be seen in Fig. 5.13, and the surfaces of the SHCC cores are not injured because of cutting.

As shown in Fig. 5.14, when the outer tube was cut the tube opens because of bending stress. Since the bond stresses between layers have already been eliminated

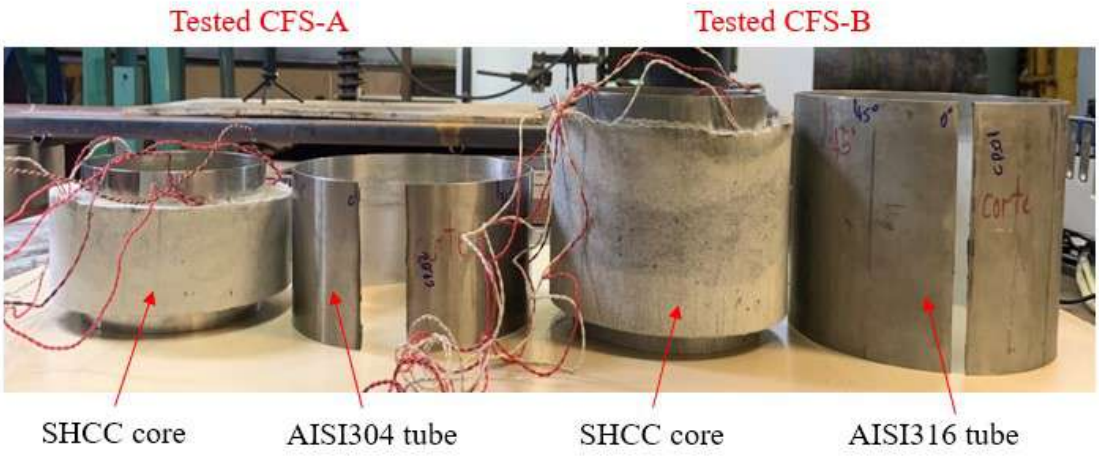

Figure 5.13: Specimens after cutting

by the push-out tests, the measured strain comes from the self-stress relief in the radial direction.

Based on the test results, the strains in the radial direction (ε_r) of the specimens CFS-A and CFS-B are 6.8×10^{-5} and 3.9×10^{-5}, respectively. The tangential strains are too small, and, therefore, are neglected.

Based on the mechanical properties of the SHCC core mentioned in Section 3.2.1, the expansion of the SHCC core layer occurs in the elastic regime. With the Young's modulus (E_0) measured as 20 GPa, the self-stresses (σ_N) in the radial direction can be expressed as

$$\sigma_N = E_0 \varepsilon_r \tag{5.4}$$

The radial self-stresses (σ_N) for the specimens CFS-A and CFS-B are calculated as 0.77 MPa and 1.35 MPa, respectively. The values of self-stresses (σ_N) are employed in the calculation of the friction coefficient between the SHCC core and steel tubes.

5.4.4 Interlayer friction coefficients

As described in Section 5.3.2, in the last stage of the push-out test, the SHCC core slips along the steel tubes. So, the friction coefficient between the SHCC core and the steel tubes is the basic parameter of the interlayer interaction. The friction coefficient can be calculated based on the reported test results.

The stress analysis of the SHCC core during the final friction of the slipping process is shown in Fig. 5.15. The applied load (F) on the top cross-section of the SHCC core, under the friction force (f) resistance acting in the opposite direction, and the half self-stress ($0.5\sigma_N$) acts on both inner (S_{in}) and outer (S_{out}) SHCC

Figure 5.14: The state of CFS-A after cutting

core surfaces. In the last stage of the push-out test, the final slip of the SHCC core behaves as an uniform displacement under an almost constant applied load. So, the applied load (F) is equal to the friction force (f), as follows

$$\mathrm{F} = \tau\left(\mathrm{S_{in}} + \mathrm{S_{out}}\right) = \mathrm{f} = 0.5\mu\sigma_{\mathrm{N}}\left(\mathrm{S_{in}} + \mathrm{S_{out}}\right) \tag{5.5}$$

where μ is the friction coefficient, τ is the average bond stress during the slipping process, with values of 0.045 MPa and 0.165 MPa for the specimens POT-A and POT-B, respectively, and σ_N is the measured self-stress. Solving Eq.5.5 gives a friction coefficient (μ) of 0.117 and 0.244 for specimens CFS-A and CFS-B, respectively.

The different values of the friction coefficient in case of the different tube surface of the CFS-A and CFS-B, where CFS-A with a smooth tube surface and CFS-B with a rough tube surface, is described in Section 2.1. The value of the friction coefficient (μ) will be used in the following coulomb friction model used for numerical simulation.

5.5 Numerical simulation of the push-out test

The finite element model is built to simulate the results of the push-out tests. The whole model consists of three parts: as modelings for SHCC core, steel tubes, and interlayer.

The modified concrete damage plasticity (CDP) model built in Chapter 3 is

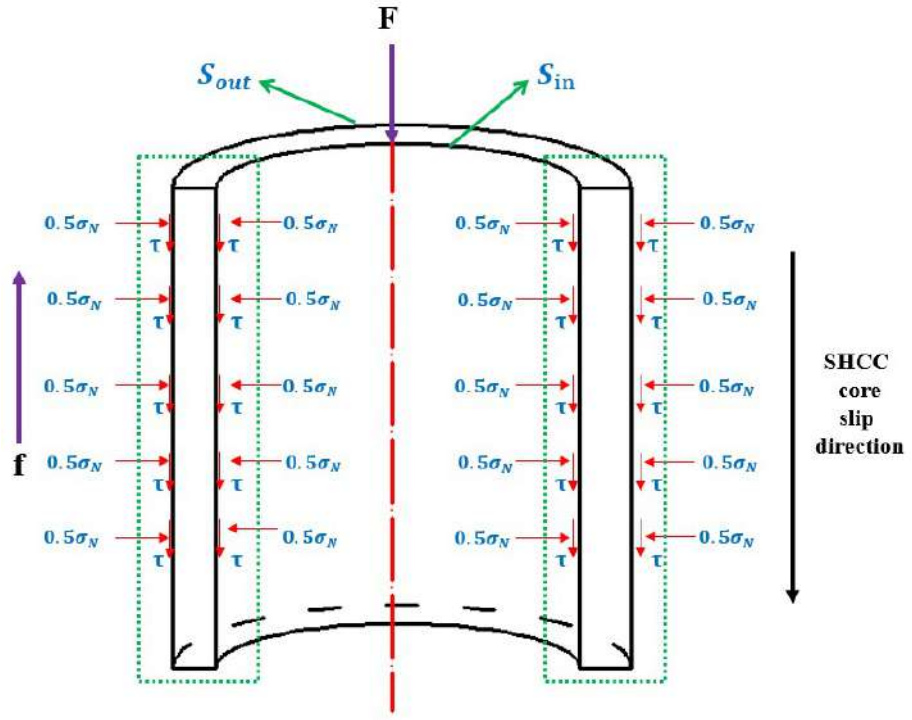

Figure 5.15: Stress analysis of the SHCC core in the final friction process

employed to simulate the property of the SHCC core. Stainless steels 304 and 316 stress-strain curves from Section 5.2.2 are employed in numerical modeling.

5.5.1 Interlayer modeling

To simulate the actual interlayer behavior in ABAQUS, using surface-to-surface contact, where the master surface is defined by the surface of tubes, and the slave surface is defined by the surface of SHCC. So, the property of the contact should be modeling for the simulation.

The contact property in ABAQUS [35] is commonly defined in two directions: normal and tangential to the contacting surfaces. Based on the literature review in Section 2.5, the surface-based cohesive contact behavior in ABAQUS is selected to simulate the bond behavior of the SPs interlayer. So the whole contact property modeling in ABAQUS contains three parts as mechanical tangential behavior, normal behavior, and cohesive behavior. Parameters of each part will be fit based on the former tests results.

As shown in Fig.5.16, the average bond stress versus slip displacement from the tests can be simulated by the combination of cohesive behavior and frictional behavior in the tangential direction.

In ABAQUS simulation, for the POT-B, the bond area (OA phase) and debond area(AC phase) can be simulated by the cohesive behavior, the fraction area (OCE

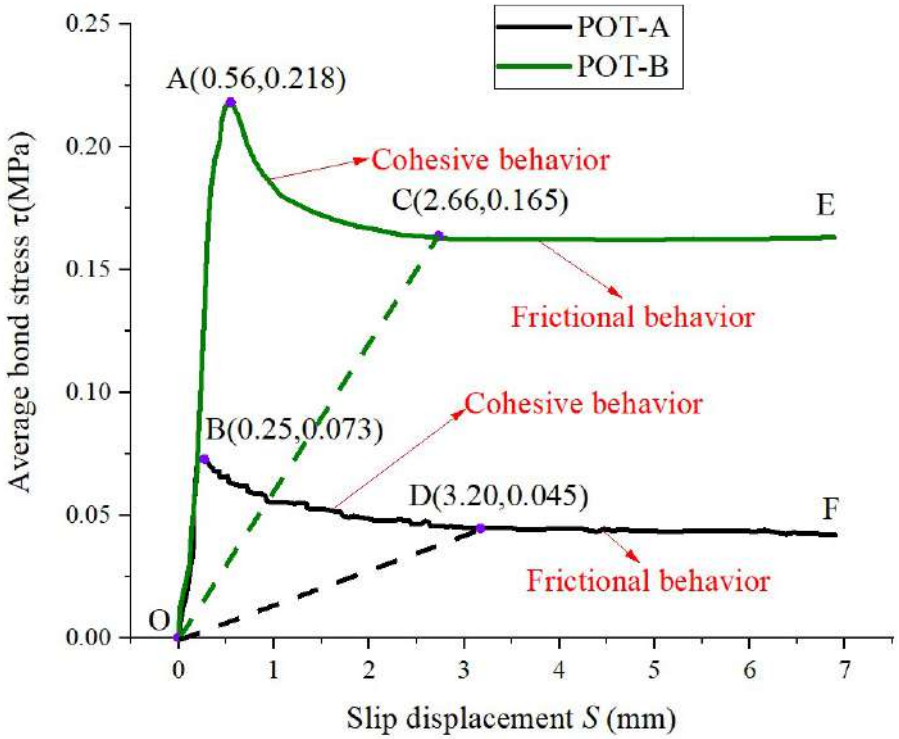

Figure 5.16: Decomposition of the average bond stress versus slip displacement curves

phase) can be simulated by frictional behavior. Similarly, for the POT-A, the bond area (OB phase) and debond area(BD phase) can be simulated by the surface-based cohesive model, the fraction area (ODF phase) can be simulated by the frictional model. Also, the self-stress for the SP can be simulated in the normal direction by the pressure-overclosure model.

The parameters for the interlayer behavior modeling in ABAQUS [35] are summarized in Table 5.2, the details will be shown in the following.

Surface-based cohesive behavior

For the surface-based cohesive contact behavior based on the curves of the average bond stress versus slip in Fig. 5.16, the terms K_{tt} and K_{nn} are calculated as

$$K_{nn} = \frac{\alpha E}{t_p} \tag{5.6}$$

$$K_{tt} = K_{ss} = \frac{\alpha G}{t_p} \tag{5.7}$$

where t_p denotes thickness of the adjacent layer, E represents the Youngs modulus, G represents the shear modulus, and α is a penalty parameter. The relation between E and G is given by

Table 5.2: Parameters for the interlayer behavior

Category	Parameter	POT-A	POT-B
Normal behavior	Contact stress (MPa)	0.775	1.35
Friction model	Friction coefficient	0.117	0.244
	Shear stress (MPa)	0.045	0.165
	Elastic slip (mm)	3.20	2.66
Surface-based cohesive contact behavior	K_{ss}	0.292	0.389
	K_{nn}	0.701	0.934
	Maximum normal stress (MPa)	0.073	0.218
	Plastic displacement (mm)	3.20	2.66
	Exponential parameter	0.5	1

$$G = \frac{E}{2(1+\nu)} \tag{5.8}$$

where $\nu = 0.2$ is the Poisson's ratio of the SHCC core.

Then, considering the penalty stiffness function of the surface-based cohesive contact behavior theory, the coefficients K_{ss} can be written as

$$K_{ss} = \frac{K_{nn}}{2(1+\nu)} \tag{5.9}$$

At the same time, K_{ss} is also given by

$$K_{tt} = K_{ss} = \frac{t_s^0}{\delta_s^0} \tag{5.10}$$

As shown in Fig. 5.16, for POT-A and POT-B along the shear direction, the peak value of contact separation (δ_s^0) is 0.25mm and 0.56mm, the peak values of the contact stress(t_s^0) is 0.073MPa and 0.218MPa, the separation at failure (δ_s^f) is 3.20mm and 2.66mm, respectively. For specimens POT-A and POT-B, K_{ss} was calculated as 0.292 MPa/mm and 0.389MPa/mm, respectively, and K_{nn} as 0.701 MPa/mm and 0.934 MPa/mm, respectively. The values of the maximum normal stress and plastic displacement required by ABAQUS [35] are given by the maximum bond stress (τ_u) and its corresponding slip displacement, respectively, as shown in Fig. 5.16. The exponential softening was chosen for the post damage evolution. The parameter α for the damage variable (D) was obtained from fitting of the experimental data considering the exponential damage variable model, which leads

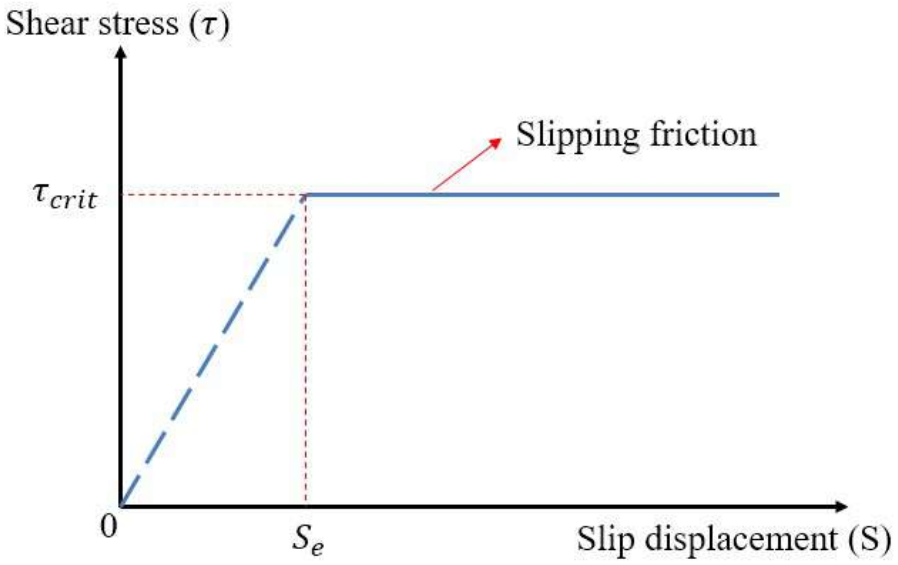

Figure 5.17: Penalty friction formulation behavior in ABAQUS [35]

to values of 0.5 and 1 for POT-A and POT-B specimens.

Tangential behavior

Coulomb friction in ABAQUS is used to simulated the frictional behavior in tangential behavior. It describes the frictional behavior by a coefficient of friction, μ, in all directions (isotropic friction). For ideal friction, no tangential motion between the surfaces will occur unless the traction (shear stress) reaches a critical value(τ_{crit}), due to the normal contact pressure (P) based on the following equation:

$$\tau_{crit} = \mu P \tag{5.11}$$

Because of the difficulty of simulating ideal friction, ABAQUS makes use of a penalty friction formulation in most situations, with a permitted slight relative slip (elastic slip S_e) during surfaces sticking as illustrated via the dashed line in Fig. 5.17.

For the POT-A and POT-B, the critical shear stress(τ_{crit}) is 0.045MPa and 0.165MPa, the elastic slip (S_e) is 3.20mm and 2.66mm, the friction coefficient (μ) is 0.117 and 0.244 as described in Section 5.4.4, respectively.

Normal behavior

The normal behavior is described by the pressure-overclosure contact model, as shown in Fig. 5.18. The model minimizes the penetration of the master surface by slave nodes. This constraint induces pressure when the surfaces are in contact and

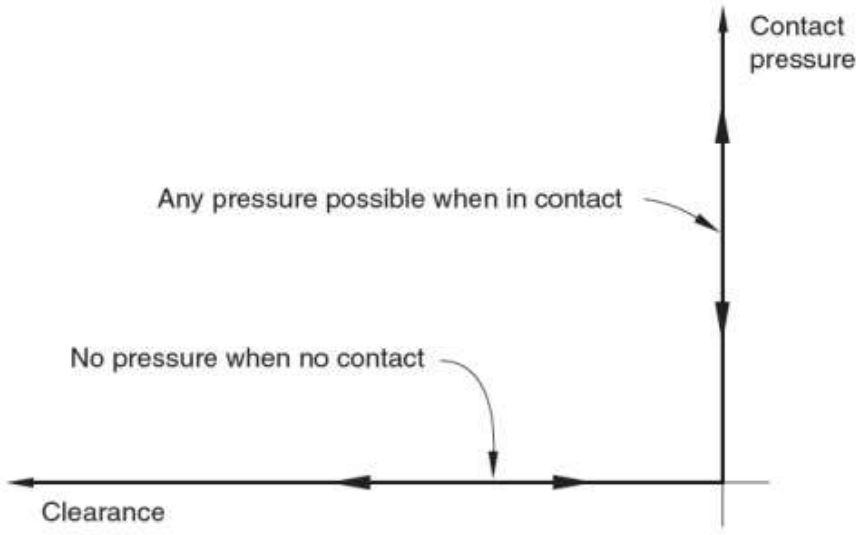

Figure 5.18: Pressure-overclosure model in ABAQUS [35]

sets the pressure to zero when the surfaces separate.

The contact pressure P is a function of the overclosure distance h, which is the penetration distance during the iterations before equilibrium in the increment is achieved. The basic model is described by the two conditions below:

$$\begin{cases} P = 0 & for\ h < 0 \quad (open) \\ P > 0 & for\ h = 0\ (closed) \end{cases} \tag{5.12}$$

The defined contact pressure P of the POT-A and POT-B is matched with the self-stress measured in Section 5.4 as 0.775MPa and 1.35MPa, respectively.

5.5.2 Simulation results

The finite element (FE) model for POT-A is built to simulate the push-out behavior as shown in Fig. 5.19. For the boundary condition, the top face of the SHCC core is coupling with the reference point RP-1, where the displacement is applied. The bottom of the tubes is coupling with the reference point RP-2, which is fixed during the push-out simulation.

For the material properties, the SHCC core is modeled as described in Section 5.5.1, and the steel tube is modeled as described in Section 5.5.2.

For the interaction, the surface-to-surface contact is chosen for the simulation, where the master surface is defined by the surface of tubes, and the slave surface is defined by the surface of SHCC. Small sliding is selected for the sliding formulation. The property of the contact is defined as described in Section 5.5.3, the coefficients of the contact property are summarized in Table 5.2.

The C3D8R element is used for the whole model, and a standard mesh-sensitivity

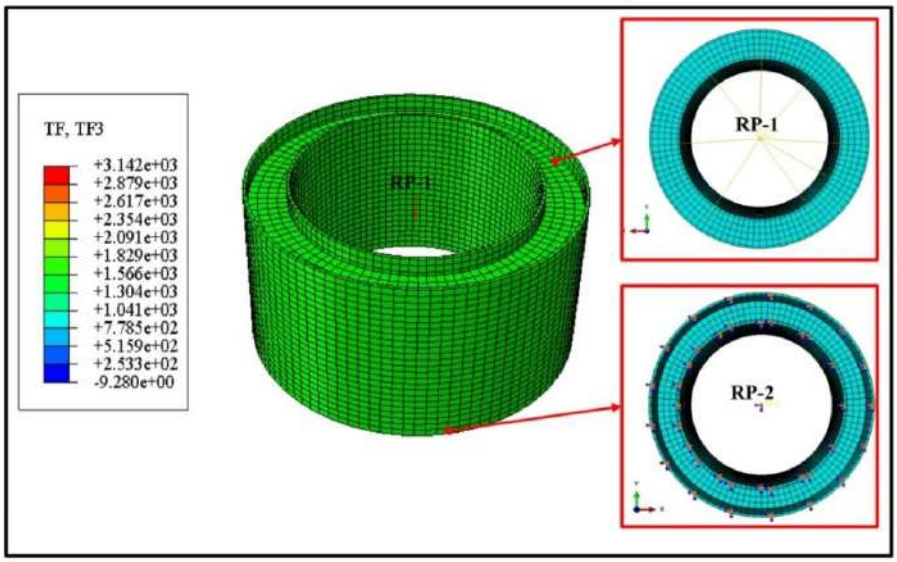

Figure 5.19: Finite element analysis of POT-A pull-out test

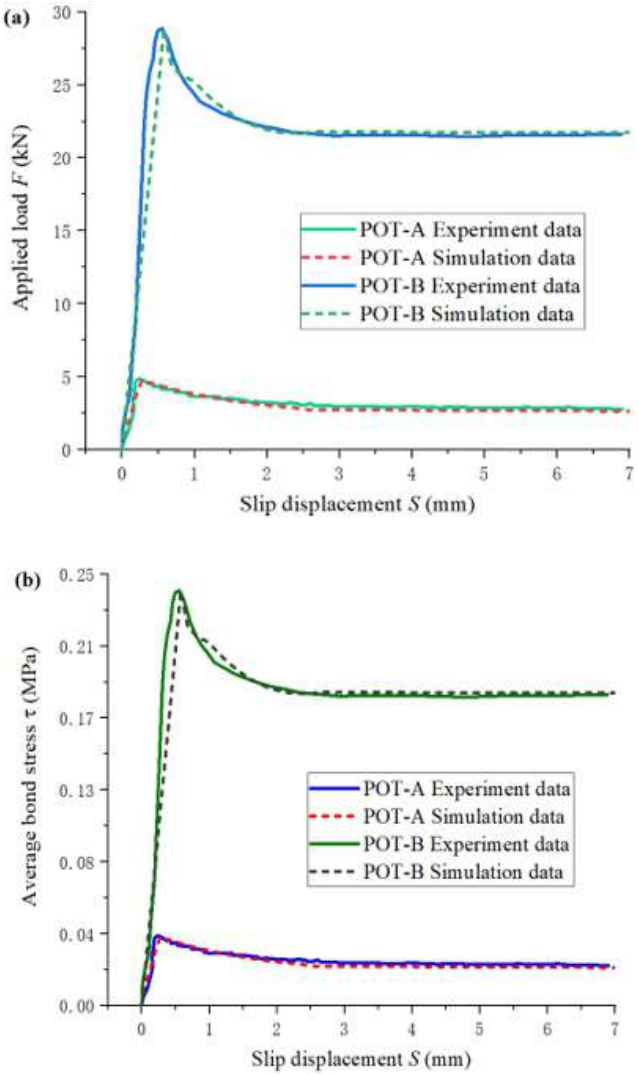

Figure 5.20: Results of simulations and experiments: (a) applied load versus slip displacement and (b) average bond stress versus slip displacement.

analysis is performed. Finally, 100 elements in every circumferential direction, 1 element for each tube layer, and 3 elements for the SHCC layer are applied.

The finite element (FE) model for POT-A and POT-B were built to simulate the push-out behavior. Fig. 5.20 shows the comparison between the results obtained from the simulations and experiments given by the applied load and average bond stress versus the slip displacement. The numerical results show that both the ultimate force, ultimate bond stress and the ultimate slip displacement agree well with the experimental results. Hence, it can be considered that the FE model is suitable to predict the interlayer behavior of the SPs during push-out tests.

5.6 Summary

In this chapter, the interlayer behavior of the SPs was studied by the push-out test. The self-stress in the SPs was measured from the experiments.

The actual interlayer behavior was modeled in three parts as the surface-based cohesive model for the bond-debond behavior, the Coulomb friction model for the frictional behavior in the tangential direction, the pressure-overclosure contact model in the normal direction.

Based on the test results and numerical analysis, the following conclusions are drawn.

- The relationship of the average bond stress (τ) and the slip displacement of the SPA and SPB specimens were measured. The maximum bond stress (τ_u) were 0.073 MPa and 0.218 MPa, respectively.

- Expressions were proposed for the interlayer behavior associated, based on the numerical results from the two specimens SPA and SPB, respectively.

- The values of self-stresses (σ_N) for the SPA and SPB specimens experimentally obtained were, respectively, 0.77 MPa and 1.35 MPa.

- The obtained interlayer friction coefficients based on the experimental push-out tests were 0.117 and 0.244 for SPA and SPB specimens, respectively.

- The correlation between experimental and numerical results for push-out test showed very good agreement. The actual interlayer behavior can be modeled in three parts as the surface-based cohesive model for the bond-debond behavior, the Coulomb friction model for the frictional behavior in the tangential direction, the pressure-overclosure contact model in the normal direction.

Chapter 6

Verify tests for the mechanical model of SPs

6.1 Introduction

According to the previous research, each part of the mechanical model of SPs has been built. In this chapter, the verification tests have performed. The correlation between the results from experiments and numerical simulations were studied.

High hydrostatic pressure and bending are the primary loading conditions for the SPs during installation and service life. During the service life in ultra-deep-water scenarios (beyond 1,500 m), the high hydrostatic pressure may cause the pipe collapse[15]. The free spanning caused by the water scouring and topography can make the pipe subject to bending load [13]. During all the subsea pipeline installation methods, extreme bending could be applied, especially the reeling method.

To verify the model and study the behavior of the SPs when subjected to these loads, the collapse experiments and the bending experiments to simulate reeling installation were performed.

6.2 Mechanical model of SPs

To sum up, the whole mechanical model for the SPs consists of three parts as modelings for SHCC core, steel tubes, and interlayer. The experimental research on each part has been done in the former chapters and the corresponding numerical models were also built.

The summary of the modeling is shown as follows.

6.2.1 SHCC core modeling

The property of the SHCC core has been studied in Chapter 3 through uniaxial tensile and compressive experiments, biaxial experiments, and triaxial experiments.

Then, the modified concrete damage plasticity (CDP) model was built based on these experiments results, and the classic continuous damage theory. The modified CDP model was verified and can be used to simulate the behavior of SHCC alone or used as a core material in SPs. The parameters of the modified CDP model used in ABAQUS are summarized in Section 4.2.

6.2.2 Steel tube modeling

Currently, the stainless steels 304 and 316 are used for the SPs. The material properties of these two kinds of steels were studied by standard experiments. The stress-strain curves were employed in numerical modeling. The values of yield stress and elastic modulus were obtained from the tests reported in Section 5.2.2.

6.2.3 Interlayer modeling

The actual interlayer behavior was researched by the push-out test and self-stress measure test. The corresponding numerical model used in ABAQUS was built in Section 5.5.1. The parameters of the interlayer modeling used in ABAQUS are summarized in Section 5.5.1.

6.3 Collapse verify test

The collapse experiments on the two kinds of SPs were performed. The operation steps have been described in Section 4.4.1. The collapse pressure (P_co) obtained from the experiments was correlated with the simulation results from the numerical analysis.

6.3.1 Full-scale test

The details of the experiments have been described in Section 4.4.1. Here, more specimens were performed, four SPs with stainless steels 304, named as SP-A, and two SPs with stainless steels 316, named as SP-B, were operated in the test.

Table 6.1 presents the geometries of the SPs used in the tests, with prototype length (L), outside diameter of the outer pipe (D_1), inside diameter of inner pipe(d_2), core thickness (T), steel layer thickness (t), and the initial ovality of the outer pipe (Δ_0).

Table 6.2 lists the collapse pressures of all the tested SP specimens. The experimental collapse pressures of SP-1A, SP-2A, SP-3A, SP-4A, SP-1B, and SP-2B are 37.68MPa, 37.18MPa, 36.92MPa, 35.23MPa, 38.71MPa, and 34.29MPa. Comparing with the corresponding initial ovality of the outer pipe (Δ_0), it is found that the collapse pressures decrease with the increase of the initial ovality for the same type of sandwich pipe.

Table 6.1: Geometrical parameters for sandwich pipes

SP type	Steel type	L (mm)	D_1 (mm)	d_2 (mm)	T(mm)	t(mm)	Δ_0 (%)
SP-1A	SS304	1250	203.20	148.40	23.40	2.00	0.29
SP-2A	SS304	2600	203.20	148.40	23.40	2.00	0.34
SP-3A	SS304	2600	203.20	148.40	23.40	2.00	0.46
SP-4A	SS304	3370	203.20	148.40	23.40	2.00	0.57
SP-1B	SS316	3125	219.08	162.74	22.63	2.77	0.19
SP-2B	SS316	3000	219.08	162.74	22.63	2.77	0.50

Table 6.2: Collapse pressures of sandwich pipes from tests

SP type	Collapse pressure P_{co} (MPa)	SP type	Collapse pressure P_{co} (MPa)
SP-1A	37.68	SP-4A	35.23
SP-2A	37.18	SP-1B	38.71
SP-3A	36.92	SP-2B	34.29

6.3.2 Numerical simulation

The 2D ring finite element (FE) model was built to simulate the collapse behavior of the SP. The model in ABAQUS was implemented as described in Section 6.2. Also, the fully bonded and unbonded layer conditions were studied, the setting was implemented as described in Section 4.2.2.

For the boundary condition, to fix the position of the model during simulation, as shown in Fig. 6.1, two vertices (A and B points) can only move along the Y-axis; with another two vertices (C and D points) only move along the X-axis.

The CPE8 element type was used for the whole model. The ultimate structural strength of a sandwich pipe subjected to external pressure was investigated by employing the Riks method (arc length method). External pressure was applied to the

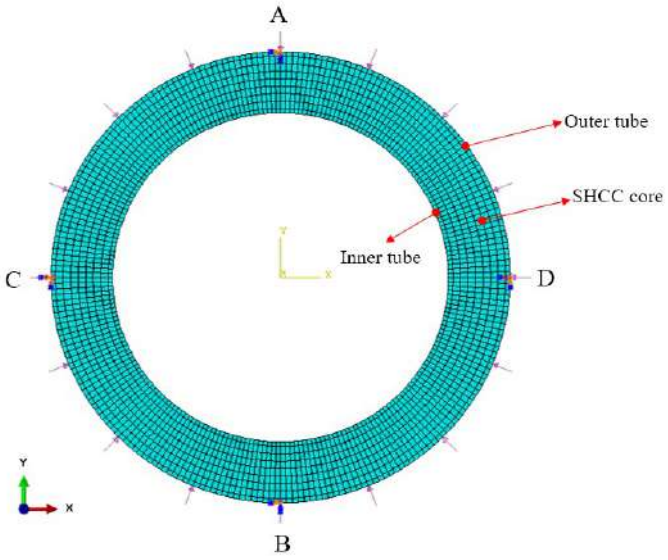

Figure 6.1: The FE modeling of the collapse simulation

outer pipe through the surface load, as shown in Fig. 6.1. The setting of the maximum pressure increment significantly affects the simulation results. A large pressure increment can lead to inaccurate collapse pressure while a small pressure increment might result in, for models with high structural stiffness, a displacement near to zero which causes convergence problems. The numerical settings were carefully adjusted to avoid these two problems.

6.3.3 Results and discussion

Fig. 6.2 shows the von Mises stress of SP-1A during the collapse process. During loading, the outer tube was yield at first, as shown in Fig. 6.2(a), then the inner tube yield, as shown in Fig. 6.2(b), subsequently, the structure loses stability and collapsed. The SHCC core was mainly damaged by compressive stress, where the main damage areas were focused on the four vertex areas near the outer and inner tubes, as shown in Fig. 6.2(c).

Table 6.3 listed the numerical results of the collapse pressures for sandwich pipes under the interlayer modeling, fully bounded, and unbonded situations.

Fig. 6.3 compares the numerical and experimental results. For all prototypes, the measured collapse pressures remained between the results given by the fully bonded FE model and frictionless FE model, which agrees with the fact that the actual sandwich pipe with SHCC core had a partially bonded interface condition. The experimental collapse pressure of the prototype SP- 2B was detected as a probable error, case the value was near to the value on the unbonded situation, the interlayer modeling simulation result was considered more able to reflect the actual value. For

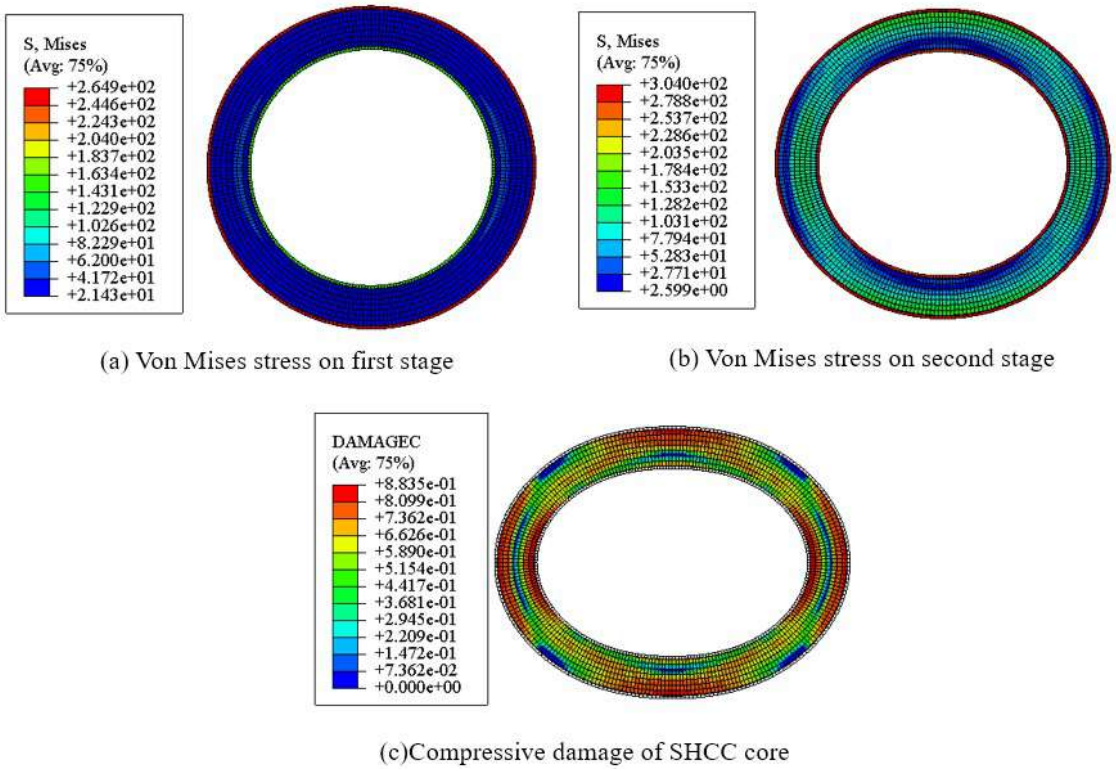

(a) Von Mises stress on first stage

(b) Von Mises stress on second stage

(c)Compressive damage of SHCC core

Figure 6.2: Von Mises stress of SP-1A and compressive damage of SHCC core

Table 6.3: Numerical results of collapse pressures of sandwich pipes

SP type	Collapse pressure(MPa) (under interlayer model)	Collapse pressure(MPa) (fully bounded)	Collapse pressure(MPa) (unbonded)
SP-1A	37.86	39.99	34.10
SP-2A	36.68	39.40	33.71
SP-3A	36.42	38.09	32.88
SP-4A	35.31	36.82	32.14
SP-1B	38.07	42.75	33.65
SP-2B	36.40	40.41	32.64

the other prototypes, the simulation results match the experimental data well. The deviation of the SP-1A, SP-2A, SP-3A, SP-4A, and SP-1B are 0.48 % , 1.34 % , 1.35%, 0.23%,and 1.65%, respectively. The average deviations are 1.01 %. Both the simulation results under the fully bounded and unbonded conditions have a very large error, the average error is 6.04 % and 10.32%, respectively.

The good agreement between the numerical simulation results under the interlayer modeling and the experimental data shows that the FE model is capable of providing accurate results for the collapse simulation.

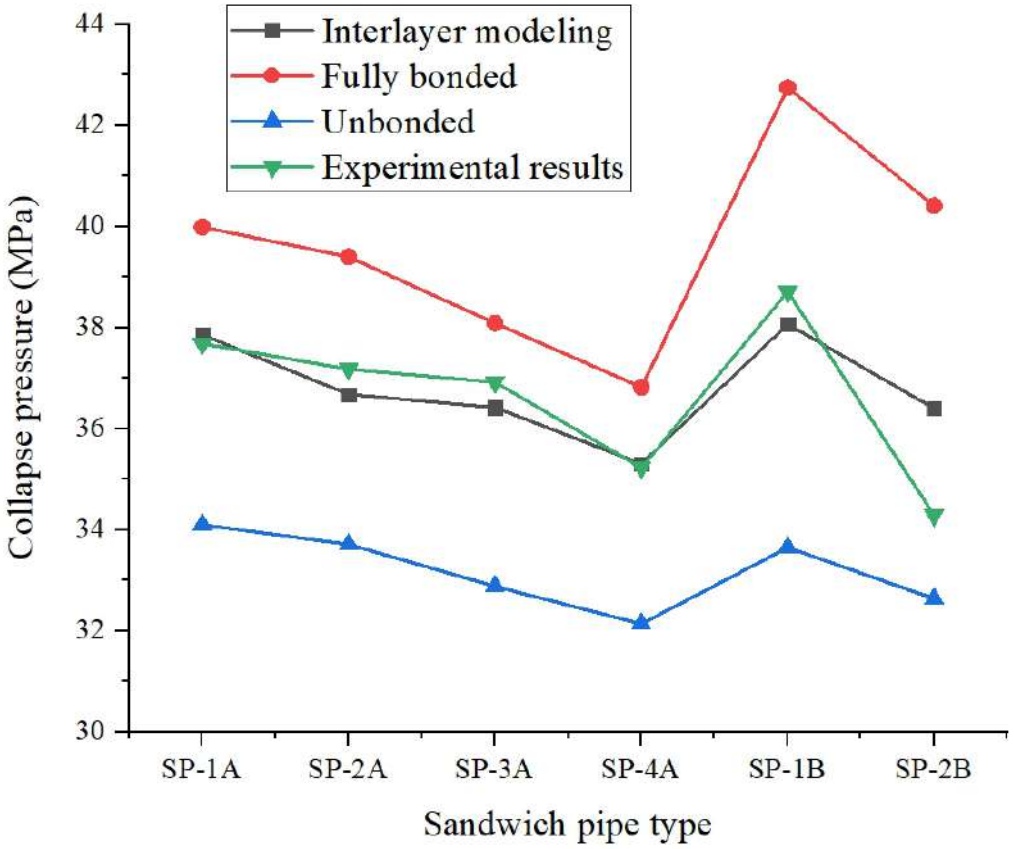

Figure 6.3: Comparison between numerical and experimental results for SPs

6.4 SP bending correlation tests

To verify the correlation between the results from experiments and numerical simulations, the SP bending tests were performed.

6.4.1 Full-scale test setup

The geometry of the outer tubes of the SP specimens were mapped before the bending tests. The middle cross-section and four longitudinal lines on each SP outer surface were mapped, as indicated in Fig. 6.4(a). The mapping method consists of first creating reference lines on the tube surface, guiding the measurements of the radial deflections by the laser tracker. Each tube was positioned horizontally and fixed to supports using magnets so that the tube does not move when being mapped, assuring that the initial coordinates, taken as references, do not change during measurements by the instrument. The outer tubes were then divided into four quadrants as shown in Fig. 6.4(a), where the weld bead was considered the 0° line. The marked longitudinal lines spaced by 90° and the middle cross-sections of the SP specimens are shown in Fig. 6.4(b-c).

The experimental setup for the SP bending test is shown in Fig. 6.5. The

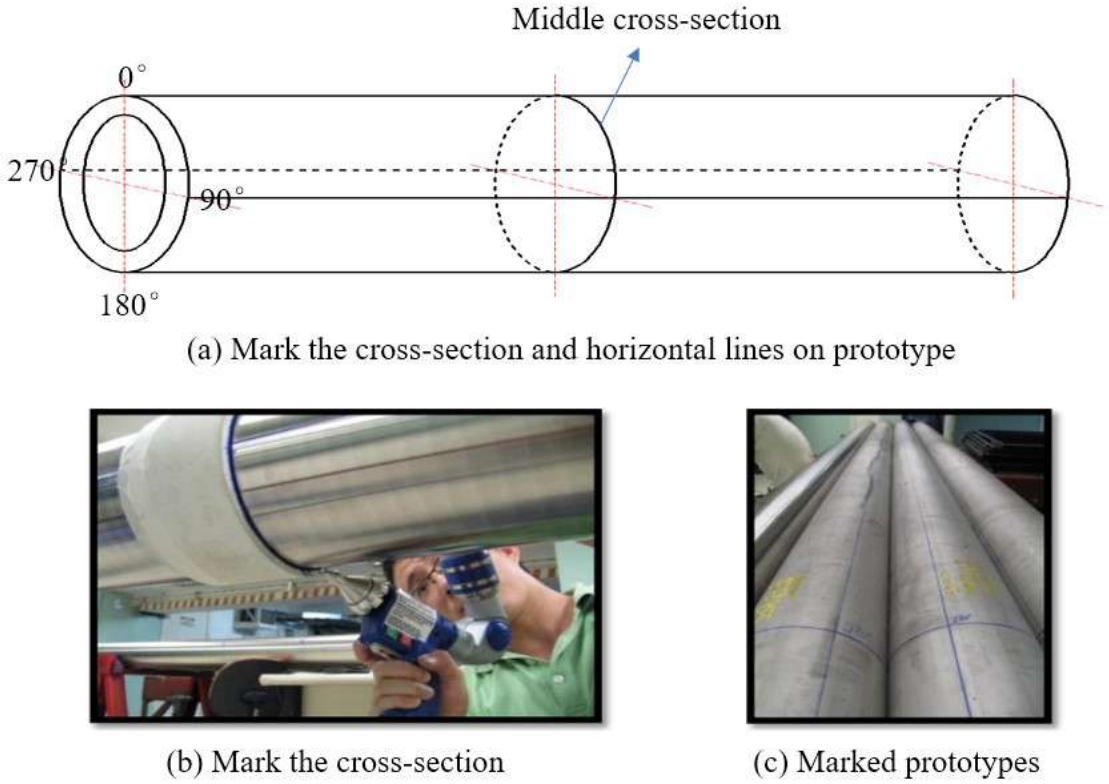

Figure 6.4: Mapping on the surface of the prototypes

bending apparatus was designed to induce plastic deformations in pipe specimens with the displacement of rigid surfaces, simulating the pipeline installation condition by the reel-lay process. The main characteristics of the bending apparatus consider: (1) specimen maximum length of 6 m, (2) specimen maximum external diameter of 324 mm (12.75 in.), (3) die tools maximum driving force of 800 kN (1.8E+5 lbf), (4) curvature radius of one of the rigid surfaces (reel diameter) of 8 m (26 ft.), and (5) curvature radius of the rectification surface of 40 m (130 ft.).

The two SP specimens described in section 5.2.1 were submitted to the bending test, the specimen with AISI304 steel tubes was named as SPA, while the that with AISI316 steel tubes was named as SPB. Both specimens are 6 m in length.

As shown in Fig. 6.5, the blocks of curving and rectification rigid surfaces are connected by rods, able to slide on each other. The SP specimen is placed between these two blocks, with both ends installed at pivotal connections fixed on the setup base. The rods are linked to two electro-hydraulic pistons, which are driven by a hydraulic pump with a speed of 2.5 mm/min during the test. The strain gauges are installed on the surface of the outer pipe at the positions of the SP middle cross-section and along the longitudinal lines at 0° and 180° , as indicated in Fig.12. Three strain gages were installed on the 0° line at the intersection with the pipe mid-section in the longitudinal direction (SG-1, SG-2, and SG-3) e other three longitudinal strain

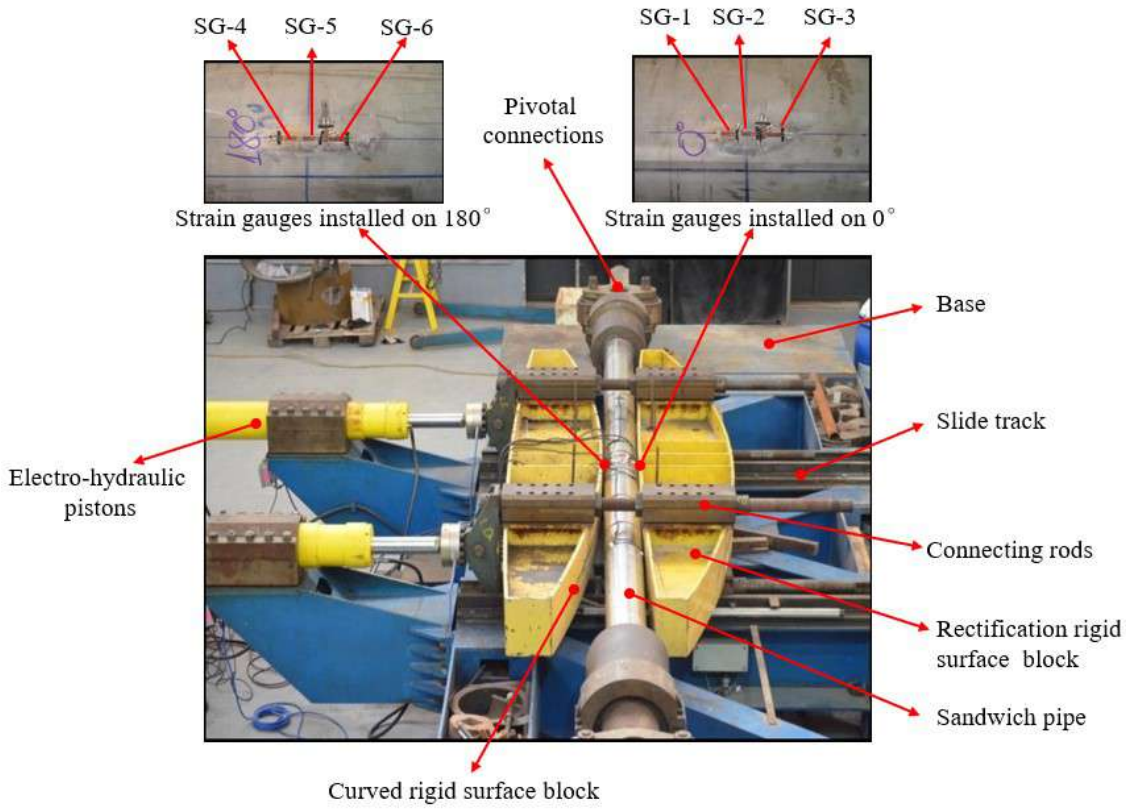

Figure 6.5: Bending apparatus setup

gages installed on the 180° line also at intersection with the mid-section (SG-4, SG-5, and SG-6). One strain gauge was installed along the circumferential direction at the intersection of the 0° line with the mid-section. The results from this strain gage used to control the pipe circumferential local bending are not reported in the correlation study. The use of three longitudinal strain gages at practically the same location guarantees redundancy to the obtained data signals. One LVDT was used to monitor the motion of one block in relation to the other. The signal from the strain-gauges and LVDT were recorded using data acquisition with the aid of the software Labview.

6.4.2 Numerical simulation

A finite element (FE) model was built to simulate the behavior of the SP specimens during the bending tests, which intends to reproduce the pipeline installation conditions by the reel-lay method. As shown in Fig. 6.6(a), the curved block is set as the rigid body to accommodate the pipe curvature as on the reel surface. In the numerical simulation, both pipe ends are coupled with reference points. The SP FE model was implemented as described in section 6.2.

For the boundary conditions, both SP ends are simply supported and can only

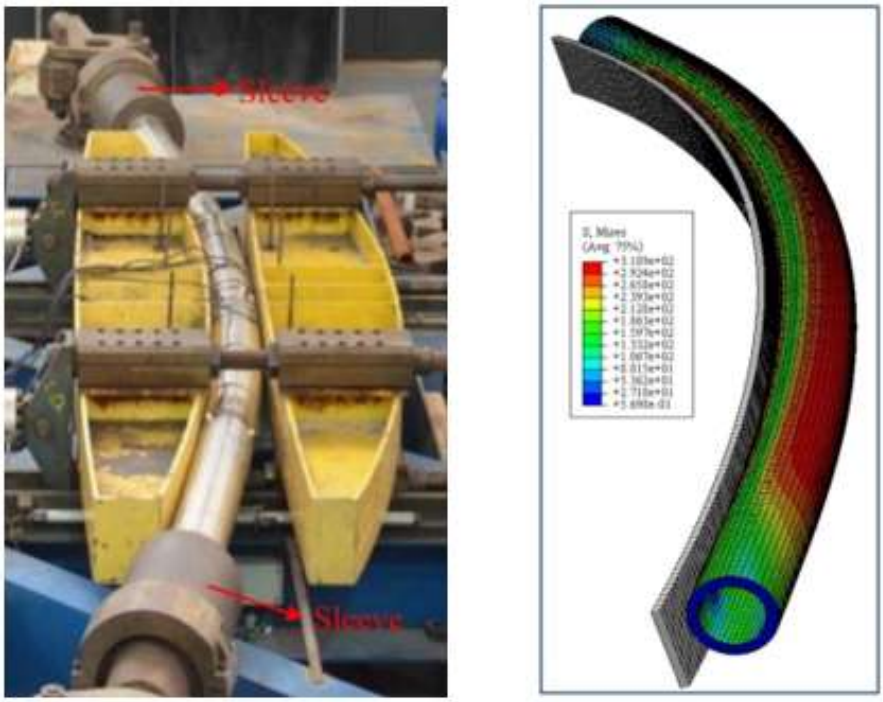

Figure 6.6: Bending test and numerical simulation for the SPA specimen

rotate on the bending plane. The rotation is applied on the bending block around the pipe transverse direction, while the other degrees of freedom are constrained. The element type C3D8R, a three-dimensional solid element with 8 nodes and reduced integration, was used to model the SP specimens. A mesh-sensitivity analysis was performed to analyze the effect of the mesh refinement on the strain and stress results implementing the final mesh sizing.

The stress distribution for the bent SPA obtained in the numerical simulation is shown in Fig. 6.6(b). The stress values increase from the middle section to the ends along the longitudinal direction during the bending process, with the maximum stress appearing on the SP outer pipe in the middle section region. The tubes of the SPs also yield from the middle section to the ends along the longitudinal direction during the bending process, the SHCC core was destroyed, the interlayer relationship debonded by the shear stress, visable deformation could be seen in the middle section region.

6.4.3 Correlation between experimental tests and numerical simulations

Strains obtained in the longitudinal direction at the mid-section from the experimental tests and numerical simulations are shown in Fig. 6.7 for SP specimens

SPA and SPB, respectively. The strains increase during the bending process until a maximum value is attained.

The maximum strain values numerically obtained for the SPA specimen presents very good agreement with the test results at both 0° and 180° locations at the mid-section, during the increasing bending curvature, as shown in Fig. 6.7(a).

For the SPB specimen, the simulation results have a better agreement with the test results during the initial stage associated with the increasing bending curvature, but they tend to a lower bound value in the final stage of the simulation, as shown in Fig. 6.7 (b).

In general, the numerical results approach quite well the experiments, consequently FE model of the SP using the actual interlayer friction behavior can be employed in simulations considering the SP bending behavior.

6.5 Parametric study of SP ultimate and post-failure bending

Based on the developed FE element model, a parametric study was conducted to describe the SP behavior up to and beyond the ultimate bending capacity. The influence of the SP geometry and interlayer bond behavior was evaluated in this study. For the interlayer behavior, fully bonded and unbonded conditions were compared with the actual interlayer behavior to demonstrate the influence of the bond characteristics on the bending capacity. The SP geometry was evaluated, considering the influence of the length to diameter ratio, diameter to thickness ratio, and the outer pipe ovality generated during the steel tube manufacturing process.

Fig. 6.8 shows the geometry of the SP cross-section employed in the parametric study, where the external diameter and thickness of the outer and inner steel pipes are D_1 , T_1, D_2 , and T_2 , respectively. The external diameter and thickness of the SHCC core layer are identified as D_3 and T_3 .

6.5.1 SP ultimate bending

The FE model was employed to study the SP bending capacity. Both SP ends were coupled to the corresponding reference points to which rotations were prescribed on the bending plane to simulate the loading condition applied in the tests.

Fig. 6.9 shows that the increase of the L/D ratio of the SP specimen causes little influence on ultimate bending moment. After the point of $L/D = 9$, the curve are almost plateau, indicating the stability of the ultimate bending moment. Based on these results, the parametric study was performed for $L/D = 9$.

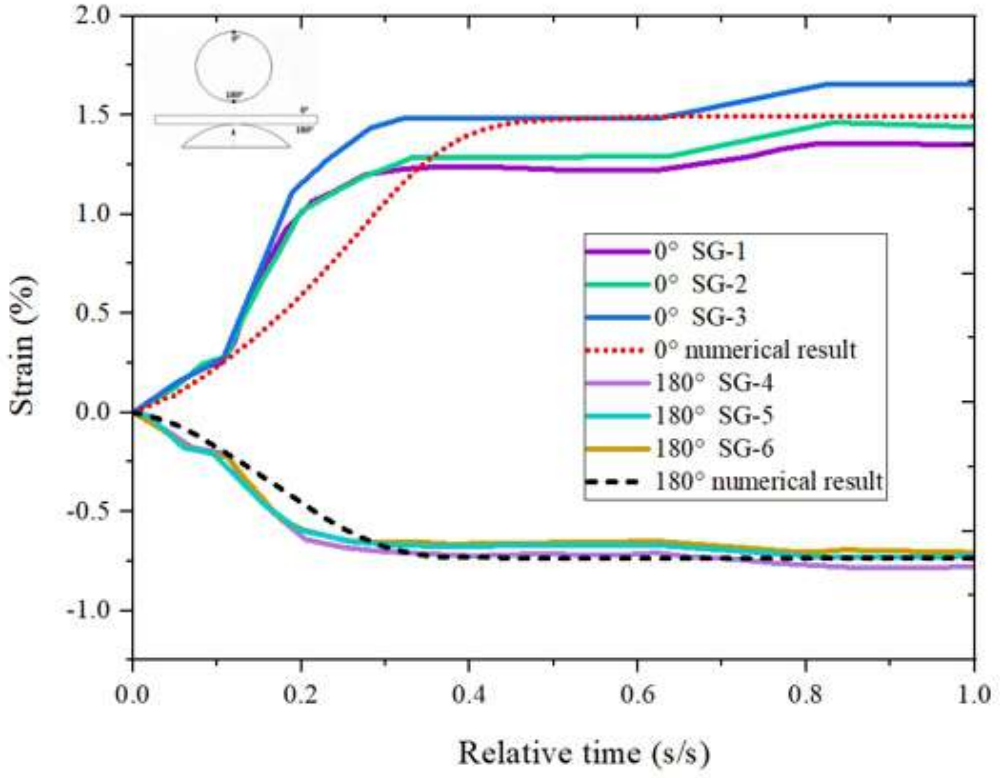

(a) Specimen SPA

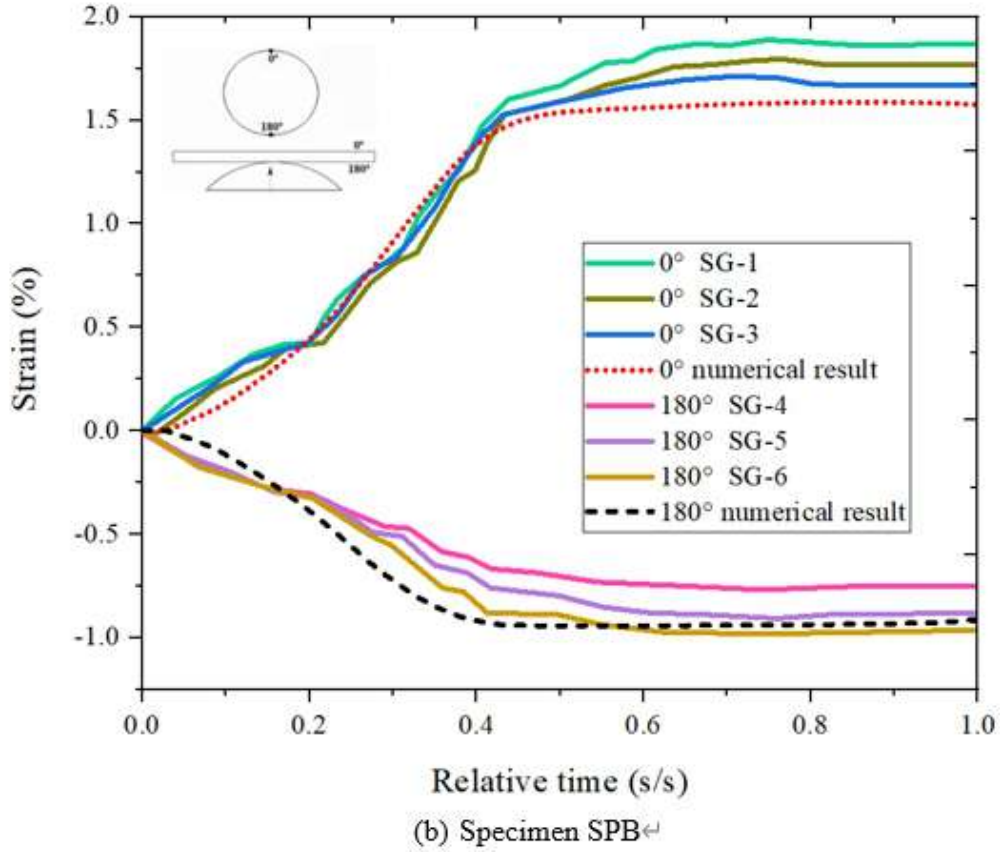

(b) Specimen SPB

Figure 6.7: Correlation between experimental and numerical results

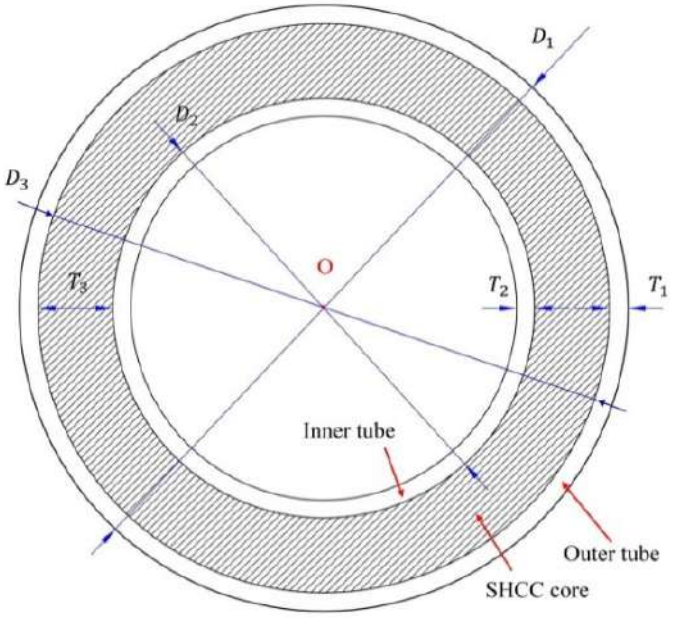

Figure 6.8: Geometry of SP cross-section

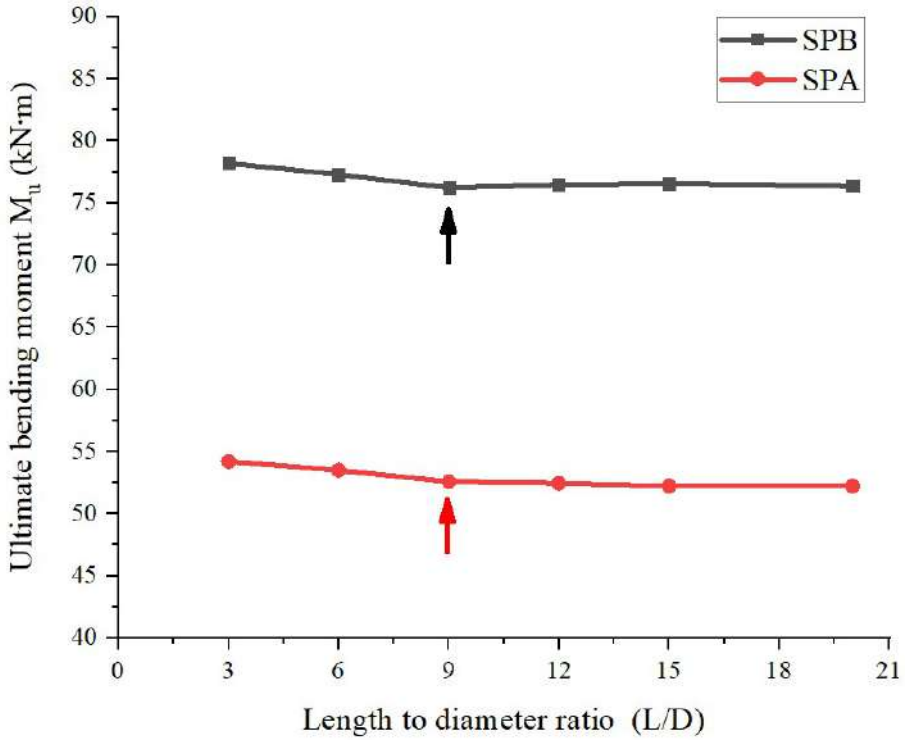

Figure 6.9: Influence of the length to diameter ratio (L/D)

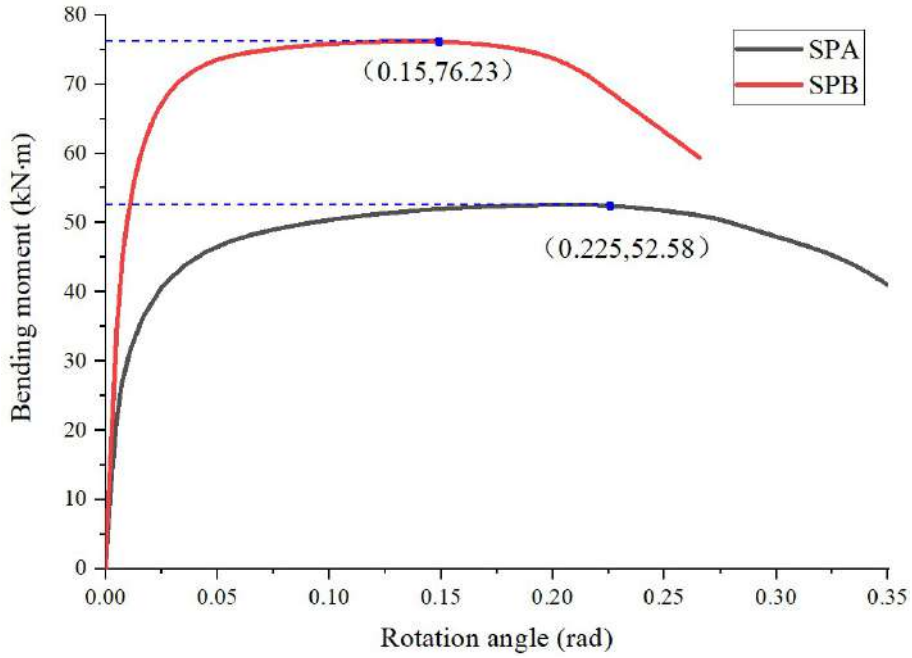

Figure 6.10: SP bending behavior during the tests

Fig. 6.10 presents the bending moment behavior during the tests for both SP specimens SPA and SPB. The ultimate bending moments are 52.58 kN.m and 76.23 kN.m for the SPA and SPB specimens, respectively. The whole bending process can be described as an increasing phase, followed by a stable phase, and, finally, a failure phase (ultimate bending strength and unloading). The span of the stable phase for SPA is larger than that for SPB.

6.5.2 Influence of interlayer bond condition on SP bending behavior

Fig. 6.11 shows the influence of interlayer bond conditions on the SP bending behavior. Both the SP specimens have the same tendency under the fully bonded condition; the bending moment and the range of the plastic stable phase are visibly wider than those for the unbounded condition. The ultimate bending moments under a fully bonded condition are 55.01 kNm and 84.42 kNm for the SPA and SPB specimens, which are 4.6% and 10.7% larger than the experimental results, respectively.

The ultimate bending moments for the unbounded and the actual interlayer behavior conditions are approximately the same in case the interlayer friction coefficients calculated in the section 2.5.3 is small. The actual interlayer bonding are destroyed during bending. The actual friction has little effect on the ultimate bending moments. However, the range of the plastic stable phase for the actual condition

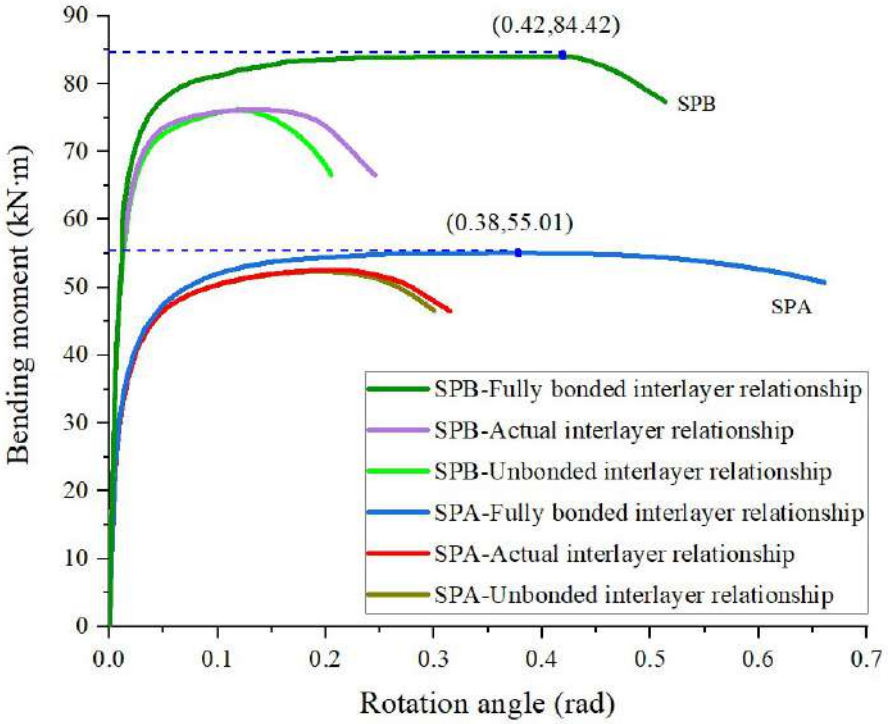

Figure 6.11: Influence of the interlayer bond conditions on the SP bending behavior

is wider than that for the unbounded condition. This is more remarkable for the specimen SPB when compared to SPA, because the interlayer bonded stresses of SPB were higher than those of SPA, as reported in Section 5.4.

6.5.3 Influence of steel tube thickness on ultimate bending moment

The thicknesses of the inner and outer steel pipes have shown considerable influence on the ultimate bending moment. The SPB specimen was used in a parametric study to evaluate this influence. Initially, the analyses were performed considering fixed the thicknesses of the inner steel pipes and SHCC core layer , while the outer pipe thickness was varied. Additionally, the thicknesses of the outer steel pipe and SHCC core layer were then fixed, while varying the inner pipe thickness. Increasing the thickness from 2.0 mm to 4.8 mm, with increments of 0.7 mm, and, consequently decreasing the D/t ratio, increases the ultimate bending moment, as expected (Fig. 6.12).

Fig. 6.12 shows that with the increase of the tube thickness (T), the ultimate bending moment (M_U) of the SPB specimen increases linearly. The fitting expressions for the outer and inner pipes are, respectively:

$$M_U = 35.27 + 14.86\mathrm{T}_1 \tag{6.1}$$

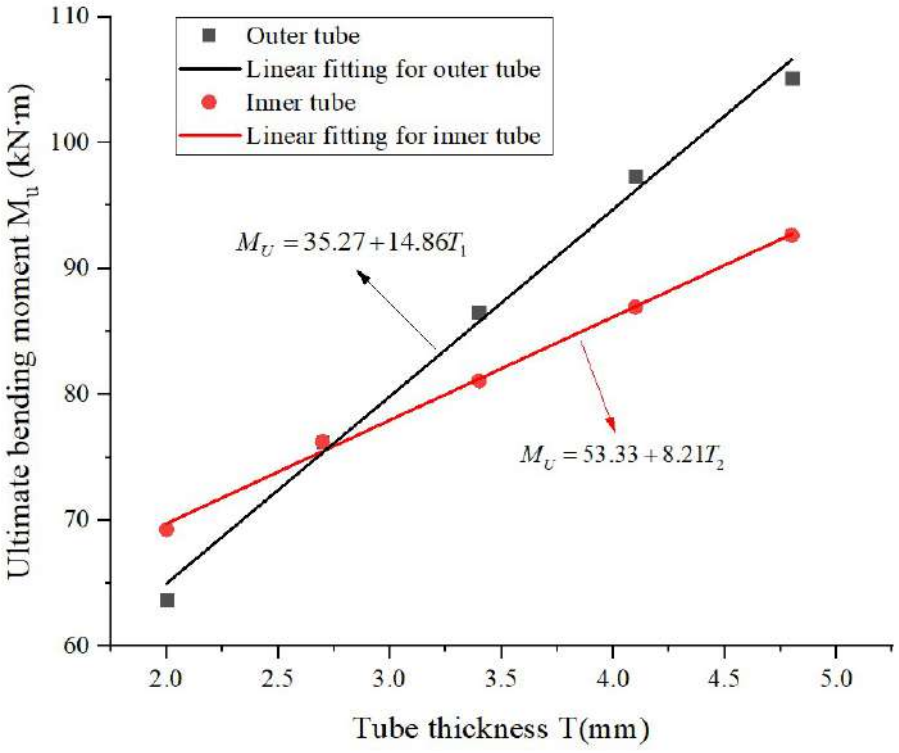

Figure 6.12: Influence of the tube thickness on the ultimate bending moment for SPB

$$M_U = 53.33 + 8.21\mathrm{T}_2 \tag{6.2}$$

Fig. 6.13 shows that with an increase of the D/T ratio, the SPB ultimate bending moments for the outer and inner pipes can be expressed by the following fitting curves, respectively:

$$M_U = 151.10exp\left[\left(-\frac{D_1}{T_1}\right)/47.58\right] + 48.44 \tag{6.3}$$

$$M_U = 90.59exp\left[\left(-\frac{D_2}{T_2}\right)/15.10\right] + 63.94 \tag{6.4}$$

6.5.4 Influence of the SHCC core thickness on the ultimate bending moment

The influence of the SHCC core thickness on the ultimate bending moment is analyzed assuming the same inner and outer pipe thickness in all simulations. The SHCC core thickness was increased from 20mm to 34mm, with increments of 2.8 mm. The material and geometric properties of the SPB specimen were assumed in the analysis. Increasing the SHCC core thickness also increases the ultimate bend-

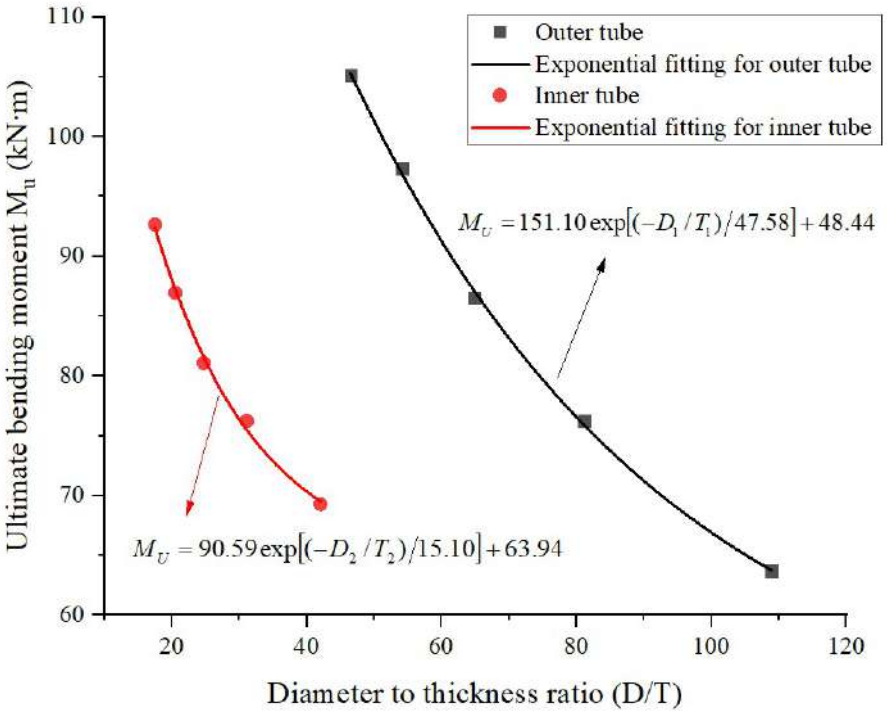

Figure 6.13: Influence of the tube thickness on the ultimate bending moment for SPB

ing moment, which is decreased when the D/t ratio is increased, as shown in Fig. 6.14.

For the SPB specimen, the fitting expressions based on the effect of the SHCC core thickness and D/T ratio are, respectively.

$$M_U = 44.56 + 1.36\mathrm{T}_3 \tag{6.5}$$

$$M_U = 259.92exp\left[\left(-\frac{D_3}{T_3}\right)/3.13\right] + 62.48 \tag{6.6}$$

6.5.5 Influence of the pipe ovality on bending moment

Fig. 6.15 shows the influence of the initial ovality (Δ_0) on the bending moment, considering the elliptical shape of the ovalized section, the lower bound ultimate bending moment is obtained for the ellipse minor axis coincident with the bending plane. Therefore, increasing the initial ovality decreases the ultimate bending moment, as shown in Fig. 6.15.

The ultimate bending moment was not significantly affected by the initial ovality, with an increase of the initial ovality, from 1.83% to 9.13%, the ultimate bending moment decreases from 74.21 kN.m to 68.23 kN.m (8.06%).

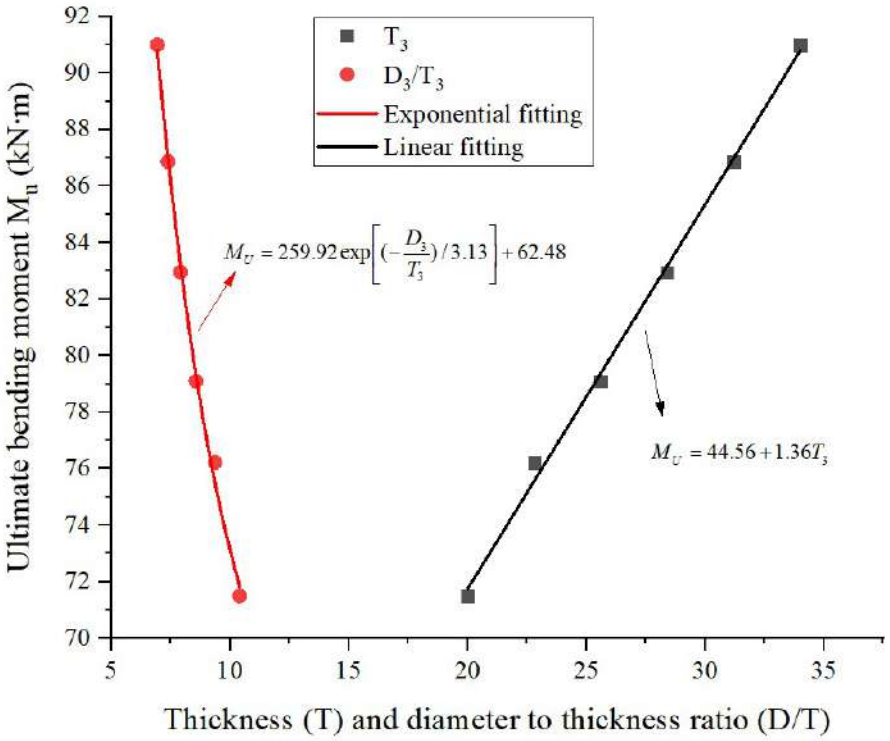

Figure 6.14: Influence of the SHCC core thickness and D/T ratio on the ultimate bending moment

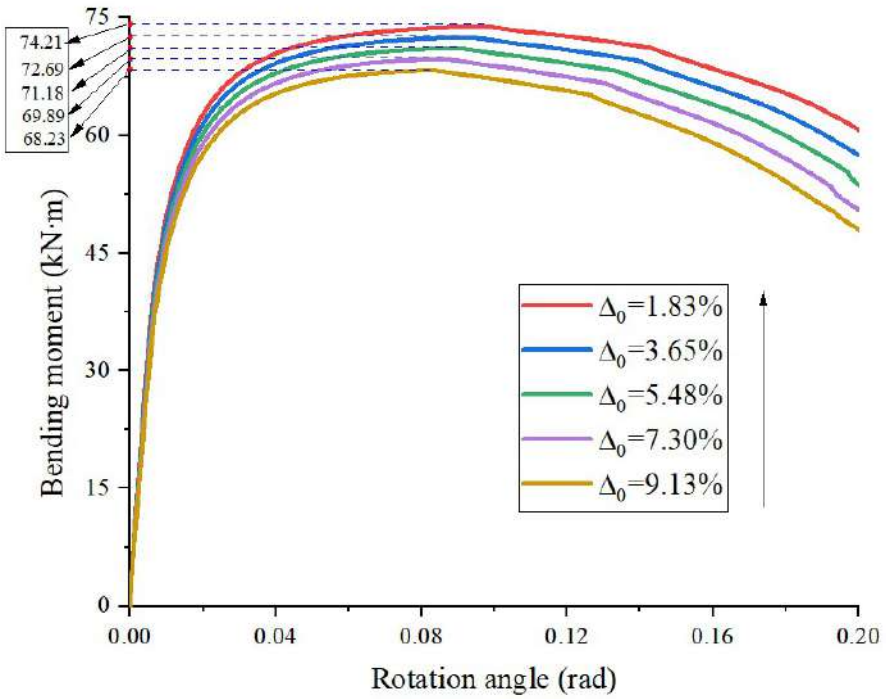

Figure 6.15: Influence of the initial ovality on the ultimate bending moment

6.6 Summary

In this chapter, the mechanical model of SPs assuming the actual interlayer model was verified by collapse and bending full-scale tests. Correlation studies between the experiments and a finite element (FE) model were performed.

Then, the SP ultimate bending moment and post-failure behavior under pure free bending were also investigated by the FE model. The bending capacities of sandwich pipes were calculated by the finite element model. The influence of geometry parameters and initial ovality on the ultimate bending moment were analyzed.

Based on the test results and numerical analysis, the following conclusions are drawn.

- To sum up, the whole mechanical model for the SPs consists of three parts as modelings for SHCC core, steel tubes, and interlayer.

- The experimental collapse pressures of SP-1A, SP-2A, SP-3A, SP-4A, SP-1B, and SP-2B are 37.68MPa, 37.18MPa, 36.92MPa, 35.23MPa, 38.71MPa, and 34.29MPa, respectively.

- The good agreement between the numerical simulation of the collapse and bending experimental data shows that the FE model for the SPs is capable of providing accurate results for the collapse and bending simulation.

- The numerical analysis for free bending SP indicated ultimate bending moments of 52.58 kN.m and 76.23 kN.m for SPA and SPB, respectively, confirming that increasing the friction coefficient and bond stress can also increase the ultimate bending moment.

- The respective numerical behavior of the two specimens demonstrated that the actual friction coefficient tends to the unbounded interlayer condition. It implies that the SP has a weak interlayer bond capacity, which can be compensated by the steel pipe surface roughness.

- The ultimate moment (M_U) of the SPs shows a linear increase with the thickness of the steel pipes or the SHCC core layer. An exponential decrease of the SP ultimate bending moment with the increase of the diameter to thickness ratio was observed from the FE model results. The increase of the initial ovality also resulted in a decrease of the SP ultimate bending moment.

Chapter 7

Conclusions and Future Works

7.1 Conclusions

The thesis proposed a comprehensive mechanical model for the sandwich pipe (SPs). The whole model should consist of different mechanical model for the strain hardening cementitious composite (SHCC) core, the steel tubes, and the actual interlayer behavior. The mechanical model for the tubes can be easily obtained by the standard uniaxial tensile and compressive tests. So, the main research work was to build the model for the SHCC core and the actual interlayer behavior.

The thesis can be divided in three parts, corresponding to the built and verification of the modified CDP model for the SHCC core, research on the actual interlayer behavior modeling, and the verification study on the whole mechanical model for SPs.

7.1.1 Modified CDP model for SHCC core

A modified concrete damage plasticity (CDP) model of an SHCC material employed as the annular layer of sandwich pipes (SPs) has been developed based on experiments and the classic continuous damage theory.

Based on the obtained results the following conclusions are presented.

- The SHCC material presents a tensile hardening region during the uniaxial tensile experiments, which can greatly improve the resistance to crack propagation in SPs under bending.

- Based on the uniaxial tensile and compressive stress-strain curves and classic continuous damage theory, the tension and compression damage variables for the theoretical model can be deduced. Using the developed CDP model, the

damage distribution in the SHCC material can be simulated in both tensile and compressive regions.

- From the theoretical analysis and biaxial compressive experiments, the value of the ratio $\frac{\sigma_{bo}}{\sigma_{co}}$ was calculated as 1.18. The value of K_c for the yield criterion for the SHCC material was adopted as 0.667.

- Based on processed triaxial compressive experimental data with the Drucker-Prager yield model, the dilation angle of the SHCC plastic flow rule was calculted as 29.4°.

7.1.2 Validation tests for the CDP model

To validate the modified CDP model for the SHCC material and its application in the finite element (FE) modeling of SPs, four-point bending tests are carried out for SHCC specimens and collapse tests are conducted for SP models, respectively.

Then, the results from numerical simulations, based on the finite element method, are correlated with experimental data.

Based on the obtained results the following conclusions are indicated below.

- Considering results from four-point bending tests and numerical simulations, it can be concluded that the CDP model can be used to reproduce the mechanical behavior and predict the damage distribution in an SHCC material.

- Considering the experiments and numerical simulations of the SP collapse, as expected, the increase of initial ovality decreases the collapse pressure, and the CDP model can be used to simulate the mechanical behavior of an SHCC material employed in the annular of SPs, as demonstrated for SPs with fully bounded and unbounded layers.

7.1.3 Experimental research on the interlayer behavior of SPs

The actual interlayer behavior of SPs was studied by the push-out test. The self-stress in the SPs was measured by experiments. The actual interlayer behavior was modeled in three parts as the surface-based cohesive model for the bond-debond behavior, the Coulomb friction model for the frictional behavior in the tangential direction, and the pressure-overclosure contact model in the normal direction.

Based on the test results and numerical analysis, the following conclusions are drawn.

- The interlayer model be used to simulate the real interlayer behavior of SPs with SHCC core, which can be used to study the mechanical behavior of SPs combined with mechanical model of SHCC core and steel tubes.

- The respective numerical behavior of the two SP specimens demonstrated that the actual friction coefficient tends to the unbounded interlayer condition. It implies that the SP has a weak interlayer bond capacity, which can be compensated by the steel pipe surface roughness.

7.1.4 Validation tests for the mechanical model of SPs

The mechanical model of SPs comprising the actual interlayer model was verified by collapse and bending full-scale tests. Correlation studies between the experiments and a finite element (FE) model were performed.

The SP ultimate bending moment and post-failure behavior under pure free bending was also investigated using the FE model. The bending capacities of sandwich pipes were calculated by the finite element model. The influence of geometry parameters and initial ovality on the ultimate bending moment was analyzed.

Based on the test results and numerical analyses, the following conclusions are drawn.

- The numerical simulation for bending of SPs confirms that increasing the friction coefficient also increases the ultimate bending moment.

- The ultimate moment (M_U) of the SPs has shown to vary linearly with the thickness of the steel pipes and that of the SHCC core layer. An exponential decrease of the SP ultimate bending moment with the increase of the diameter to thickness ratio was observed from the FE model results. The increase of the initial ovality also resulted in a decrease of the SP ultimate bending moment.

7.2 Future works

Besides the thesis work, the following aspects deserve deeper investigation.

For the interlayer relationship, in addition to the longitudinal load-slip curves were obtained by the push-out tests in the thesis, the circumferential bond behavior can be measured by the specific peeling experiment.

In addition, based on the thesis work, the further study of SPs under combined loading conditions can be performed. The following issues can be considered based on the current work of the thesis.

- Study of the behavior of the SPs under combined load of external pressure and bending, meanwhile, consider the effects of high temperatures on the interlayer properties.

- Contiune to study the behavior of the material with further tests and simulations under cyclic load.

- Design optimization of the structure of the SPs based on mechanical analysis results under multiple working conditions , i.e., construction, installation, operation, and decommission.

Bibliography

[1] Chen An, Menglan Duan, Romildo D Toledo Filho, and Segen F Estefen. Collapse of sandwich pipes with pva fiber reinforced cementitious composites core under external pressure. *Ocean Engineering*, 82:1–13, 2014.

[2] Qiang Bai and Yong Bai. *Subsea pipeline design, analysis, and installation*. Gulf Professional Publishing, 2014.

[3] Segen Farid Estefen, Theodoro Antoun Netto, and Ilson Paranhos Pasqualino. Strength analyses of sandwich pipes for ultra deepwaters. *Journal of Applied Mechanics*, 72(4):599–608, 2005.

[4] X Castello and SF Estefen. Limit strength and reeling effects of sandwich pipes with bonded layers. *International journal of mechanical sciences*, 49(5):577–588, 2007.

[5] RV Velasco. Self-consolidating concretes reinforced with high volumetrics fractions of steel fibers: Rheological, physics, mechanics and thermal properties. *PhD diss., Ph. D. Thesis. COPPE, Federal University of Rio de Janeiro, Rio de Janeiro*, 2008.

[6] Segen F Estefen, Marcelo Igor Lourenço, Junkai Feng, Claudio Moura Paz, and Dirney Bessa de Lima. Sandwich pipe for long distance pipelines: Flow assurance and costs. In *ASME 2016 35th International Conference on Ocean, Offshore and Arctic Engineering*. American Society of Mechanical Engineers Digital Collection.

[7] Kequan Yu, Yichao Wang, Jiangtao Yu, and Shilang Xu. A strain-hardening cementitious composites with the tensile capacity up to 8%. *Construction and Building Materials*, 137:410–419, 2017.

[8] Petr Jun and Viktor Mechtcherine. Behaviour of strain-hardening cement-based composites (shcc) under monotonic and cyclic tensile loading: part 1– experimental investigations. *Cement and Concrete Composites*, 32(10):801–809, 2010.

[9] Longbang Qing, Kelai Yu, Ru Mu, and John P Forth. Uniaxial tensile behavior of aligned steel fibre reinforced cementitious composites. *Materials and Structures*, 52(4):70, 2019.

[10] Cong Lu and Christopher KY Leung. A new model for the cracking process and tensile ductility of strain hardening cementitious composites (shcc). *Cement and Concrete Research*, 79:353–365, 2016.

[11] Willie Swanepoel. *The behaviour of fibre reinforced concrete (SHCC) under biaxial compression and tension*. PhD thesis, Stellenbosch: Stellenbosch University, 2011.

[12] Abd El-Hakim Khalil, Emad Etman, Ahmed Atta, and Mohamed Essam. Nonlinear behavior of rc beams strengthened with strain hardening cementitious composites subjected to monotonic and cyclic loads. *Alexandria Engineering Journal*, 55(2):1483–1496, 2016.

[13] Kaveh Arjomandi and Farid Taheri. Bending capacity of sandwich pipes. *Ocean Engineering*, 48(Jul.):17–31, 2012.

[14] Jiankun Yang, Claudio M Paz, Segen F Estefen, Guangming Fu, and Marcelo Igor Lourenço. Collapse pressure of sandwich pipes with strain-hardening cementitious composite-part 1: Experiments and parametric study. *Thin-Walled Structures*, 148:106605, 2020.

[15] Quanbiao Xu, Shunfeng Gong, and Qing Hu. Collapse analyses of sandwich pipes under external pressure considering inter-layer adhesion behaviour. *Marine Structures*, 50(nov.):72–94, 2016.

[16] MR Javanmardi and Mahmoud R Maheri. Anisotropic damage plasticity model for concrete and its use in plastic hinge relocation in rc frames with frp. In *Structures*, volume 12, pages 212–226. Elsevier, 2017.

[17] Chia Farahmandpour, Sophie Dartois, Marc Quiertant, Yves Berthaud, and Hélène Dumontet. A concrete damage–plasticity model for frp confined columns. *Materials and Structures*, 50(2):156, 2017.

[18] Yin Chi, Min Yu, Le Huang, and Lihua Xu. Finite element modeling of steel-polypropylene hybrid fiber reinforced concrete using modified concrete damaged plasticity. *Engineering Structures*, 148:23–35, 2017.

[19] Günther Meschke, Roman Lackner, and Herbert A Mang. An anisotropic elastoplastic-damage model for plain concrete. *International journal for numerical methods in engineering*, 42(4):703–727, 1998.

[20] J Lubliner, J Oliver, Sand Oller, and Eugenio Oñate. A plastic-damage model for concrete. *International Journal of solids and structures*, 25(3):299–326, 1989.

[21] Jeeho Lee and Gregory L Fenves. Plastic-damage model for cyclic loading of concrete structures. *Journal of engineering mechanics*, 124(8):892–900, 1998.

[22] Xian Xing Lambert Li. Parametric study on numerical simulation of missile punching test using concrete damaged plasticity (cdp) model. *International Journal of Impact Engineering*, 144:103652, 2020.

[23] Xiaoshan Lin and Rebecca J Gravina. An effective numerical model for reinforced concrete beams strengthened with high performance fibre reinforced cementitious composites. *Materials and Structures*, 50(5):212, 2017.

[24] Hossein Saberi A B, Tinh Quoc Bui A, Akira Furukawa A, Alireza Rahai B, and Sohichi Hirose A. Frp-confined concrete model based on damage-plasticity and phase-field approaches. *Composite Structures*, 244.

[25] Garyfalia G Triantafyllou, Theodoros C Rousakis, and Athanasios I Karabinis. Corroded rc beams patch repaired and strengthened in flexure with fiber-reinforced polymer laminates. *Composites Part B: Engineering*, 112:125–136, 2017.

[26] Jacky Mazars, François Hamon, and Stéphane Grange. A new 3d damage model for concrete under monotonic, cyclic and dynamic loadings. *Materials and Structures*, 48(11):3779–3793, 2015.

[27] Mohammad Reza Javanmardi and Mahmoud Reza Maheri. Extended finite element method and anisotropic damage plasticity for modelling crack propagation in concrete. *Finite Elements in Analysis and Design*, 165:1–20, 2019.

[28] Jia-Bao Yan and Wei Zhang. Numerical analysis on steel-concrete-steel sandwich plates by damage plasticity model: From materials to structures. *Construction and Building Materials*, 149:801–815, 2017.

[29] Bashar Alfarah, Francisco López-Almansa, and S Oller. New methodology for calculating damage variables evolution in plastic damage model for rc structures. *Engineering Structures*, 132:70–86, 2017.

[30] Najwa F Hany, Elie G Hantouche, and Mohamed H Harajli. Finite element modeling of frp-confined concrete using modified concrete damaged plasticity. *Engineering Structures*, 125:1–14, 2016.

[31] Filipe Ribeiro, José Sena-Cruz, Fernando G Branco, and Eduardo Júlio. 3d finite element model for hybrid frp-confined concrete in compression using modified cdpm. *Engineering Structures*, 190:459–479, 2019.

[32] Tine Tysmans, Maciej Wozniak, Olivier Remy, and John Vantomme. Finite element modelling of the biaxial behaviour of high-performance fibre-reinforced cement composites (hpfrcc) using concrete damaged plasticity. *Finite Elements in Analysis and Design*, 100:47–53, 2015.

[33] Aikaterini S Genikomsou and Maria Anna Polak. Finite element analysis of punching shear of concrete slabs using damaged plasticity model in abaqus. *Engineering Structures*, 98:38–48, 2015.

[34] Jobin George, J. S. Kalyana Rama, M. V. N. Siva Kumar, and A. Vasan. Behavior of plain concrete beam subjected to three point bending using concrete damaged plasticity (cdp) model. *Materials today: proceedings*, 4(9):9742–9746, 2017.

[35] Simulia. Abaqus 6.14: Abaqus/cae user guide, 2014.

[36] Dimitrios Xenos and Peter Grassl. Modelling the failure of reinforced concrete with nonlocal and crack band approaches using the damage-plasticity model cdpm2. *Finite Elements in Analysis and Design*, 117:11–20, 2016.

[37] Chen An, Xavier Castello, Menglan Duan, Romildo D Toledo Filho, and Segen F Estefen. Ultimate strength behaviour of sandwich pipes filled with steel fiber reinforced concrete. *Ocean Engineering*, 55:125–135, 2012.

[38] Huu Thanh Nguyen and Seung Eock Kim. Finite element modeling of push-out tests for large stud shear connectors. *Journal of Constructional Steel Research*, 65(10-11):1909–1920, 2009.

[39] Yin Chi, Lihua Xu, and Yuanyuan Zhang. Experimental study on hybrid fiber–reinforced concrete subjected to uniaxial compression. *Journal of Materials in Civil Engineering*, 26(2):211–218, 2012.

[40] Lazar Kachanov. Rupture time under creep conditions. *Izv. Akad. Nauk SSSR*, 8:26–31, 1958.

[41] Yu N Rabotnov. Creep problems in structural members. 1969.

[42] Jean-Louis Chaboche. Continuum damage mechanics: Part igeneral concepts. 1988.

[43] George Z. Voyiadjis and Peter I. Kattan. *Chapter 5 - Damage and elasticity in metals*. Elsevier Ltd, 2006.

[44] Amir K. Shojaei and Jianfu Shao. Application of continuum damage mechanics in hydraulic fracturing simulations. *Porous Rock Fracture Mechanics*, pages 197–212, 2017.

[45] George Z Voyiadjis and Peter I Kattan. Investigation of the damage variable basic issues in continuum damage and healing mechanics. *Mechanics Research Communications*, 68:89–94, 2015.

[46] Lu Tongqing, Wang Zhongtong, Tang Jingda, Zhang Wenlei, and Wang Tiejun. A pseudo-elasticity theory to model the strain-softening behavior of tough hydrogels. *Journal of the Mechanics and Physics of Solids*, 137.

[47] Mohammad Malikan and Victor A Eremeyev. A new hyperbolic-polynomial higher-order elasticity theory for mechanics of thick fgm beams with imperfection in the material composition. *Composite Structures*, 249:112486, 2020.

[48] P. Fuschi, A. A. Pisano, and C. Polizzotto. Size effects of small-scale beams in bending addressed with a strain-difference based nonlocal elasticity theory. *International Journal of Mechanical Sciences*, 151:661–671, 2019.

[49] George Z Voyiadjis and Peter I Kattan. A comparative study of damage variables in continuum damage mechanics. *International Journal of Damage Mechanics*, 18(4):315–340, 2009.

[50] Christopher A Walton, MF Horstemeyer, Holly J Martin, and DK Francis. Formulation of a macroscale corrosion damage internal state variable model. *International Journal of Solids and Structures*, 51(6):1235–1245, 2014.

[51] Lu, Yiyan, Liu, Zhenzhen, Li, Shan, and Na. Bond behavior of steel fibers reinforced self-stressing and self-compacting concrete filled steel tube columns. *Construction Building Materials*, 2018.

[52] L. H. Xue and S. H. Cai. Bond strength at the interface of concrete-filled steel tubular columns: Part i. *Building ence*, 12(3):22–28, 1996.

[53] Xiushu Qu and Qi Liu. Bond strength between steel and self-compacting lower expansion concrete in composite columns. *Journal of Constructional Steel Research*, 139(dec.):176–187, 2017.

[54] Zakaria Ilyes Djamai, Myriam Bahrar, Ferdinando Salvatore, Amir Si Larbi, and Mohammed El Mankibi. Textile reinforced concrete multiscale mechanical modelling: Application to trc sandwich panels. *Finite Elements in Analysis Design*, 135(nov.):22–35, 2017.

[55] Xianlin Wang, Yuqing Liu, Fei Yang, Yuanchun Lu, and Xuefeng Li. Effect of concrete cover on the bond-slip behavior between steel section and concrete in src structures. *Construction and Building Materials*, 229:116855–, 2019.

[56] Hongcheng Huang and Liang Xue. Prediction of slant ductile fracture using damage plasticity theory. *International Journal of Pressure Vessels Piping*, 86(5):319–328, 2009.

[57] Luis F Sirumbal-Zapata, Christian Malaga-Chuquitaype, and Ahmed Y Elghazouli. A three-dimensional plasticity-damage constitutive model for timber under cyclic loads. *Computers Structures*, 195(jan.):47–63, 2017.

[58] Lin Siqi, Zhang Hongtao, and Liu Chao. Constitutive relationship of bond-slip behavior of concrete-filled steel tube after exposure to high temperatures. *Special Structures*, 2015.

[59] A. Karrech, K. Regenauer-Lieb, and T. Poulet. A damaged visco-plasticity model for pressure and temperature sensitive geomaterials. *International Journal of Engineering ence*, 49(10):1141–1150, 2011.

[60] Aikaterini S. Genikomsou and Maria Anna Polak. Finite element analysis of punching shear of concrete slabs using damaged plasticity model in abaqus. *Engineering Structures*, 98:38–48, 2015.

[61] M. T. Kazemim. Hoseinzadeh Asl. Damage-plasticity model for mixed hinges in steel frames. *Journal of Constructional Steel Research*, 2011.

[62] S Khalilpour, E BaniAsad, and M Dehestani. A review on concrete fracture energy and effective parameters. *Cement and Concrete Research*, 120:294–321, 2019.

[63] Bo Chen, Chongshi Gu, Tengfei Bao, Bangbin Wu, and Huaizhi Su. Failure analysis method of concrete arch dam based on elastic strain energy criterion. *Engineering failure analysis*, 60:363–373, 2016.

[64] Yu-Gui Cao, Yu-Fei Wu, and Xiao-Qing Li. Unified model for evaluating ultimate strain of frp confined concrete based on energy method. *Construction and Building Materials*, 103:23–35, 2016.

[65] X. Castello and S. F. Estefen. Limit strength and reeling effects of sandwich pipes with bonded layers. *International Journal of Mechanical ences*, 49(5):577–588, 2007.

[66] Chengqing Wu, Jun Li, and Su Yu. *Ultra-high performance concrete-filled steel tubular columns*. 2018.

[67] Charles W. Roeder, Max T. Stephens, and Dawn E. Lehman. Concrete filled steel tubes for bridge pier and foundation construction. *International Journal of Steel Structures*, 18(1):39–49, 2018.

[68] Zhichao Lai A, Pengyu Yao A, Wenjin Huang B, Baochun Chen A, and Zheng Ying C. Reactive powder concrete-filled steel tube (rpcft) members subjected to axial tension: Experimental study and design. *Structures*, 28:933–942, 2020.

[69] Fei Yin, Wan Lin Cao, Su Duo Xue, Hong Ying Dong, and Ru Wei Wang. Behavior of multicell concrete-filled steel tube columns under eccentric loading. *Journal of Constructional Steel Research*, 172:106218, 2020.

[70] P., S., MangatM., S., and Elgarf. Bond test for reinforcing steel. *Materials Structures*, 3(3):169–174, 1970.

[71] Omid Gooranorimi, Wimal Suaris, and Antonio Nanni. A model for the bond-slip of a gfrp bar in concrete. *Engineering Structures*, 146(sep.1):34–42, 2017.

[72] Tian Yi Song, Zhong Tao, Lin Hai Han, and Brian Uy. Bond behavior of concrete-filled steel tubes at elevated temperatures. *Journal of Structural Engineering*, 143(11):04017147.1–04017147.12, 2017.

[73] Yu Chen, Ran Feng, Yongbo Shao, and Xiaotian Zhang. Bond-slip behaviour of concrete-filled stainless steel circular hollow section tubes. *Journal of Constructional Steel Research*, 130(MAR.):248–263, 2017.

[74] Thomas Gress, Jens Stahl, Tim Mittler, Lukas Spano, Hui Chen, Noomane Ben Khalifa, and Wolfram Volk. Mechanical characterization of as-cast aa7075/6060 and cusn6/cu99.5 compounds using an experimental and numerical push-out test. *Materials Ence Engineering*, 751(MAR.28):214–225, 2019.

[75] Alexandre Lavrov, Mohammad Bhuiyan, and Anna Stroisz. Push-out test: Why bother? *Journal of Petroleum Science and Engineering*, 172, 2018.

[76] A.L.A.C.H.E.K. Ibrahim, R.E.B.O.U.L. Nadége, and J.U.R.K.I.E.W.I.E.Z. Bruno. Experimental and finite element analysis of push-out shear test for adhesive joints between pultruded gfrp and concrete. *International Journal of Adhesion and Adhesives*, 98:102552–, 2020.

[77] A. Kozmaa, C. Odenbreita, M. V. Brauna, M. Veljkovicb, and M. P. Nijghb. Push-out tests on demountable shear connectors of steel-concrete composite structures. In *International Conference on Advances in Steel-concrete Composite Structures-asccs*, pages 45–54, 2019.

[78] Di Jin, Zou Yang, Zhou Xuhong, Qin Fengjiang, and Peng Xi. Push-out test of large perfobond connectors in steelconcrete joints of hybrid bridges. *Journal of Constructional Steel Research*, 150:415–429, 2018.

[79] S O Bamaga, M M Tahir, C S Tan, P N Shek, and R. Aghlara. Push-out tests on three innovative shear connectors for composite cold-formed steel concrete beams. *Construction and Building Materials*, 223(2019):288–298, 2019.

[80] Ran Feng, Yu Chen, Kang He, Jiangang Wei, Baochun Chen, and Xiaotian Zhang. Push-out tests of concrete-filled stainless steel shs tubes. *Journal of Constructional Steel Research*, 145(JUN.):58–69, 2018.

[81] Qinghua Han, Yihong Wang, Jie Xu, Ying Xing, and Guang Yang. Numerical analysis on shear stud in push-out test with crumb rubber concrete. *Journal of Constructional Steel Research*, 130(MAR.):148–158, 2017.

[82] Michael A. Minnicino and Michael H. Santare. Modeling the progressive damage of the microdroplet test using contact surfaces with cohesive behavior. *Composites ence Technology*, 72(16):2024–2031, 2012.

[83] Seungwook Seok, Ghadir Haikal, Julio A. Ramirez, Laura N. Lowes, and Jeehee Lim. Finite element simulation of bond-zone behavior of pullout test of reinforcement embedded in concrete using concrete damage-plasticity model 2 (cdpm2). *Engineering Structures*, 221:110984, 2020.

[84] Loidolt Peter, Manfred H. Ulz, and Khinast Johannes. Modeling yield properties of compacted powder using a multi-particle finite element model with cohesive contacts. *Powder Technology*, 336:426–440, 2018.

[85] Shunhua Chen, Naoto Mitsume, Wei Gao, Tomonori Yamada, Mengyan Zhang, and Shinobu Yoshimura. A nodal-based extrinsic cohesive/contact model for interfacial debonding analyses in composite structures. *Computers Structures*, 215(APR.):80–97, 2019.

[86] P. F. Liu, X. Q. Peng, and Z. Y. Guo. A viscoelastic cohesive/friction coupled model for delamination analysis of composite laminates. *Theoretical and Applied Fracture Mechanics*, 103:102263, 2019.

[87] Kim Wallin. A simple fracture mechanics based charpy-v impact energy criterion for plastic collapse. *Engineering Fracture Mechanics*, 237:107247, 2020.

[88] Hao Cheng and Xiaoping Zhou. An energy-based criterion of crack branching and its application on the multidimensional space method. *International Journal of Solids and Structures*, 182-183, 2019.

[89] M. L. Benzeggagh and M. Kenane. Measurement of mixed-mode delamination fracture toughness of unidirectional glass/epoxy composites with mixed-mode bending apparatus. *Composites ence and Technology*, 56(4):439–449, 1996.

[90] C ASTM et al. Standard specification for coal fly ash and raw or calcined natural pozzolan for use in concrete. *ASTM Int*, 4, 2012.

[91] J Zhang and J Li. Investigation into lubliner yield criterion of concrete for 3d simulation. *Engineering Structures*, 44:122–127, 2012.

[92] Niels Saabye Ottosen. A failure criterion for concrete. *American Society of Civil Engineers. Engineering Mechanics Division. Journal*, 103(4):527–535, 1977.

[93] Gerald Schickert and Helmut Winkler. Results of test concerning strength and strain of concrete subjected to multi-axial compressive stress. 1977.

[94] Frank Erwin Richart, Anton Brandtzaeg, and Rex Lenoi Brown. A study of the failure of concrete under combined compressive stresses. Technical report, University of Illinois at Urbana Champaign, College of Engineering, 1928.

[95] Laddie L Mills and Roger M Zimmerman. Compressive strength of plain concrete under multiaxial loading conditions. In *Journal Proceedings*, volume 67, pages 802–807, 1970.

[96] Saeed Karim Babanajad, Yaghoob Farnam, and Mohammad Shekarchi. Failure criteria and triaxial behaviour of hpfrc containing high reactivity metakaolin and silica fume. *Construction and Building Materials*, 29:215–229, 2012.

[97] Ertekin Öztekin, Selim Pul, and Metin Hüsem. Experimental determination of drucker-prager yield criterion parameters for normal and high strength concretes under triaxial compression. *Construction and Building Materials*, 112:725–732, 2016.